REPUBLIQUE ALGERIENNE DEMOCRATIQUE ET POPULAIRE
MINISTERE DE L'ENSEIGNEMENT SUPERIEUR ET DE LA RECHERCHE SCIENTIFIQUE

Université Frère Mentouri - Constantine 1
Faculté des Sciences de la Technologie
Département d'Electronique
Laboratoire Signaux et Systèmes de Communication, SISCOM

No. série: ...

Thème

Détection Automatique CFAR de Cibles dans les SAR Imageurs

Par

Hicham Madjidi

Présentée en Vue de l'Obtention du Diplôme de
Doctorat Troisième Cycle en Télécommunications
Option Signaux et Systèmes de Télécommunications

Soutenue devant le Jury

Président:	Pr Benslama Malek	Université Frères Mentouri Constantine 1
Rapporteur:	Pr Laroussi Toufik	Université Frères Mentouri Constantine 1
Examinateurs:	Pr Soltani Faouzi	Université Frères Mentouri Constantine 1
	Pr Hamadouche M'hamed	Université M'hamed Bougara Boumerdès
	Pr Fortaki Tarek	Université Mostefa Ben Boulaïd Batna 2

Année Universitaire 2022-2023

"O Allah, benefit me with that which You have taught me, and teach me that which will benefit me, and increase me in knowledge. All praise is due to Allah in every condition, and I seek refuge in Allah from the condition of the people of the Fire"

Prophet Muhammad (PBUH)

Dedications

I would like to dedicate this thesis to my parents, Mohammed and Sakta Reguia, who have always believed in me, gave me all great and precious things, instilled in me the love of science from a young age, always encouraged me to follow my dreams and supported me every step of the way. They have the credit after Allah (SWT) for what I have achieved. Their steadfast affection and wisdom have served as the bedrock of my life.

I would also like to dedicate this thesis to my siblings, Fathi, Saad, Fouzia, Soumia and Houria. Thank you for being my best friends and for always cheering me on. I consider myself really fortunate to have you in my life. Finally, to all the family, friends and to all those who are dear to me and provided encouragement and motivation during the ups and downs of this research journey.

Acknowledgements

In the name of Allah, the Most Gracious and the Most Merciful.

First and foremost, I want to thank Allah for providing me with the chance, ability, strength, and determination to accomplish this assignment. Without Your divine intervention, my thesis would not have come to fruition.

I would also like to convey my most sincere thanks to my supervisor, Prof. Toufik Laroussi, for his great support and guidance during the completion of this thesis. Besides, I am truly grateful for the freedom he gave me during my research, which enormously helped my growth as an independent researcher and to perform without excessive pressure. Being under his direction has been a real joy and honor for me.

Finally, I would also like to thank the Jury, namely, the president, Prof. Benslama Malek, from the University Frères Mentouri Constantine 1 and the members, Prof. Soltani Faouzi, from the University Frères Mentouri Constantine 1, Prof. Hamadouche M'hamed from the University M'hamed Bougara Boumerdès and Prof. Fortaki Tarek from the University Mostefa Ben Boulaïd Batna 2, who consented to be the thesis examiners and whose suggestions and recommendations will undoubtedly help me enhance the quality of my thesis.

The work presented in this PhD thesis was carried out at the SISCOM Laboratory (Laboratoire Signaux et Systèmes de Communication), Department of Electronics, University Frères Mentouri Constantine 1.

ملخص

في أطروحة الدكتوراه هذه ، نعالج مشكلة الكشف التلقائي للسفن على صور SAR (Synthetic Aperture Radar) في بيئة معقدة. بافتراض فوضى بحرية غير غوسية بدون معرفة مسبقة حول وجود أو عدم وجود أي حافة فوضى و\أو أهداف متداخلة في النافذة المرجعية المنزلقة، نقترح ونحلل أداء الكشف لثلاثة كاشفات CFAR (Constant False Alarm Rate) في فوضى البحر العادية وغير المتجانسة Lognormal أو Weibull. من خلال القيام بذلك ، نقوم أولاً بتحليل كاشف QM-CFAR (Quantile Matching-Constant False Alarm Rate) في خلفية Weibull. يعالج هذا الكاشف مشكلة كاشف الرقابة في المواقف المستهدفة المتعددة. على وجه التحديد ، بافتراض فوضى Weibull غير ثابتة مع وجود أو عدم وجود أهداف متداخلة، يتم استخدام QM و MLE (Maximum Likelihood Estimator) بشكل متزامن للسماح للكاشف المقترح بالأداء بقوة في المواقف المستهدفة المتعددة مع معلمات Weibull غير المعروفة مسبقاً. تظهر محاكاة MC (Monte-Carlo) أنه مقارنة بخوارزميات CFAR الحالية، يوفر كاشف QM-CFAR تقديرات قوية ودقيقة لمعلمات توزيع Weibull ويحقق تدهوراً أقل لـ P_D (Probability of Detection) في المواقف المستهدفة المتعددة. بعد ذلك ، من أجل تقليل تأثير القيم المتطرفة على الكاشف القائم على SD (Standard Deviation) ، نقترح استخدام MAD (Median Absolute Deviation)، لأنه بديل قوي وسريع لـ SD. يمكن حساب عتبة الكشف عن كاشف MAD-CFAR المقدمة حديثاً بشكل مباشر ؛ تحقيق مكاسب كبيرة في P_D ووقت المعالجة. أخيراً ، نعالج مشكلة الرقابة التلقائية المنخفضة والعليا للعينات غير المرغوب فيها من بيانات مرتبة للخلايا المرجعية ، أي الرقابة الثنائية أو المزدوجة التلقائية. تحقيقا لهذه الغاية ، نقترح استخدام CFCR (Constant False Censoring Rate) وعتبات CFAR للكشف عن ثنائية الطور للرقابة على القيم الخارجية الدنيا والعليا. من خلال القيام بذلك ، نقترح مقدراً جديداً AML (Approximate Maximum Likelihood) ، والذي يولد تعبيرات مغلقة لمعلمات التوزيع المعرفية دون الحاجة إلى تكرارات. أظهرنا أنه في خلفية غير متجانسة غير طبيعية ، يكتسب كاشف السفن AML-CFAR نظام P_{FA} (Probability of False Alarm)، أداء كشف عالي وتكلفة زمنية عادلة فيما يتعلق بأحدث أجهزة الكشف.

Abstract

In this PhD Thesis, we address the problem of automatic ship detection acquires from SAR (Synthetic Aperture Radar) images in complex marine environments. Assuming a non-Gaussian sea clutter with no prior knowledge about the presence or not of any clutter edge and/or interfering targets in the sliding reference window, we propose and analyze the detection performances of three CFAR (Constant False Alarm Rate) detectors in homogeneous and heterogeneous Log-normal or Weibull sea clutter. In doing this, we first analyze the QM-CFAR (Quantile Matching-Constant False Alarm Rate) detector in a Weibull background. This detector addresses the problem of fixed-point(s) censoring detector in multiple target situations. Specifically, assuming a non-stationary Weibull clutter with the presence or not of interfering targets, the QM and the MLE (Maximum Likelihood Estimator) are concomitantly used to allow the proposed detector to perform robustly in multiple target situations with a priori unknown Weibull parameters. MC (Monte-Carlo) simulations show that, compared to recent existing CFAR algorithms, the QM-CFAR detector provides robust and accurate estimates of the Weibull distribution parameters and achieves less degradation of the P_D (Probability of Detection) in multiple target situations. Then, for the sake of reducing the effect of outliers on the SD (Standard Deviation) based detector, we suggest the use of the MAD (Median Absolute Deviation), as it is a robust and fast alternative to SD. The newly presented MAD-CFAR detector's detection threshold can be computed straightforwardly; yielding a significant gain in the P_D and processing time. Finally, we address the problem of lower and upper automatic censoring of unwanted samples from a rank ordered data of reference cells, i.e., bilateral or dual automatic censoring. To this end, we suggest the use of CFCR (Constant False Censoring Rate) and CFAR detection biparametric thresholds to censor lower and upper outliers. In doing this, we propose a novel estimator AML (Approximate Maximum Likelihood), which generates closed-form expressions of lognormal distribution parameters with no iterations needed. We showed that in a log-normal heterogeneous background, the AML-CFAR ship detector acquires a fair P_{FA} (Probability of False Alarm) regulation, a high detection performance and a fair time cost with regard to the challenging state-of-the-art detectors.

Résumé

Dans cette thèse de doctorat, nous considérons le problème de la détection automatique de navires à partir d'images acquise par un SAR (Synthetic Aperture Radar) opérant dans des environnements marins complexes. En supposant un clutter non gaussien sans aucune connaissance préalable de la présence ou non d'un bord de clutter et/ou de cibles interférentes dans la fenêtre de référence glissante, nous proposons et analysons les performances de détection de trois détecteurs CFAR (Constant False Alarm Rate) pour un clutter marin homogène et hétérogène de type Log-normal ou Weibull. Pour ce faire, nous analysons tout d'abord le détecteur QM-CFAR (Quantile Matching-CFAR) dans un clutter Weibull. Ce détecteur traite le problème de la censure de point fixe dans des situations de cibles multiples. Plus précisément, en supposant un clutter Weibull non stationnaire avec la présence ou non de cibles interférentes, le QM et le MLE (Maximum Likelihood Estimator) sont utilisés concomitamment pour permettre au détecteur proposé de fonctionner de manière robuste dans des situations de cibles multiples avec un clutter Weibull dont les paramètres sont inconnus *a priori*. Les simulations MC (Monte-Carlo) montrent que, par rapport aux récents algorithmes CFAR, le détecteur QM-CFAR induit une estimation des paramètres du clutter Weibull de manière précise et impacte une dégradation moindre de la P_D (Probability of Detection). Ensuite, afin de mitiger l'effet des interférences sur le détecteur basé sur l'écart-type, nous suggérons l'utilisation du détéecteur MAD (Median Absolute Deviation), qui consiste en une alternative plus robuste et plus rapide que celle basée sur l'écart-type. Le seuil de détection du détecteur MAD-CFAR nouvellement présenté peut être calculé directement, ce qui se traduit par un gain significatif en termes de P_D et de temps de traitement. Enfin, nous considérons le problème de la censure automatique bilatérale d'échantillons non désirés à partir d'une suite ordonnée des cellules de référence. A cet effet, nous suggérons l'utilisation de seuils biparamétriques de détection CFCR (Constant False Censoring Rate) et CFAR pour censurer les cellules indésirables de plus petites et de plus grandes puissances. Pour ce faire, nous proposons un nouvel estimateur AML (Approximate Maximum Likelihood) qui infère des expressions littérales des paramètres de la distribution lognormale. Nous montrons que pour un clutter hétérogène log-normal, le détecteur de navires AML-CFAR acquiert une régulation de la P_{FA} (Probability of False Alarm) rationnelle, une performance de détection élevée et un coût raisonnable par rapport aux détecteurs existants.

Contents

List of Figures

List of Tables

List of Abbreviations

AD	Anderson–Darling
AML	Approximate Maximum Likelihood
ANN	artificial neural networks
ATR	Automatic Target Recognition
BQME	Bayesian QME
BTSR	Robust Bilateral-Trimmed-Statistics
CA	Cell Averaging
CCDF	Complementary CDF
CDF	Cumulative Distribution Function
CFAR	Constant False Alarm Rate
CFCR	Constant False Censoring Rate
CML	Censored ML
CPU	Central Processing Unit
CUT	Cell Under Test
DR	Detection Rate
EDF	Empirical Distribution Function
EO	Earth Observation
EU	European Union
FAR	False Alarm Rate
GB	Giga Bytes
GHz	Giga Hertz
GMOS	Geometric Mean Order Statistics
GO	Greatest of
GRMM	Generalized Rayleigh Mixture Model
GT	Ground Truth
GoF	Goodness of Fit
HLC	High Level Classifier
ICDF	Inverse CDF
IE	Inclusion/Exclusion
IEEE	Institute of Electrical and Electronics Engineers
IID	Independent and Identically Distributed
ITU	International Telecommunications Union
KDE	Kernel Density Estimation
KS	Kolmogorov-Smirnov

LED	Linear Envelope Detector
LLC	Low Level Classifier
LMM	Log-normal Mixture Model
LNTS	Log-Normal Truncated Statistics
LS	Location Scale
LUB	Least Upper Bound
MAD	Median Absolute Deviation
MC	Monte-Carlo
MLE	Maximum Likelihood Estimator
MSE	Mean Squared Error
N-P	Neyman-Pearson
NRT	Near Real Time
OCR	Outlier Contamination Ratio
OEM	Ocean Environment Monitoring
OS	Ordered Statistic
PD	Probability of Detection
PDF	Probability Density Function
PFA	Probability of False Alarm
PFC	Probabilities of False Censoring
PM	Probability of Miss
PNull	Probability of Null detection
PRF	Pulse Repetition Frequency
PRI	Pulse Repetition Interval
PUT	Pixel Under Test
QM	Quantile Matching
QME	QM Estimation
RADAR	RAdio Detection And Ranging
RAM	Random Access Memory
RAR	Real Aperture Radar
RCS	Radar Cross Section
RF	Radio Frequency
ROC	Receiver Operating Characteristics
ROIs	Regions Of Interest
RRMSE	Relative Root Mean Square Error
RS	Remote Sensing
RT	Real Time
RV	Random Variable

SAR	Synthetic Aperture Radar
SCR	Signal to Clutter Ratio
SD	Standard Deviation
SDM	Standard Deviation around the Mean
SIR	Signal to interference Ratio
SLAR	Side-Looking Airborne Radar
SO	Smallest of
SRW	Sliding Reference Window
SVM	Support Vector Machine
TMOS	Trimmed Mean Order Statistics
TS	Truncated Statistics
UN	United Nations
USA	United States of America
WH	Weber Haykin
WL	Weighted Likelihood
WLMM	Weibull Lognormal Mixture Model
WWII	World War II

Chapter 1

General Introduction

Summary

In this chapter, we recall some useful definitions of SAR (Synthetic Aperture Radar) imagery and the fundamental principles of ATR (Automatic Target Recognition) systems. Then, we position ourselves in relation to the problems we want to solve. Finally, we present the reading structure of this thesis.

1.1 Introduction

With increasing worldwide world travel and transport of goods, vessel traffic services. OEM (Ocean Environment Monitoring) has become one of the most important tasks of the coastal authorities nowadays, which involves tracking and monitoring illegal vessel activities, oil spills, retrieval of wave parameters, wind and current observations, etc. According to the UN (United Nations) [3], maritime-based trade has grown at a rapid pace in recent years (4% in 2017), with a compound annual growth rate of 3.8% projected between 2018 and 2023. Seaborne transportation accounts for almost 90% of freight trade outside the EU (European Union) and 40% of freight trade within the EU. Furthermore, over 400 million passengers utilize European ports annually. Regarding fuel exchange, tankers are currently transporting significant amounts of natural gas and 90% of oil is already transported by sea. In terms of fisheries, the number of vessels in the European fishing fleet in 2017 was almost 83,000, even though it has been getting smaller over the past ten years. In this setting, measures to ensure the safety of navigation and, more broadly, the marine environment is critical indeed, all of these circumstances have contributed to maritime surveillance becoming an increasingly heated subject.

In this context, RS (Remote Sensing) can provide valuable support. It is one of the geospatial technologies that are having an increasing influence in fields ranging from business to research, to public policy. Often known as EO (Earth Observation) [4], it is the process of gathering information about objects or areas on the Earth's surface using electromagnetic radiation without coming into physical touch with the object or area. This technological progress includes mainly the appearance and development of new observation and acquisition systems. Among them, we distinguish the RADAR (RAdio Detection And Ranging) which is an active system that can be used day and night under various weather conditions. These two advantages have led to an expansion of research work providing this system with new and increasingly sophisticated functionalities and capabilities. Among the RS systems, due to its unique ability to provide high-resolution images of the earth's surface, even in challenging conditions such as low light or cloud cover, the SAR (Synthetic Aperture Radar) imagery has become an increasingly important tool for a wide range of applications. SAR imagery is used for a variety of purposes, including [5]

Environmental monitoring: SAR imagery is a powerful tool for monitoring the environment and tracking changes over time. It is used to monitor and track deforestation, glacier melting, soil erosion, and other changes to the earth's surface. SAR imagery provides detailed information about the earth's surface, allowing researchers and policymakers to make informed decisions about how best to preserve and protect the environment [6].

Disaster response: SAR imagery can play a critical role in disaster response efforts by providing accurate and timely information about the extent of damage and the areas that require the most assistance. It is used to assess damage, plan relief efforts, and monitor recovery progress following natural disasters such as hurricanes, earthquakes and floods. SAR imagery provides valuable information about the affected areas, even in situations where access is difficult or impossible for human responders [7].

Maritime surveillance: SAR imagery is an essential tool for maritime surveillance and tracking of shipping lanes. It is used to detect and track ships, monitor vessel traffic, and aid in search and rescue operations. The high resolution and ability to penetrate cloud cover make SAR imagery an ideal tool for maritime surveillance especially monitoring areas with frequent cloud cover, allowing authorities to monitor and respond to potential threats in real-time [3, 8].

Defense and security: SAR imagery has become an important tool for defense and security purposes, such as surveillance, target acquisition, and reconnaissance. It provides high-resolution images of the earth's surface, even in challenging conditions, making it an ideal tool for military and security applications [9].

The intrinsic capability of this instrument is to provide a quick view of the oceanic surface features such as vessels, waves and currents, oil spills, laver facilities and wind fields (Cf. Figure 1.1). SAR has been developed into a mature and powerful microwave RS technology since it was proposed by Carl Atwood Wiley, a mathematician and engineer of Goodyear Aerospace Corporation in the United States in 1951 [10]. The latter remains a suitable option for a depiction of the observed target since it gives rich visual information about the observed radar target. In addition, modern SAR sensors can offer wide-area imaging capabilities, and generate large amounts of data in a short period of time, and there is an obvious need for automatic detection of targets of interest.

The use of SAR imagery for ship detection has been an active area of research in recent years. A number of automatic ship detection algorithms have been proposed. These algorithms are designed to provide an efficient and effective means of detecting and locating

Figure 1.1: Schematic representation of activities and impacts in a coastal zone [1].

ships in SAR images, eliminating the need for manual detection with the ability to detect objects or events as they are happening, without any significant delay. This is one of the key challenges addressed in this thesis.

Ship detection in SAR imagery can be accomplished through two different methods: the detection of the ship target itself, and the detection of the ship's wake [11]. The detection of the ship's wake involves identifying and locating the distinct patterns created by the ship as it moves through the water. This is typically accomplished by analyzing the SAR image for changes in the sea surface, such as waves and wakes, which can be indicative of the presence of a ship. The detection of the ship target, on the other hand, involves identifying and locating the ship in the SAR image. This is typically accomplished by using image processing techniques, such as segmentation and feature extraction, to isolate the ship target from the rest of the image. The unique radar signature of ships, including their shape, size, and RCS (Radar Cross Section), can be used to distinguish them from other objects in the image, such as land masses, sea clutter, and clouds. Here we will only focus on algorithms that detect the ship itself. Within the framework of the work carried out and presented in this thesis, one of the objectives is the development of innovative and robust processing methods allowing the improvement of the automatic target detection process in SAR images. The requirements that any identification system has to provide are a high P_D (Probability of Detection), constant P_{FA} (Probability of False Alarm), accurate geo-location, ship identification, and ability in operating in all weather and light conditions. The well-known CFAR (Constant False Alarm Rate) concept is a signal processing strategy to control the false alarm rate in automatic radar target detection. CFAR detectors are widely used in ATR systems to accurately detect targets in noisy and cluttered environments [12]. CFAR detectors are designed to provide a constant P_{FA}, regardless of the changing environmental conditions. This is achieved by adjusting the threshold of the detector dynamically, based on the statistical properties of the background clutter. The use of CFAR detectors in SAR-ATR systems has been widely researched and implemented in recent years. Many researchers and industry professionals have recognized the importance of CFAR detectors and have dedicated their efforts to improving the algorithms and methods of their implementation [13, 14].

For all these reasons, it is of paramount importance to review and discuss the potentialities of SAR in the wide range of maritime surveillance applications, which is the main reason that led to the publication of this thesis.

1.2 SAR-ATR of Ships

Target detection is the front-end stage in any ATR system for SAR imagery [15]. Previous research on automatic target detection in SAR imaging has clearly demonstrated that no single detection method produces good results and that a hierarchical system of algorithms is required. The efficacy of the detector directly impacts the succeeding stages in the SAR-ATR processing chain. Figure 1.2 depicts the overall framework of an end-to-end ATR system for SAR imaging as documented in the literature [5, 15]. Accordingly, ship detection systems generally consist of several distinctive stages, land masking, detector, also known as prescreener, LLC (Low Level Classifier) also known as discriminator), and HLC (High Level Classifier). The LLC and HLC stages together are commonly known as the focus-of-attention module. While this is the most common structure reported in the literature, it should be highlighted that (theoretically) there is no restriction on the number of stages [15].

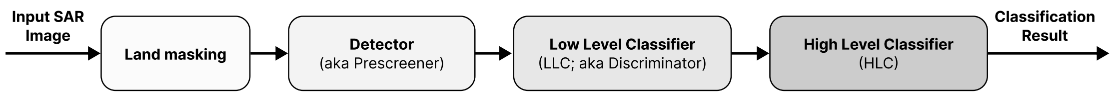

Figure 1.2: General structure for an end-to-end SAR-ATR system.

1.2.1 Land masking

Land masking is a pre-required stage for most traditional ship detection systems. It is one of the most important stages since ship detectors can produce high numbers of false alarms when applied to land areas; this is owing to the fact that land has higher reflectance values than open sea [5]. Managing these false alarms can strain detection systems too much. Accurate land masking is generally complex due to the inaccuracy of recorded coastline, tidal variations, and coastal constructions. Registering the SAR image with existing geographic maps is a common method for land masking. Even though this is the simplest method, it is not perfect. Registration errors are common in satellite imagery because the orbital parameters are not precisely known. Naturally, there is also the possibility of tidal variations and the geographical maps may not show small islands and rocks. As a result, portions of land will be designated as ocean, and vice versa. Such issues may happen with registration errors. Despite the fact that manual registration can reduce errors, it is neither intelligent nor cost-effective. The use of specific algorithms to automatically identify the coastline is another approach to territory masking. The vast majority of shoreline extraction algorithms are based on these image handling steps, which employ an edge operator to remove speckle noise. After that, a mean filter is used to expand the edge map, and thresholding is used to tell the difference between land and water. Even though the current coastline extraction algorithms outperform registration, they are unable to detect in real time and complex sea conditions, resulting in a significant decline in performance. The following literature chapters will not examine land masking because it is not the primary goal of this research; but we do mention the following new algorithm for removing high-intensity land areas from the SAR image. That is, the group of pixels which is brighter than other pixels in the subimage is defined as [11]

$$\nu = \frac{\left[\mu_{\text{local window}}\right]^2}{2\left[\sigma_{\text{tile}}\right]^2} \tag{1.1}$$

where $\mu_{\text{local window}}$ is the average of pixels in the moving window and σ_{tile} the standard deviation of all pixels in the processed subimage. This operation removes land areas and many pixels with high brightness, but maintains the ships with only a few pixels.

1.2.2 Prescreening

Prescreening, also known as detection, is the front-end stage in any SAR-ATR processing stages [15]. The objective of the preprocessing stage is to reduce the amount of data that need to be processed in the later stage and improve the accuracy of the next detection stage by identifying all ROIs (Regions Of Interest). The ROIs can then be passed into the LLC stage for further analysis [Crisp, 2004]. Defining a global threshold of the image is a simple way to proclaim any pixel value beyond the threshold as an anticipative ship pixel, but can cause numerous false alarms. However, the detector should be constructed to strike a compromise between computing complexity, detection effectiveness, and outlier rejection. Also in order to function in real-time or close to real-time, the detector needs to be computationally simple. In contrast, the detector must have a high P_D and a low P_{FA}.

Without a robust clutter rejection algorithm, such a system will almost certainly have unacceptable numbers of false alarms and misidentifications [16]. There are numerous strategies for implementing the detector. Adaptive thresholding is a type of algorithm that is commonly used in the prescreening stage of an ATR system for SAR imagery. The main idea behind this type of thresholding is the use of a different threshold for each pixel in the image, rather than using a single global threshold for the entire image. The threshold for each pixel is determined based on the intensity values in the local neighborhood of that pixel. This allows the threshold to be adjusted dynamically based on the local image characteristics, making it possible to effectively filter out background clutter and noise while preserving the target information. There are several different types of adaptive thresholding algorithms, each with its own strengths and weaknesses. The most popular adaptive thresholding algorithms include the well-known CFAR method, derived from the Bayesian decision theory. It is a signal processing strategy to control the false alarm rate in automatic radar target detection. It has been extensively studied and applied in several SAR-ATR systems [17, 15]. While detecting targets in nonstationary clutter, CFAR detectors must maintain a constant P_{FA}. Typically, the distribution of the set of observation samples is unknown and varies from set to set. In practice, it is commonly believed that distribution functions are known only partially within some parameters that may be inferred from the observation. This simplifying assumption leads to detection techniques for a wide range of probability distributions.

The crucial idea of a good CFAR detector is based on multiple stages. As shown in Figure 1.3, the separation of the clutter from the target is usually accomplished by a rectangle-shaped sliding window. This latter is divided into a PUT (Pixel Under Test), a guard region, which must be at least twice as large as the target of interest, and a clutter region, whose size should be large enough to estimate the local clutter statistics accurately [18]. The use of a guard region is an important aspect in CFAR detection, as it helps to ensure that the target

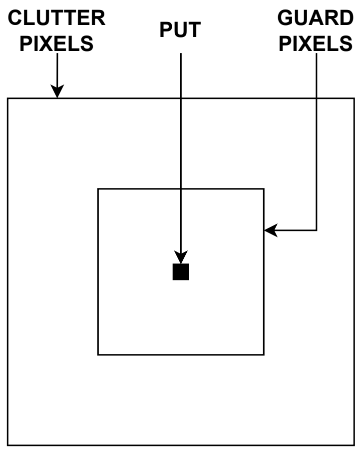

Figure 1.3: CFAR sliding window depicting the PUT, guard region and clutter region.

detection threshold is set accurately and optimally and to ensure that no pixels of an extended target could be included in the clutter region, resulting in a skewed PDF (Probability Density Function) and an erroneous detection threshold calculation [19]. However, the use of the guard region is not always the most accurate or appropriate method for all scenarios. Alternatives to the conventional guard region approach are discussed in the forthcoming chapters.

1.2.3 Low Level Classification

After the prescreener has identified ROIs that potentially contain targets, the LLC stage eliminates areas within the ROI that are composed of clutter, even if they were initially detected by the detector. The LLC stage may be thought of as a process of gradually reducing false alarms from a broad to a more precise level [5]. At the end of this procedure, only ship targets should be marked, and any false alarms should be deleted. Discrimination can be achieved through a variety of techniques, including [20].

Feature Extraction: This method involves identifying and extracting distinctive features of the target, such as its shape, size diameter or the length of the smallest box that encloses all the bright scatters in a binary image, orientation and texture. These features are used to differentiate between targets and clutter.

Statistical Classification: This method involves statistical techniques, such as decision trees, support vector machines or neural networks, to classify the image pixels into target and clutter categories. The statistical classifier is trained using a labeled dataset that consists of examples of both targets and clutter, and the classifier uses this training data to make predictions about the target/clutter categories of new pixels.

Model-Based Discrimination: This method involves a physical or mathematical model of the target to discriminate between targets and clutter. The model-based approach can be used in conjunction with other discrimination methods, such as feature extraction or statistical classification, to improve the overall performance of the ATR system.

Contextual Discrimination: This method involves the information about the spatial context of the image pixels, such as their location, neighbors, and surrounding environment, to differentiate between targets and clutter. Contextual information can be used to provide additional constraints on the target/clutter categorization, and can be particularly useful in cluttered environments where other discrimination methods may fail.

Each of these techniques has its own strengths and limitations. ATR systems often use a combination of these approaches to achieve the highest level of accuracy and reliability. This research work does not delve into land masking or discrimination as these are not the primary focus of the study and will not be addressed in the subsequent chapters.

1.2.4 High Level Classifier

An HLC is a type of machine learning model or algorithm that performs complex classification tasks, often involving multiple classes and complex relationships between the classes. The goal of an HLC is to accurately predict the class or category of an object or instance based on a set of features or attributes [15].

Unlike LLCs, which perform simple binary classification tasks, HLCs can handle multiple classes, complex relationships between the classes, and can make predictions based on more nuanced and sophisticated analysis of the data. HLCs are often more accurate and flexible than LLCs, but they may also be more computationally intensive and require more data to train effectively.

Examples of HLCs include decision trees, random forests, support vector machines, neural networks and deep learning models. These models can be used in a wide range of applications, including image recognition, speech recognition, natural language processing and predictive analytics.

1.3 Contributions

The primary aim of this thesis focuses on providing novel automatic tools for ship target detection using advanced SAR imagery technology. This thesis contains a number of research articles that give thorough statistical analysis of sea clutter and handle difficult detection challenges caused by multiple target situations and non-homogeneous ocean environments.

In order to achieve the objective of this research work, the CFAR target detection concept is adopted. As discussed earlier, the detection performance of CFAR methods is easily affected by the various non-homogeneities of the environment. Moreover, the sliding window technique cannot effectively differentiate between clutter and target pixels and easily leads to a high computation load. In this thesis, we propose new non-guard CFAR ship detection methods for SAR images, which introduce censoring techniques to CFAR detectors to resolve the aforementioned drawbacks.

The study incorporates both simulated and real SAR scenes in its analysis, in order to thoroughly examine and compare the effectiveness of the proposed methods in different scenarios. By using simulated and real data, the study aims to establish a comprehensive understanding of the performance of the method under varying conditions, and provides insights into its potential applications in real-world situations.

As a detector's processing time is important in SAR ship detection. Fast and efficient detection of ships is essential. Long processing times can lead to delays in decision making, which can have serious consequences in time-sensitive situations. Therefore, it is important to have detectors that can rapidly and accurately detect ships in SAR scenes in order to ensure efficient and effective operations. This ensures shorter revisit time and the possibility to manage RT (Real Time) or NRT (Near Real Time) monitoring activities. Therefore, the new detectors have been specifically designed with low time costs. By leveraging advanced algorithms, the new detectors are able to quickly and accurately detect ships in SAR scenes. This means that decisions can be made faster and more efficiently, without sacrificing accuracy, making them ideal for time-sensitive applications such as maritime surveillance, search and rescue operations and environmental monitoring.

1.3.1 Publication summary

The main body of this thesis is based on three journal papers and two IEEE (Institute of Electrical and Electronics Engineers) conference proceedings. The articles listed are a collection of scholarly works that were written over the course of the PhD program. They represent a substantial contribution to the field of automatic CFAR target detection and highlight the research progress and achievements made throughout the PhD journey. Each article is presented in chronological order, making it easy to see the evolution of the research over time. The conference papers presented during this PhD are also reported. In addition to the order, a brief summary has been provided for each article, giving an overview of its content and main findings. These summaries serve as a convenient reference for those who may not have time to investigate the full texts, but still wish to gain a general understanding of the research. Overall, the articles represent a comprehensive body of work that showcases the depth and breadth of the PhD research program.

Journal Papers

1. **Hicham Madjidi**, Toufik Laroussi, Faiçal Farah. ”On Maximum Likelihood Quantile Matching CFAR Detection in Weibull Clutter and Multiple Rayleigh Target Situations: A Comparison,” Arabian Journal for Science and Engineering (2022): 1-9.

   The QM-CFAR (Quantile Matching-CFAR) detector for a Weibull background is introduced in this paper. In particular, assuming a non-stationary Weibull clutter with or without interfering targets, the QM and MLE (Maximum Likelihood Estimator) are used concurrently to allow the proposed detector to perform robustly in multiple target situations with *a priori* unknown Weibull parameters. That is, we first rank order the reference samples in order to choose quantile information that has the same clutter characteristics as the CUT (Cell Under Test) and remove any outliers from the data. The parameters are then obtained using the QM and the MLE. Finally, we carry out target decision-making. The subsequent CFAR detection threshold provides for fixed censoring of the top end of the reference window. MC (Monte-Carlo) simulations reveal that, when compared to contemporary existing CFAR algorithms, the QM-CFAR detector gives more robust and more accurate estimations of the Weibull distribution parameters, and achieves reduced P_D deterioration in multiple target circumstances

[21].

2. **Hicham Madjidi**, Toufik Laroussi, Faiçal Farah. "A Robust and Fast CFAR Ship Detector Based on Median Absolute Deviation Thresholding for SAR Imagery in Heterogeneous Log-normal Sea Clutter," Signal, Image and Video Processing (2023): 1-8.

   The MAD-CFAR (Median Absolute Deviation-CFAR) detector is introduced in this paper for ship detection in SAR images immersed in heterogeneous log-normal clutter. The SDM (Standard Deviation around the Mean) is a well-known data spread metric that can be greatly influenced by strong and/or weak outliers, as well as non-Gaussianity of the background clutter. To address this issue, we use the absolute deviation around the median, also known as the MAD metric, which is more resistant to outliers in multiple target situations. The MAD-CFAR detector shows robust false alarm regulation and high detection in a heterogeneous log-normal background when compared to the performances of contemporary CFAR detectors on both simulated and real SAR images [22].

3. **Hicham Madjidi**, Toufik Laroussi. "Approximate MLE Based Automatic Bilateral Censoring CFAR Ship Detection for Complex Scenes of Log-Normal Sea Clutter in SAR Imagery," Digital Signal Processing (2023): 1-15.

   In this paper, we propose and examine the automatic bilateral censoring and detection capabilities of the AML-CFAR (Approximate Maximum Likelihood-CFAR) detector in complex scenes of log-normal sea clutter. That is, resorting to linear biparametric adaptive thresholds for both censoring and detection algorithms, we introduce a logarithmic amplifier to get a transformed Gaussian distribution. We first compute the lower and upper censoring thresholds using the closed form solutions of the AML estimates of the unknown mean and standard deviation parameters by assuming a homogenous middle half ranked sub-SRW (Sliding Reference Window). After censoring both ends, we utilize the remaining data to estimate the unknown distribution parameters using the same expressions as the AML estimates to get the detection threshold. Extensive simulations on both simulated and real SAR images reveal that the AML-CFAR detector outperforms its competitors' state-of-the-art detectors [23].

International Communications

1. **Hicham Madjidi**, Toufik Laroussi, and Faiçal Farah. "A CFAR Detection Algorithm

for Weibull and Lognormal Clutter Mixture in SAR Images," In 2022 19th International Multi-Conference on Systems, Signals & Devices (SSD), pp. 286-291. IEEE, 2022.

The paper proposes a CFAR detector for SAR clutter images based on a WLMM (Weibull Lognormal Mixture Model). The clutter parameters of the mixture and the accompanying percentiles are first calculated using MLEs. Then, an adaptive threshold is set to keep the P_{FA} constant. The SA (Simulated Annealing) optimization approach is used to efficiently shorten the searching time and estimate the global optimal percentiles. The application of the proposed CFAR framework to a real-world image, namely the MSTAR BTR 60 (Moving and Stationary Target Acquisition and Recognition Bronetransporter), demonstrates that an optimum weighting yields a good detection [24].

2. **Hicham Madjidi**, Toufik Laroussi, and Faiçal Farah. "CFAR Ship Detection in SAR Images Based on the Generalized Rayleigh Mixture Models," In 2022 M'sila. IEEE, 2022.

In this paper, we employ the GRMM (Generalized Rayleigh Mixture Model) to describe sea clutter and estimate the CFAR threshold in the same way as we did in [24]. Furthermore, to address the issue encountered in traditional window-based CFAR detectors, we create a binary censorship map that specifies pixels that should not be used for background modeling. This would prevent the clutter statistics from deteriorating owing to neighboring target pixels [25].

1.4 Thesis Structure

The rest of this thesis is organized as follows. In chapter 2, after a brief presentation of the conventional radar systems, we lay the foundations of radar imagery necessary for understanding the information contained in SAR images. In chapter 3, we first recall the statistical models of the radar clutter under different sea conditions and grazing angles of radar beams used in radar detection along with target models. Then, we discuss how selecting the best fitting distribution by using the term Goodness of fit test. Lastly, we discuss the basic concepts of adaptive CFAR detection as well as the adaptativity of the detection threshold.

In chapter 4, 5 and 6, novel CFAR detectors, for complex environments, are derived. MC simulations are performed to compare the new CFAR detectors with classical CFAR ones in terms of ROC (Receiver Operating Characteristics) curves and computational time. In addition, the same algorithms are compared through real datasets acquired from different sensors (Sentinel-1, TerraSAR-X and ALOS-2 SAR) and outcomes are compared with GT (Ground Truth).

Chapter 2

Remote Sensing Radar Imaging

Summary

After a brief presentation of the conventional radar systems used to acquire the data, the main objective of this second chapter is to lay the foundations of radar imagery necessary for understanding the information contained in SAR images. First, we summarize the physical bases of radar imagery before presenting the principle of SAR image formation. Particular interests are given to explaining the signal processing methods used to achieve increasingly small resolutions, namely pulse aperture synthesis. Then, various specific properties of SAR data, namely, speckle noise, geometric and radiometric are summarized. Finally, we conclude with a presentation of the different types of SAR data.

2.1 Introduction

Before we examine the peculiarities of radar imaging systems, let us first look briefly at their origins and history. The origin of radar can be traced back to the experiments of Heinrich Hertz in 1886, in which he demonstrated that radio waves could be reflected by metallic objects. Shortly after, in 1904, German inventor Christian Hülsmeyer was the first to put these findings to use by constructing a simple ship detection device, aimed at avoiding collisions during foggy conditions. In the 1920s and 1930s, experimental ground-based pulsed radars were developed for detecting objects at a distance [2].

The effectiveness of a radar system depends in part on the manufacturers, the operator, and the conditions under which it operates. The manufacturers must properly calculate data such as transmitter power, receiver sensitivity and the type of airborne material used. The operator, on the other hand, must make the best use of the equipment provided. For example, he must choose the location of his radar station so that it is not obstructed by surrounding objects such as hills, cliffs or tall buildings. It is also necessary to move it away as much as possible from the interfering sources such as other radars for example. There are, however, other factors that can interfere with the proper functioning of the radar and over which the manufacturer and operator have no control. Among these exogenous factors, we can quote, Fig 2.1, the atmospheric conditions, the dimension and the shape of the object to be detected, the sphericity of the ground and the interferences caused by solar and cosmic radiations or other systems of jamming produced by man. The detection and display of an echo signal is often accompanied by this unwanted information appearing simultaneously on the display screen. These may be echoes from other objects or electrical interference, usually referred to as noise from external electrical installations or from the radar itself [26].

The specific role of radar is to determine which of the received echoes is useful (target echo). If the radar is used for meteorological research, the echoes reflected by rain and clouds can be considered interesting, whereas the echoes reflected by aircraft are considered undesirable. On the other hand, if the radar is used for enemy aircraft detection, echoes reflected from rain and clouds become undesirable [26].

Unlike a simple radar, which only detects the presence and location of an object, imaging radar can create detailed images of the target area, providing information about its size, shape, and surface features. Early imaging radars deployed during WWII (World War II)

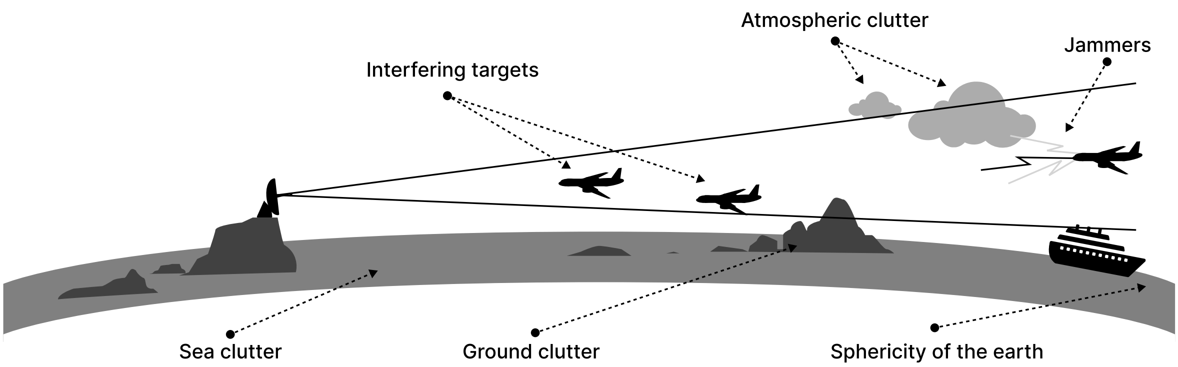

Figure 2.1: Schematic representation of activities and impacts in a coastal zone.

included revolving sweep screens that were utilized for aircraft identification and placement. After WWII, SLAR (Side-Looking Airborne Radar) was developed for military surveillance and reconnaissance, imaging a strip of ground parallel to and offset to the side of the aircraft during flight. In the 1950s, also for military purposes advances in SLAR and the development of higher resolution SAR were developed. These radars were declassified in the 1960s and began to be utilized for civilian mapping applications. Since then, various airborne and spaceborne radar systems for mapping and monitoring purposes have been developed [2].

2.2 Radar systems

A radar system is a device used for detecting and tracking objects, typically by emitting high-frequency radio waves and measuring the reflection (echo) from the target. The basic principle of radar operation is straightforward. A transmitter sends out a short burst of radio waves, and the receiving antenna listens for an echo. The time it takes for the echo to return is used to calculate the distance of the target, while the frequency shift (Doppler effect) in the returning signal is used to determine its velocity. The radio waves are therefore emitted into space in repetitive pulses at regular intervals called Pulse Repetition Interval TR (PRI). In order to avoid the so-called second time around echo effect, the receiver, sharing the same antenna with the transmitter, must not only be inhibited for the entire duration τ of each transmitted RF pulse, but also, they should have a power and Pulse Repetition Frequency f_R (PRF) so as to minimize any risk related to a propagation anomaly. This anomaly can be caused by the location of the radar and/or particular weather conditions. Each time an object located in the scanning space (main beam) of the radar is hit by the RF (Radio

Frequency) wave, a part of the electromagnetic energy is reflected and then analyzed by the receiver becoming operational during the interval separating two successive pulses called listening time $(T_R - \tau)$ [26].

The types of radar systems can vary based on the frequency band used (L, S, C, X, Ku, Ka, etc.), the method of wave generation and reception (pulsed or continuous wave), and the specific design of the antenna (parabolic, phased array, etc.). Different frequency bands are used for different purposes, with higher frequency bands providing higher resolution but limited penetration of solid objects, while lower frequency bands provide longer range but lower resolution. Pulsed radar emits short bursts of radio waves, with the receiver listening for echoes during the gaps between transmissions. Continuous wave radar emits a constant radio frequency, with the receiver measuring the frequency shift in the returning signal to determine target velocity. Different antenna designs are used to achieve different radiation patterns and beam shapes, with parabolic antennas providing high gain and directional coverage, and phased array antennas capable of rapidly steering the beam and providing electronic beamforming capabilities. Overall, radar systems play an important role in many areas, providing information about the location, velocity and characteristics of objects in the environment. Advances in radar technology continue to expand the capabilities and applications of radar, with the development of new frequency bands, waveforms, and antenna designs providing increased performance and versatility.

Imaging radar systems are a type of radar system that uses radar technology to produce images or maps of objects or areas. They work by emitting RF signals and measuring the reflection of those signals off of objects in the environment. The resulting data is then processed to produce an image of the target. There are two main types of imaging radar systems, namely Real Antenna Radar RAR (Real Aperture Radar) and SAR [27].

RAR systems, often refer to SLARs, use a physically large antenna to produce images, while SAR systems use smaller antenna elements and processing techniques to synthesize a large antenna, which provides high-resolution images. Both real aperture and synthetic systems are side looking perpendicular to the flight axis of the carrier, but differ in obtaining the azimuthal spatial resolution, i.e. the resolution along the flight axis.

Imaging radar systems are used in a variety of applications, including military surveillance, environmental monitoring, and remote sensing. They are particularly useful for their ability to penetrate clouds and provide images in adverse weather conditions, as well as for producing high-resolution images. Additionally, imaging radar systems can operate day or night and do not require visible light to produce images, making them useful for observing objects in low-light or nighttime conditions. Overall, imaging radar systems play an important role in many fields by providing valuable information and images of objects and areas that are difficult or impossible to observe using other technologies [28].

2.2.1 Components of a Pulse Radar System

Radar system design varies depending on function. However, the fundamental functioning and core set of subsystems in a conventional radar system are alike. Fig 2.2 shows a block diagram of a typical radar system showing the main components, i.e., transmitter, receiver, power supply, synchronizer, duplexer, antenna and display [29].

Transmitter: The transmitter generates the RF signals that are transmitted by the radar antenna.

Antenna: The antenna is responsible for radiating the RF energy into space and receiving the echoes that are reflected back from targets in the environment.

Receiver: The receiver is responsible for detecting the echoes that are reflected back from targets in the environment.

Power Supply: The Power Supply provides the electrical power to operate the various components, such as the transmitter, receiver and processor.

Synchronizer: The synchronizer is responsible for coordinating the timing of various operations within the radar system, such as the rate at which pulses are sent, i.e., sets PRF,

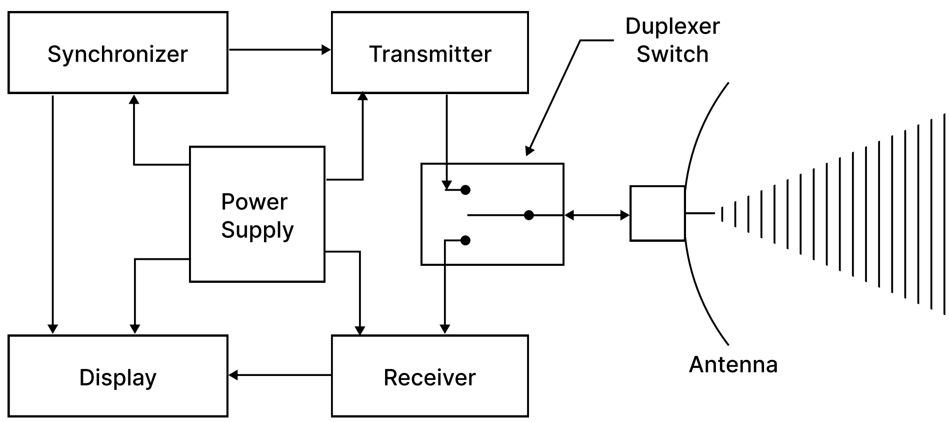

Figure 2.2: Schematic representation of activities and impacts in a coastal zone.

the processing of the received signal, the display of the processed information and resets the timing clock for range determination at the end of each pulse.

Duplexer: A duplexer is a device that allows the radar's transmitter and receiver to share a common antenna.

Display Unit: The display unit is responsible for presenting the radar data to the operator.

Overall, the components of a radar system work together to generate, transmit, receive, process and display radar data, providing information about the range and velocity of targets in the environment.

2.2.2 Characteristic parameters of an RF pulse

In the pulse radar, Fig 2.3, there are a number of parameters that characterize the emitted RF wave and whose choice is crucial for its proper functioning [26].

Distance measurement

If an electromagnetic wave, traveling at the speed of light $C = 3 \times 10^8$ m/s, takes Δt to hit an object and return. Then this object is at a distance D of the radar, equal to

$$D = \frac{c\ \Delta t}{2} \tag{2.1}$$

The factor $\frac{1}{2}$ accounts for the round trip of the pulse. If $\Delta t > T_R$, then there is ambiguity in the distance measurement (second echo return effect).

$$D_{\max} = \frac{c\ T_R}{2} \tag{2.2}$$

Azimuth (bearing) and elevation (site) angle measurements: Pulse radar calculates the bearing and location of an object from the direction in which the antenna must be pointed to obtain a maximum reflected signal from.

Height measurement: The height or altitude of an object is calculated by multiplying the slant distance of the object by the sine of its elevation angle.

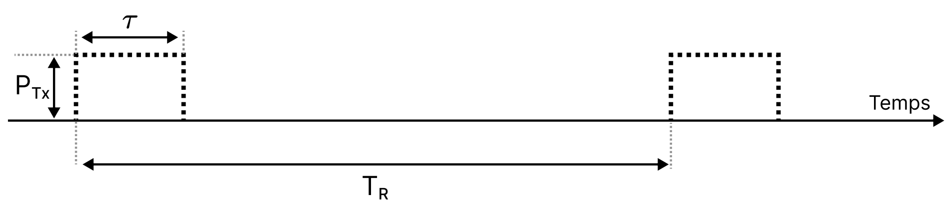

Figure 2.3: Chronogram of the emission of a radar pulse.

2.3 Radar Backscatter

The basic idea behind imaging radar systems is to use electromagnetic radiation as a means of gathering information about the Earth's surface. One of the characteristics of electromagnetic waves is that they are (partially) reflected (backscattered) when they come into contact with a barrier, such as a building, sea, etc. The process involves transmitting electromagnetic waves towards the surface and then measuring the amount of radiation that is reflected back. Part of the energy of the emitted electromagnetic wave is absorbed by the objects. The rest of this incident energy is radiated by the object as a new electromagnetic wave with different characteristics (amplitude, phase and polarization) from those received by the objects. This reflected radiation carries information about the surface. Its properties are defined by various characteristics such as wavelength, frequency and polarization. These characteristics determine how the wave interacts with the surface and how the information is encoded in the returned signal. In this way, imaging radar systems allow us to obtain a picture of the Earth's surface and extract valuable information from it. The electromagnetic wave is characterized by the direction of propagation, amplitude, wavelength, polarization and phase [27].

An imaging radar generates an image in which each pixel represents the strength of the electromagnetic radiation backscattered by the radar-illuminated Earth's surface. The image's darker portions show low backscatter, while the brighter areas represent strong backscatter. Bright characteristics indicate that a significant amount of radar energy was reflected back to the radar, whilst dark features indicate that relatively little energy was reflected. Backscatter for a target region at a specific wavelength will change depending on a number of factors, including the size of the scatterers in the target area, the moisture content of the target area, the polarization of the pulses, and the observation angles. When various wavelengths are employed, the backscatter will likewise change. Using the following formula, the radar equation calculates the mean power backscattered at every location in the image [30, 31, 26].

$$P_{Rx} = P_{av} \frac{G_{Tx} G_{Rx} \lambda^2}{(4\pi)^3 r_{Tx}^2 r_{Rx}^2} \sigma_{\text{target}} \tag{2.3}$$

where $G_{Tx} = G_{Rx}$ denotes the directivity or directive gain, of the transmit and receive antenna, $r_{Tx} = r_{Rx}$ the distance between the imaged surface and the transmit/receive antenna,

P_{Rx} the average power received by the radar, P_{Tx} the power emitted by the radar, λ the wavelength of the electromagnetic wave, σ_{target} the average target RCS (Radar Cross Section) in units of square meters, which is defined as the ratio between the incident and received signal intensity [32]

$$\sigma_{\text{target}} = \frac{I_{\text{received}}}{I_{\text{incident}}} 4\pi r^2 \tag{2.4}$$

In addition to being attenuated, the backscatter is systematically contaminated by noise (unwanted or disturbing information that interferes with the signal being transmitted or received). Most of this noise comes from the electronic components, and is thus qualified as thermal noise. This can result in degradation of the signal quality and can make it more difficult to extract useful information from the signal. Noise power is of the form [27, 33]

$$P_n = \alpha k_B B_r T_0 \tag{2.5}$$

where α denotes a unitless quantity characteristic of the receiver (called the Noise Figure), k_B the Boltzmann constant (1.38×10^{-23} J/K), B_r the receiver bandwidth and T_0 the equivalent noise temperature of the receiver.

2.4 Factors influencing the radar backscatter

The radar backscatter from a target is influenced by its material properties, such as dielectric constant and conductivity, target geometry, incidence angle, polarization, surface roughness and thepresence of surface vegetation. These factors can interact and affect the backscatter in complex ways, making it difficult to predict its exact behavior. Understanding these factors is important for accurate radar imaging and target classification.

2.4.1 Frequency influence

The frequency of the radar signal has an influence on the radar backscatter. Different frequencies can penetrate different materials to varying degrees and can be affected differently by the target's electrical properties. Lower frequency radar signals, such as L-band, have a longer wavelength and can penetrate through vegetation and other materials, making them useful for remote sensing applications where the penetration is desired. Higher frequency radar signals, such as X-band, have a shorter wavelength and are more sensitive to the target's surface characteristics, making them useful for high-resolution imaging applications.

In other words, the more the frequency decreases (the more the wavelength increases), the greater the depth of penetration is.

Fig 2.4 depicts a conceptual overview of the effect of sensor wavelength λ on signal penetration into various surface types. Radar signals penetrate deeper as sensor wavelength rises. This is due to the dependency of the dielectric constant ε_r on the incident wavelength, which allows for greater penetration in the L-band than in the C- or X-bands. Consider a forest with a wavelength of 3 cm (X Band), where the wave finishes at the level of the trees' first leaves. As a result, the information in the image is connected to the crowns of the trees. The wave, on the other hand, penetrates the foliage and tiny branches with a wavelength of $\approx$ 23 cm (L Band). The information is then fundamentally connected to the tree trunks or the underlying earth. As a result, longer wavelength systems should be utilized to characterize vegetation characteristics (e.g., vegetation structure, biomass, etc.) [27].

The wavelengths used in radar imagery are listed in Table 2.1. The portion of the electromagnetic spectrum used in radar imagery covers a wavelength ranging from meters to centimeters. The frequency band used must comply with IEEE standards. While the center frequency and signal bandwidth are regulated by the ITU (International Telecommunications

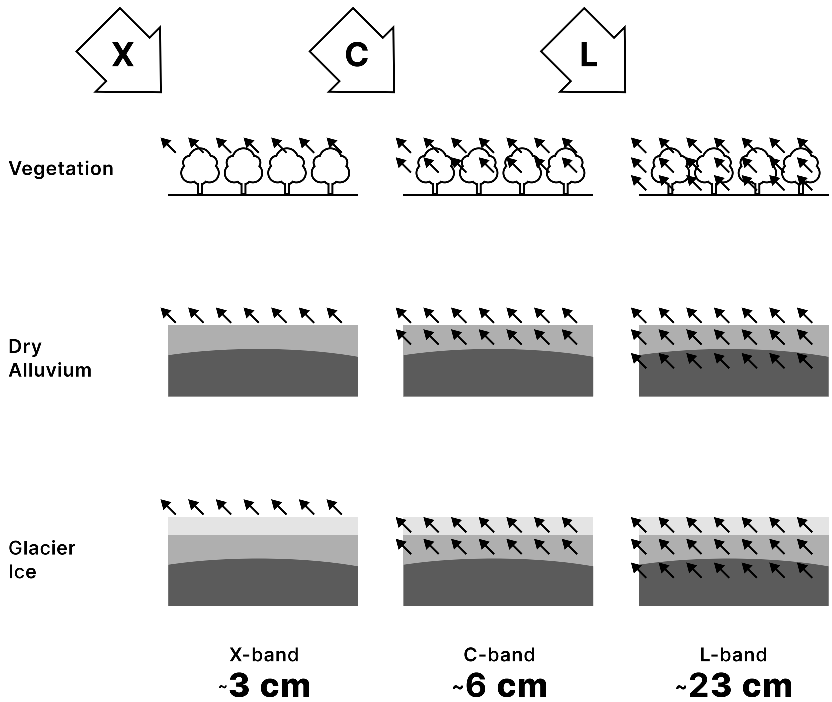

Figure 2.4: Radar backscattering mechanisms for different SAR X-, C- and L-band wavelengths λ.

Table 2.1: Radar frequency bands that are frequently employed, along with the corresponding frequency and wavelength ranges.

Frequency Band	Ka	Ku	X	C	S	L	P
Frequency [GHz]	40-25	17.6-12	12-7.5	7.5-3.75	3.75-2	2-1	0.5-0.25
Wavelength [cm]	0.75-1.2	1.7-2.5	2.5-4	4-8	8-15	15-30	60-120

Union) [34]. The microwave region of the spectrum is quite large, relative to the visible and infrared, and there are several wavelength ranges or bands commonly used which were given code letters during WWII, and remain to this day.

2.4.2 Polarization Influence

An important concept in radar imaging is the notion of polarization. Along with the wavelength, its choice has a great influence on the nature of the information in the SAR image. As shown in Fig. 2.5, the polarization of the electromagnetic wave refers to the orientation of the electric field vector E with respect to the target surface. The incidence plane is defined as the plane perpendicular to the observed surface. When the direction of E is perpendicular to the plane of incidence, it is called horizontal polarization. When the direction of E is parallel to the plane of incidence, we speak of vertical polarization [27].

Polarization setups vary between imaging systems. However, the most common configurations are linear polarization configurations HH, VV, HV, or VH, with the first term referring to the polarization at wave emission and the second term referring to the polarization at wave receipt. In other words, radar can transmit pulses in either horizontal (H) or vertical (V) polarization and receive in either H or V, with the resultant combinations of HH (Horizontal transmit, Horizontal receive), VV, HV, or VH.

Thus, the exploitation of polarimetric data provides information on these depolarization properties of a surface or an object. The polarimetric information is complete and fully exploitable if we have for a surface its response to the four preceding combinations of polarizations. From the knowledge of these quantities, is generally deduced the backscattering matrix of the target or surface which gives various information relating to their electrical properties, such as the type of dominant backscattering mechanisms, soil moisture content, permittivity, roughness, etc.

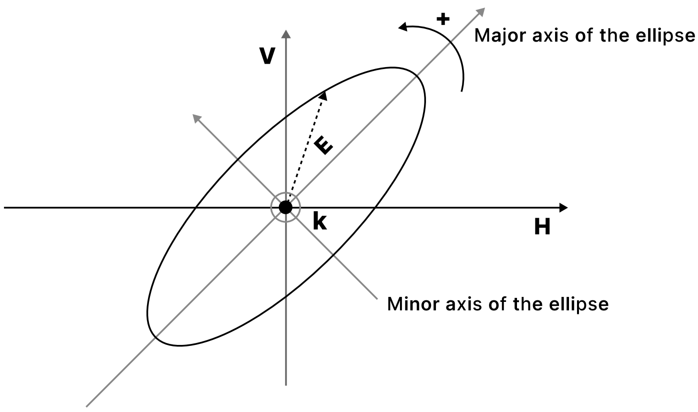

Figure 2.5: Wave polarization.

2.4.3 Surface Roughness Influence

The backscatter coefficient, also known as the RCS, is a measure of the amount of energy that is scattered backwards by a target when it is illuminated by a beam of electromagnetic radiation, such as light or radar. The backscatter coefficient is a complex quantity that depends on various factors such as the frequency, polarization and angle of incidence of the illuminating radiation, as well as the physical and electromagnetic properties of the target.

The idea of surface roughness is inextricably linked to the concept of backscatter coefficient. It represents the capacity of the surface to return more or less energy to the sensor. The degree of roughness of a surface varies with wavelength. If the roughness scale of a randomly rough surface is defined as the standard deviation of the height deviation h from some mean height h of the surface, the issue of how large h must be for a surface to seem rough to an imaging radar system may be addressed. The Fraunhofer criterion defines a surface as rough if the height deviations surpass the value through, which is determined by [32]

$$h_{\text{rough}} > \frac{\lambda}{32\ \cos\theta_i} \tag{2.6}$$

Fig. 2.6 depicts the concept of wavelength-dependent roughness by depicting increasing roughness conditions from left to right and identifying the transition from smooth, Fig. 2.6a, to intermediately rough, Fig. 2.6b, to rough surfaces, Fig. 2.6c, in accordance with the

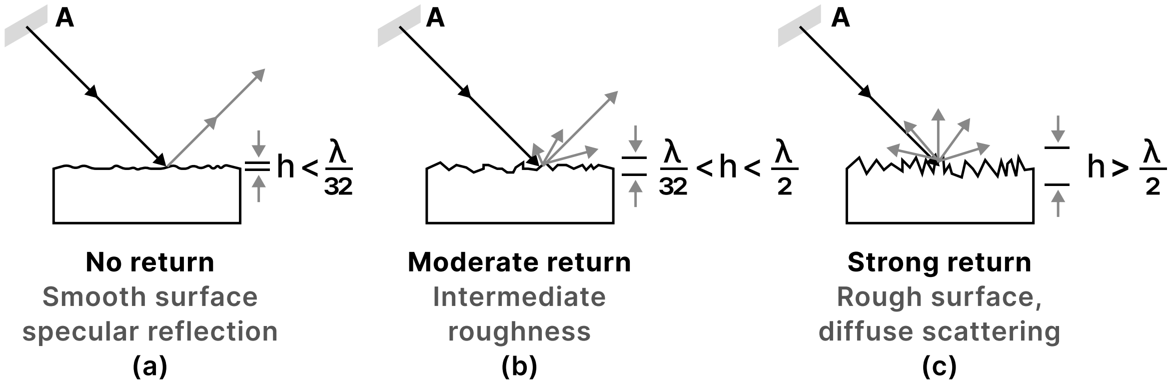

Figure 2.6: Sketch illustrating the relationship between surface roughness and sensor wavelength, (a) smooth, (b) intermediate, and (c) rough.

Fraunhofer criterion of Eq. (2.6). Backscatter rises with roughness (length of gray arrows pointing toward sensor). Hence, rough surfaces (at wavelength λ) have greater RCS than intermediately rough or smooth surfaces. The wavelength dependency also indicates that when the wavelength increases from X-band ($\lambda = 3.1$ cm) to C-band ($\lambda = 5.66$ cm) to L-band ($\lambda = 24$ cm), the surface will seem darker [32].

Furthermore, because of the surroundings as well as the shape and size of the target, the interaction of the radar signal with the target is frequently more complicated. In marine applications, for example, different scattering scenarios of a vessel on the sea surface are depicted in Fig. 2.7. A man-made vessel is often built with flat metal surfaces that operate as mirror reflectors for most radar signals. As a result, when the surfaces are tilted towards the radar, a high direct reflection, also known as single-bounce, occurs, as shown in Fig. 2.7a. On most other angled surfaces, radar signals are likely to bounce between the vessel and the sea surface before returning to the radar sensor, resulting in more complex scattering scenarios, as illustrated in Figs 2.7b–2.7d. [8].

2.5 SLAR

A SLAR is a type of radar that is mounted on an aircraft and used to obtain images of the terrain below. Unlike conventional radar, which points straight down towards the ground, SLAR (and any other imaging radar) system is pointed away from Nadir by a so-called side-looking angle θ_l, such that it illuminates a continuous swath on the ground as the aircraft moves along, providing a lateral view of the terrain as shown in Fig 2.8. This side-looking

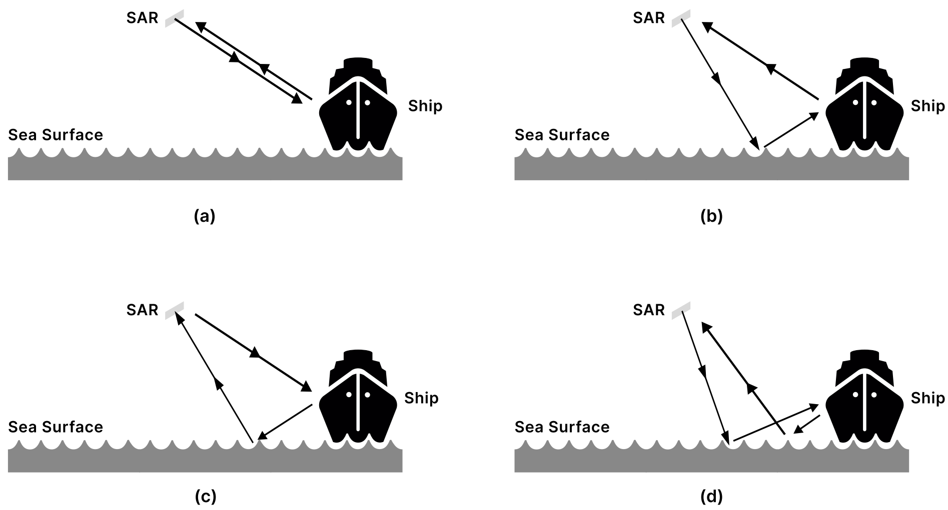

Figure 2.7: Different surface scattering situation for vessel over sea surface.

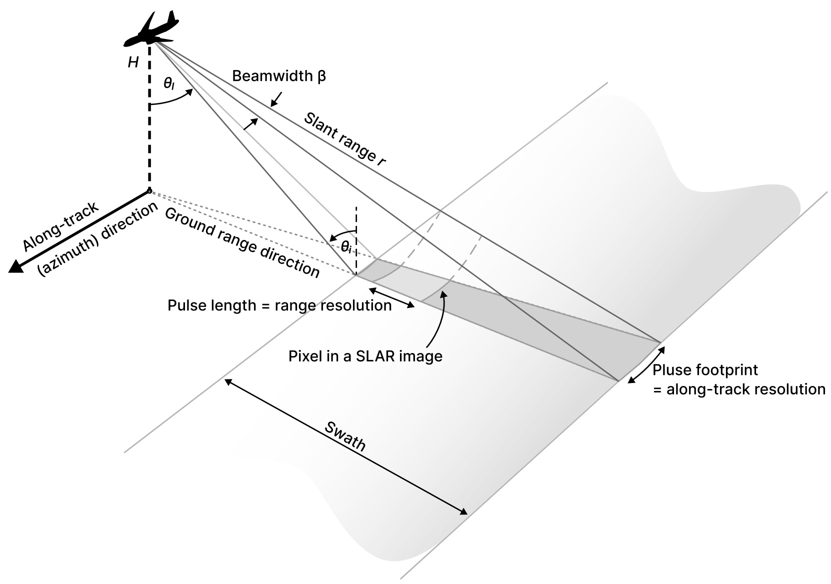

Figure 2.8: Observation geometry of a SLAR imagery.

configuration is necessary to eliminate right-left ambiguities from two symmetric equidistant points.

The radar travels in a straight line at height H, observing Earth from an oblique look angle θ_l. Instead of the look angle, the incidence angle $\theta_i = (90^\circ - \theta_l)$ is sometimes annotated. The lighted footprint's size is determined by the antenna beamwidth β and the distance between the satellite and the ground R. It is worth noting that the radar beam is broad in range but narrow in azimuth. The forward motion of the flying platform facilitates image generation.

While the platform (aircraft or satellite) of a SLAR travels forward in the flight direction with the nadir directly beneath the platform, the radar system is transmitting a sequence of short microwave pulses of pulse width τ. The microwave beam is transmitted obliquely at right angles to the direction of flight illuminating a swath, each of which illuminates an instantaneous area on the ground that is usually referred to as the antenna footprint S, the dark gray area in Figure 2.8. The instantaneous footprint size is important as it determines the spatial resolution of the radar image and the coverage of the area being imaged, that is largely defined by [32]

$$S \approx \frac{\lambda}{L} r = \beta r \tag{2.7}$$

where λ defines wavelength, L the side length of the antenna, r distance of the radar sensor from the ground and $\beta = \frac{\lambda}{L}$ antenna's beamwidth.

Swath width refers to the strip of the Earth's surface from which data are collected by a SLAR. It is the width of the imaged scene in the range dimension. The longitudinal extent of the swath is defined by the motion of the aircraft with respect to the surface, whereas the swath width is measured perpendicularly to the longitudinal extent of the swath, which can be approximated by [35]

$$S_W \approx \frac{h\beta}{\cos^2 \theta_l} \tag{2.8}$$

where h denotes the height of the satellite orbit above the Earth (altitude) and θ_l is the radar look angle. This expression assumes that $\beta << 1$ and does not take into account the Earth's curvature.

The echo backscattered from each ground cell within the footprint is received and recorded as a pixel in the image plane based on their arrival time in both the range (distance) and azimuth (horizontal) directions, which is what determines the distance resolution and azimuth resolution of the radar image. The resulting two-dimensional representation provides a map of the terrain and objects, with each pixel in the image representing the strength of the radar signal reflection at a specific location. These images can be used to identify features such as topography, vegetation, and man-made structures. The image resolution of a radar system is determined by several factors, including the frequency of the radar signals, the bandwidth of the radar signals, the pulse duration, and the receiver noise level.

2.5.1 Image Resolution

The degree of detail shown in a radar image is referred to as image resolution. It measures how well the radar system can identify and discriminate objects within an image. Several factors influence the resolution of a radar image, including the frequency of the radar signal, the size of the antenna, and the altitude of the radar platform. The resolution of a radar sensor has two dimensions, namely the range resolution and the azimuth resolution. Built-in radar and processor constraints dictate azimuth resolution, which is proportional to the length of the processed pulse, with shorter pulses resulting in "higher" resolution. The angular beam width of the terrain strip illuminated by the radar beam determines range resolution.

Range Resolution

In the range direction, echoes from the ground arrive progressively later from the near-range to the far-range edge of the swath, describing the capacity of a SLAR system to identify objects at varied (slant) distances from the radar [32]. If the respective echoes of two points are separated by a time difference τ, their range resolution is given by [34, 32]

$$\rho_R = \frac{c\tau}{2} \tag{2.9}$$

The variable ρ_R in Eq. (2.9) is usually referred to as the slant range resolution of a SLAR system as it describes a SLAR's ability to distinguish objects at different (slant) distances from the radar. While the slant range parameter ρ_R is useful for many system design questions. That is, remote sensing is often more interested in the ground range resolution ρ_G, which describes the ability to discriminate objects that are situated on the ground. If we project ρ_G onto the ground with incidence angle ($\theta_i \neq 0$), we get the ground range resolution which is coarser than the slant range resolution [34, 32]

$$\rho_G = \frac{\rho_R}{\sin\theta_i} \tag{2.10}$$

Eq. (2.10) demonstrates that the ground range resolution ρ_G does not remain constant across the swath and instead increases with increasing distance from Nadir (due to an increase in θ_i). This is in contrast to the behavior of typical optical systems, in which the ground resolution declines as θ_i increases [32].

Azimuth Resolution

The ability to discern objects in the azimuth direction, that is, on a constant delay line, is referred to as azimuth resolution. It is evident that this is equal to the width of the antenna footprint since echoes from all places along a line spanning that width are returned at the same time, which is then restricted by the antenna's side length L_{Az} in this direction. As a result, the azimuth resolution is equal to [32, 34, 35]

$$\rho_{Az} = S_{Az} \approx \frac{\lambda}{L_{Az}} r = \beta_{Az} r \tag{2.11}$$

where β_{Az} is the antenna beamwidth in azimuth.

Eq. (2.11) indicates that the azimuth resolution ρ_{Az} is linearly degrading with the increasing distance between the sensor and the ground R. To illustrate this, let assume a SLAR system operating at $\lambda = 23$ cm, utilizing an antenna of length L = 12 m at h = 800 km altitude and observing at a look angle $\theta = 20°$. This system achieves an azimuth resolution of $\rho_{Az} = 16.3$ km. Even if λ is as short as 2 cm, ρ_{Az} will still be equal to about 1.4 km; this is regarded as a low resolution for imaging applications. This is why, when high resolution is required, the real aperture approach is not employed from orbiting platforms. In order to improve the azimuth resolution, Carl Wiley, an engineer with the Goodyear Aircraft Corporation, made a crucial discovery in 1952 that provided a solution to the azimuth resolution issue plaguing existing SLAR technology. In technical words, he discovered a one-to-one correlation between a reflecting object's along-track location (relative to a transmitted radar beam) and the instantaneous Doppler shift of the signal reflected back to the radar by that object. He also proposed that a frequency analysis of the collected signals might allow for finer along-track resolution than current SLAR technology. All modern high-resolution imaging radar systems are based on Wiley's discovery, which was first known as Doppler beam-sharpening but is now more commonly known as aperture synthesis [32].

It's worth noting that the formula for calculating azimuth resolution in this context is comparable to the formula for theoretical resolution in optical sensors. The key difference is that optical sensors use a much smaller wavelength (λ) than what's used here, typically only a few microns, which enables them to achieve high resolutions (a few tens of meters) orbit space with small aperture sizes (just a few centimeters) [35].

2.6 SAR

As shown in Eq. (2.11), the azimuth resolution of a real aperture radar necessitates a large antenna dimension, which is impractical. In order to improve the azimuth resolution, a synthetic aperture technique is used. These systems achieve high azimuth resolution independent of slant range to target while using smaller antennas and relatively long wavelengths, resulting in an extraordinary improvement of the azimuth resolution (more than 30 times better employing the same antenna length) [36].

2.6.1 Basic SAR Principles

A SAR is a remote sensing imaging system whose primary output is to create two-dimensional images or three-dimensional reconstructions of objects, such as sea. Similar to a conventional radar, SAR works by transmitting pulses of radar energy towards the target and receiving the echoes that are reflected back. The radar antenna is mounted on a moving platform, such as a satellite or an aircraft, and the movement of the platform allows the radar system to create a synthetic aperture that is much larger than the physical size of the antenna. Due to the platform movement, the SAR's consecutive transmission/reception time translates into different positions. A suitable coherent combination of received signals enables the creation of a virtual aperture that is significantly greater than the physical antenna length. The name "synthetic aperture" comes from this fundamental characteristic of SAR, which also gives it the ability to function as an imaging radar. In the case of SAR the radar image results from processing the raw data, i.e., after forming the synthetic aperture, and represents a measure of the scene reflectivity [36].

Fig 2.9 depicts Wiley's typical SAR geometry, in which the platform moves at a constant velocity V along the azimuth or along-track direction, the slant range is the direction perpendicular to the radar's flight path, and the swath width represents the illuminated scene's ground-range extent [36]. While moving, it is constantly transmitting short radar pulses and receiving echoes returned from objects on the ground. Each radar pulse illuminates an instantaneous footprint of size S on the Earth surface. For spaceborne applications, the limited length L of the radar antenna Eq. (2.9) results in instantaneous footprints that typically measure several kilometers in size, resulting in the typical resolution limitation that plagues SLAR systems [32].

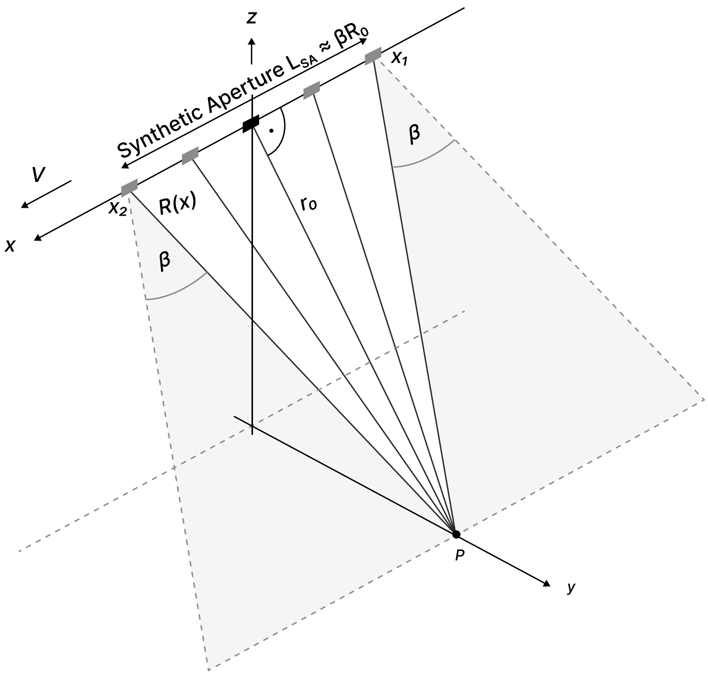

Figure 2.9: Geometry of observations used to form the synthetic aperture for target P at along-track position x=0.

In order to apply Wiley's aperture synthesis approach, we must first guarantee that an object P on the Earth's surface gets captured by numerous successive radar pulses as the antenna beam sweeps across the ground. This requirement is shown in Fig 2.9 by a series of antenna placements that illuminate object P as the sensor moves from point A (the first time P is seen) to point D (the final time P is seen). Following the acquisition of the radar data, a post-processing approach is used to combine all acquisitions between A and D into a single dataset that appears to have been acquired with a much longer antenna. The corresponding synthetic aperture length L_{SA} can be calculated via [32]

$$L_{SA} = \frac{\lambda}{L} r_0 \approx \beta r_0 \tag{2.12}$$

where r_0 is the minimum distance between the platform and the object. The above expression is equivalent to the footprint S illuminated by the (shorter) real antenna installed on the spacecraft (Cf. Fig 2.9). While the virtual synthetic aperture beamwidth is given by

$$\Theta_{SA} = \frac{\lambda}{2L_{SA}} \tag{2.13}$$

At any time t, the distance between the radar and illuminate object on the ground can be evaluated by applying the Pythagoras's theorem [36]

$$r(t) = \sqrt{r_0^2 + (vt)^2} \tag{2.14}$$

In general, the distance r_0 is significantly larger than vt during an object's illumination time on the ground; this permits extending $r(t)$ into a Taylor series and ignoring all except the first two terms, yielding the following approximation [36]

$$r(t) \approx r_0 + \frac{(vt)^2}{2r_0} \quad \text{for} \quad vt/r_0 \ll 1 \tag{2.15}$$

In the above formula, time, indicated by the variable t, is related with the platform movement and is frequently expressed as slow time. It should be noted that the quadratic approximation in Eq. (2.15) is done for convenience. Accurate SAR data processing considers the entire phase history without approximation. The azimuth phase is directly connected to the range fluctuation of a point target over time by [36]

$$\phi(t) = \frac{-4\pi r(t)}{\lambda} \tag{2.16}$$

where ϕ is the phase variation. The phase has also a parabolic behavior and the factor 4π is due to the two-way (round trip) range measurement of the SAR system [36].

Finally, the azimuth resolution of a SAR radar system can be computed according to [36, 35]

$$\delta_a = r_0 \Theta_{sa} = \frac{L_a}{2} \tag{2.17}$$

This corresponds to the highest resolution possible with the synthetic aperture. At first look, this finding appears to be somewhat uncommon. It demonstrates that the final resolution is unaffected by the distance between the sensor and the region being imaged. Furthermore, the equation suggests that a short antenna produces fine azimuth resolution. This is explained in the following manner [35]

- The longer the synthetic array, the larger the sensor's footprint on the ground. This results in a sharper synthetic beam that precisely balances the increase in distance.
- The smaller the antenna, the larger the footprint and the synthetic array. This results in a finer synthetic beam and, as a result, a finer resolution.

In contrast to optical sensors, viewing raw SAR data provides no relevant information about the scene. An image is obtained only after signal processing, as illustrated in Fig. 2.10, which outlines the fundamental SAR processing procedures. To put it simply, the entire process may be thought of as two distinct matched filter operations along the range

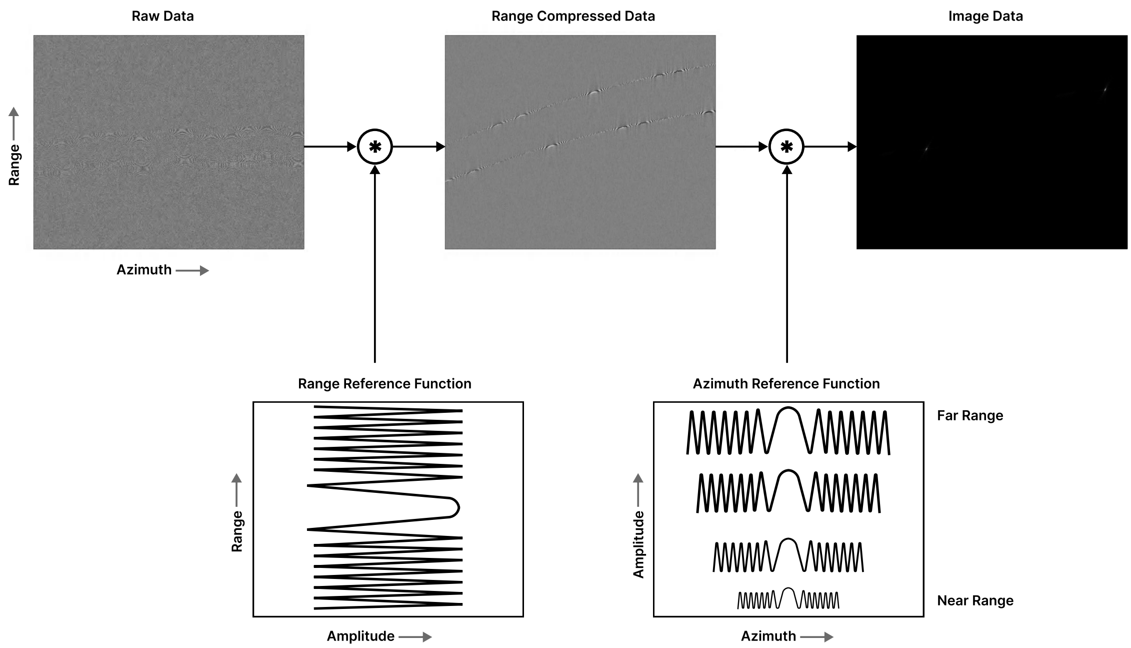

Figure 2.10: Summary of SAR processing steps where the range compressed data result from a convolution of the raw data with the range reference function. In a second step the azimuth compression is performed through a convolution with the azimuth reference function, which changes from near to far range. Here the "*" represents the convolution operation.

and azimuth dimensions. The first step is to compress the transmitted chirp signals to a single pulse. Due to the much lower computational load, a multiplication in the frequency domain is used instead of a convolution in the time domain. As a consequence, each range line is multiplied in the frequency domain by the complex conjugate of the spectrum of the transmitted chirp, yielding a range compressed image that displays just the relative distance between the radar and any point on the ground. The same basic logic applies to azimuth compression, i.e., the signal is convolved with its reference function, which is the complex conjugate of the response expected from a point target on the ground [36].

2.7 Radar Image Properties

2.7.1 Radar image geometry

The radar image has a geometry that results from the oblique perspective and the use of the round-trip time of the signal to position an object along the swath. To begin with, the image

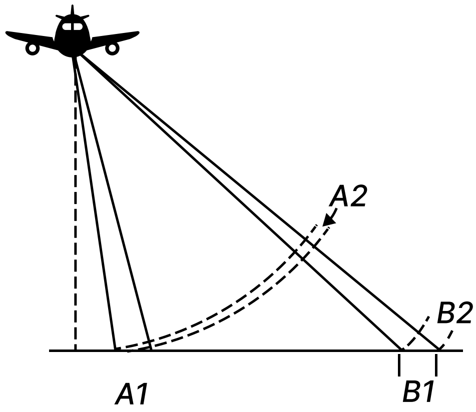

Figure 2.11: Side-looking viewing geometry.

geometry does not correspond exactly to the real geometry of the scene, but to the latter projected onto the incident wavefront. There are two types of geometry: "sensor geometry" images and "ground geometry" images. A geometric correction step is sometimes considered in order to project the image in real geometry (necessary for some applications such as image registration). This projection phase uses a digital terrain model, the angle of incidence as well as the size of the swath, to calculate in each pixel of the scene the geometric transformation to be made to the image to return to real geometry [37].

The viewing geometry of a radar, like that of other remote sensing devices, causes geometric distortions in the resulting images. However, there are significant differences in radar imagery due to the side-looking viewing geometry (Fig. 2.11), as well as the fact that the radar is fundamentally a distance measuring device, i.e., measuring range. Slant-range scale distortion happens when the radar measures the distance to slant-range objects rather than the real horizontal distance along the ground. This results in a shifting image scale from near to far distance. Targets A1 and B1 are of the same size on the ground, but their perceived dimensions in slant range (A2 and B2) differ. This causes targets in the close range appear compressed in comparison to objects in the long range. Ground-range distance may be computed using trigonometry using slant-range distance and platform altitude to convert to the correct ground-range format [2].

2.7.2 SAR Modes

The radar image has a geometry that depends on the data acquisition mode; a SAR system can operate in a variety of modes depending on the desired applications. The strip-map

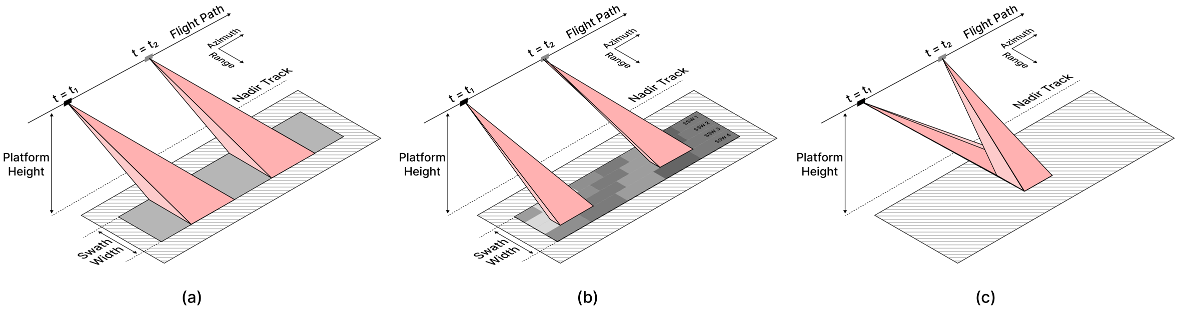

Figure 2.12: Illustration of different SAR operation modes which are used to increase the swath width (Scan SAR) or improve the azimuth resolution (Spotlight) compared to the Stripmap mode. (a) Stripmap (b) Scan SAR (c) Spotlight.

mode, in which the radar antenna beam is fixed, is the most basic acquisition mode. The radar antenna may be steered in both azimuth and elevation for various modes. Steering can be accomplished mechanically or electronically. This steering allows for improved azimuth resolution and longer or wider swath coverage. The most frequent SAR modes are briefly presented in the following paragraphs [30, 10]

Stripmap mode: In this mode, the antenna pointing direction is held constant as the radar platform moves in the azimuthal direction, as shown in Fig 2.12a. This acquisition mode makes it possible to generate an image of the area illuminated ROI by the radar for the duration of the acquisition;

Scan SAR: As illustrated in Fig 2.12b, this mode is a version of stripmap SAR in which the antenna is scanned in range several times during a synthetic aperture. This produces a considerably larger swath, but the azimuth resolution decreases (or the number of looks is reduced). The best azimuth resolution is obtained by multiplying the number of swaths scanned by the stripmap mode.

Spotlight SAR: The resolution of the stripmap mode can be enhanced by extending the angular extent of the illumination on the region of interest (a spot on the ground). This is accomplished by directing the antenna in a certain direction and focusing the radar signal on a small, well-defined region of the Earth's surface. To do this, the illumination beam's direction is electrically adjusted to keep the beam focused at the same region to be scanned, as illustrated in Fig 2.12c.

2.7.3 Speckle Noise

Speckle refers to the random fluctuations in radar backscatter that result in a granular appearance in the radar images. This is caused by the interference of multiple scattered radar signals from different points within the resolution cell that is strongly dependent upon the radar viewing angle, resulting in a speckled pattern. The speckle pattern can have a significant impact on the interpretation of radar images and can make it difficult to distinguish small-scale features or objects. To mitigate the effects of speckle, various image processing techniques, such as spatial averaging and multi-look processing, can be applied to the radar images to reduce the speckle noise and improve image quality.

Speckle is not strictly speaking noise, because it is fundamentally linked to the physical principle of measurement and cannot be reduced by improving the performance of the antenna used. However, it is often called "speckle noise" because in most applications it is a source of inaccuracy, which degrades the quality of an image and may make interpretation (visual or digital) more difficult. Thus, it is generally desirable to reduce speckle prior to interpretation and analysis [2]. The traditional method of reducing speckle noise is by processing images taken from different parts of the signal spectrum, and averaging the detected results [10]. This is called multilooking, and is discussed below.

2.7.4 Number of looks

In order to improve the visual quality of the images (which is a compromise between the geometric resolution and the radiometric resolution), it was necessary to find processes which make it possible to overcome the problems posed by the speckle in terms of radiometric resolution. Among these processes, one of the first used was the multilooking technique. The principle of this refers to the division of the radar beam (A) into several, in this example, five, narrower sub-beams (1 to 5) as shown in Fig 2.13 Each sub-beam provides an independent "look" at the illuminated scene, as the name suggests. Each of these "looks" will also be subject to speckle, but by summing and averaging them together to form the final output image, the amount of speckle will be reduced.

Speckle reduction filtering consists of moving a small window of a few pixels in dimension (e.g. 3×3 or 5×5) this is called the "number of looks", over each pixel in the image, applying a mathematical calculation using the pixel values under that window (e.g. calculating the

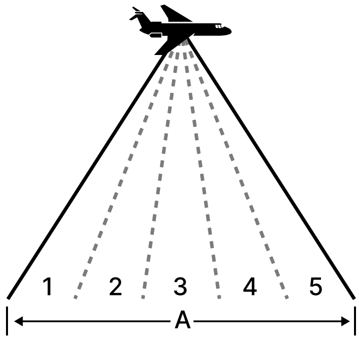

Figure 2.13: Independent looks and multilooking. The length of the synthetic aperture is A, which is divided into 5 sub-apertures [2].

average), and replacing the central pixel with the new value as shown in Fig 2.14. The window is moved one pixel at a time in both the row and column dimensions until the entire image is covered. A smoothing effect is achieved and the visual appearance of the speckle is decreased by computing the average of a small window surrounding each pixel.

From a radiometric perspective, the quality of the image improves when the number of looks N is increased. However, this comes at the expense of lower spatial resolution [38]. It's worth mentioning that when N exceeds 25, increasing it further only results in a small decrease in signal fluctuations. The small improvement in radiometric resolution should be balanced against the significant increase in spatial resolution. For example, if 10 resolution cells in a four-look image are averaged, the speckle noise is decreased to around 0.5 dB. Simultaneously, the image resolution will be reduced by an order of magnitude. Whether this loss in resolution is worth the reduction in speckle noise depends on both the aim of the

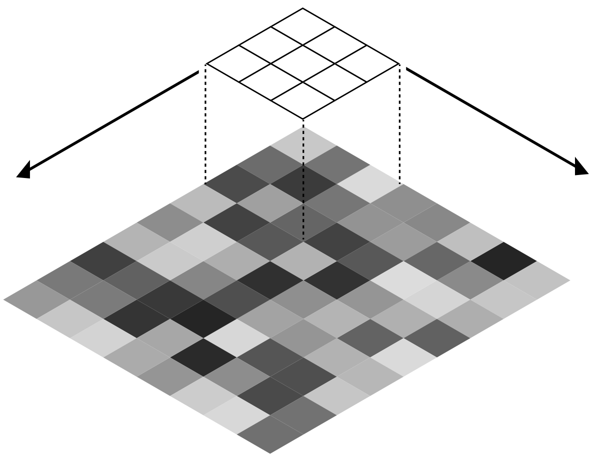

Figure 2.14: Multilooking window.

investigation, as well as the kind of scene imaged [35].

2.8 Satellite Imagery Data Sources

There are many satellite imagery data sources available today that can be used to read and manipulate (focus) RAW SAR data products. These include the following

- **Copernicus Open Access Hub** – Copernicus, previously known as GMES (Global Monitoring for Environment and Security), is the European Union's Earth observation program. More information and download: https://www.copernicus.eu/en/access-data
- **Sentinel Hub** – Sentinel Hub is an engine for processing of petabytes of satellite data. It is assisting hundreds of application developers globally and opens avenues for machine learning. For browsing, visualizing, and analysis, it makes Sentinel, Landsat, and other Earth observation imagery easily accessible. More information and download: https://apps.sentinel-hub.com/eo-browser/
- **ESA** – Earth observation data from the broad catalog of missions the European Space Agency (ESA) operate and support. More information and download: https://tpm-ds.eo.esa.int/oads/access/collection/
- **HRSID** – High resolution SAR images dataset (HRSID) is a data set for ship detection, semantic segmentation, and instance segmentation tasks in high-resolution SAR images. More information and download: https://github.com/chaozhong2010/HRSID
- **SAR Ship Dataset** - A SAR Dataset of Ship Detection for Deep Learning under Complex Backgrounds. More information and download: https://github.com/CAESAR-Radi/SAR-Ship-Dataset
- **LS-SSDD-v1.0** - Large-Scale SAR Ship Detection Dataset-v1.0. More information and download: https://github.com/CAESAR-Radi/SAR-Ship-Dataset

2.9 Conclusion

After a brief presentation of the radar systems used to acquire the data, we described the basic principles to understand the backscattering from the sea and factors influencing radar backscatter. Then, we summarized the physical bases of radar imagery before presenting the principle of SAR image formation. Particular interests were given to explaining the signal processing methods used to achieve increasingly small resolutions, namely pulse aperture synthesis. We lastly presented the different sources of SAR imagery data.

Chapter 3

Target Statistical Detection Theory in Pulsed Radar

Summary

In this chapter, we first recall the statistical models of the radar clutter under different sea conditions and grazing angles of radar beams used in radar detection. Next, we recall the statistical models of targets employed in radar detection. Then, we provide a relatively compact revision of most of the used GoF (Goodness of Fit) statistical methods to describe how well the model fits the radar clutter. Finally, we introduce the fundamental principles of adaptive CFAR detection and the adaptativity of the detection threshold.

3.1 Introduction

When a radar signal is transmitted and reflected back from a scene, it can generate a complex image that contains both the targets of interest, such as ships, and various types of background clutter, such as waves, shoreline, and other non-target objects. The process of ship detection involves identifying the target ships within this complex radar image. This is typically accomplished using a variety of image processing techniques, which can help to distinguish the targets from the background clutter.

Due to ship scattering, the ship signature usually appears as a brighter spot than the background, i.e., direct reflection from regions perpendicular to the radar beam, corner reflections, and multiple reflections from the ship and sea surface [5]. Ships' wakes can also be seen in the data when photographed by fine spatial-resolution SARs and under appropriate weather-marine circumstances [39]. For ship detection in maritime applications, accurate statistical analysis of sea clutter is a necessary procedure. Statistical analysis of sea clutter involves analyzing the statistical properties of the radar echoes received from the sea surface to distinguish between actual ship targets and sea clutter. This can be done by characterizing various statistical properties of the radar echoes, including the amplitude distribution, the spatial correlation, and the temporal variability. The goal of statistical analysis is to develop models of sea clutter that can be used to reduce its impact on ship detection. A set of distributions can be grouped into a system in order to model a large number of SAR images [40]. Therefore, we need a method to determine the appropriate distribution of each class or mode in a SAR image (histogram).

The CFAR detection technique is an adaptive detection approach that may determine the detection threshold based on the statistical properties of the clutter [18]. As a result, many academics concentrate on identifying appropriate background modeling distributions. As SAR instrument spatial resolution increases, the associated decrease in scatterers per resolution cell increases the appreciability of backscattering responses from distinct ground features, resulting in SAR images with complex land/sea topologies exhibiting even more heavy-tailed and/or bimodal histograms [41]. Leptokurtic distributions such as the Weibull, lognormal, and K-distributions are common in CFAR methods. Recent research has focused on the mixing of distributions [42, 24, 25].

In addition to various statistical models proposed, recent research in radar detection has also explored variations on the CFAR thresholding function itself. The earliest CFAR detectors used in radar detection include CA-CFAR (Cell Averaging-CFAR) [43], GO-CFAR (Greatest of-CFAR) [44], SO-CFAR (Smallest of-CFAR) [45], and OS-CFAR (Ordered Statistic-CFAR) [46]. Among these, the CA-CFAR detector proposed by the Lincoln Laboratory is the most commonly used, but it performs poorly in heterogeneous environments. The GO-CFAR detector works well in clutter edge situations, but not in homogeneous environments. The SO-CFAR detector performs better in multiple target situations, but produces more false alarms in clutter edge or two-sided outlier situations than CA-CFAR. The OS-CFAR detector, which is based on a sorting algorithm, performs better in multiple target situations but worse than the CA-CFAR detector in a homogeneous environment. More recent methods include the TS-CFAR (Truncated Statistics-CFAR) detector [47] and more complex architectures such as the excision-switching-CFAR detector [48].

Overall, the CFAR technique is a powerful tool for ship detection in cluttered radar scenes, and can significantly enhance ship target detection performance by setting a constant FAR. By adaptively adjusting the threshold based on the local environment, CFAR techniques can reduce the impact of clutter and improve the probability of detecting targets of interest.

3.2 Clutter Statistical Models

Radar detection is rarely performed in environments composed of thermal noise only. We generally distinguish two types of clutter. The surface clutter, such as land, sea, etc. and the volume clutter, such as precipitation, insects, rain, etc. [26].

These two types of clutter are such that the SCR (Signal to Clutter Ratio) is very large compared to the SNR. The presence of interference induces a SIR (Signal to interference Ratio) much larger than the SNR. The modeling of the clutter depends on the radar application in question. Indeed, in low resolution radars, the pulse width is greater than 0.5 μs. Moreover, if the detection is done at grazing angles greater than 5 degrees, the surface clutter can be modeled by a Gaussian distribution of zero mean and constant variance (uniform clutter). On the other hand, in some environments, the use of a high resolution radar is unquestionable (pulse width less than 0.5μs). For this case, the experimental data corresponding to this type of clutter have shown that they follow a distribution with a longer tail than that of the Gaussian. Consequently, to detect targets in this type of clutter, it is necessary to model

Table 3.1: Examples of Gaussian and non-Gaussian environments.

Radar type	Pulse width τ (μs)	Land or Sea	Frequency band	Incidence angle (degrees)	Clutter modeling
Low resolution	2	Rocky Mountains	S	≥ 5 < 5	Gaussian Weibull
Low resolution	3	Forested hills	L	0.5°	Lognormal and Weibull
High resolution	0.17	Forest	X	0.7°	Lognormal and Weibull
High resolution	0.17	Cultivated land	X	$0.7° - 5.0°$	Lognormal, Weibull and K
High resolution	0.2	Sea: State 1	X	4.7°	Lognormal, Weibull and K
High resolution	0.1	Sea: State 2	K_V	$1.0° - 30°$	Lognormal, Weibull and K

the environment by non-Gaussian distributions [28]. In the radar literature, the statistical models that can compensate for the absence of a Gaussian clutter are the Weibull, lognormal and K distributions. To this end, Table 3.1 summarizes some cases of non-Gaussian clutter. Note that state 1 and state 2 designate, respectively, light air (ripples without crests) and light breeze (small wavelets. Crests of glassy appearance, not breaking) [26].

Statistical modeling is of great value in SAR imaging applications. Firstly, it leads to an in-depth comprehension of terrain scattering mechanisms. Secondly, it can guide the research of speckle suppression [49], edge detection [50], segmentation [51], classification [52], target detection and recognition [53] for SAR images, etc.

Statistical modeling of SAR data has been a popular research area since the 1970s, when the first SAR image was obtained in the United States. The analysis of real SAR data encouraged the advancement of statistical modeling techniques for which researchers have proposed different statistical models. Among these, the product model-based statistical family has proven to be the most effective. These models can be divided into two main categories; namely, parametric and nonparametric models [54].

3.2.1 Nonparametric models

Nonparametric models are a class of statistical models that do not make assumptions about the underlying probability distribution of the data. Instead, they estimate the distribution directly from the data based on the nonparametric method. Nonparametric models are often used when the distribution is unknown, complex, or not easily described by a known distribution. One common nonparametric model is KDE (Kernel Density Estimation), which estimates the PDF of the data based on a set of kernel functions. The kernel functions are centered on each data point and are used to weight the contribution of nearby data points to the density estimate. The resulting density estimate is a smoothed representation of the underlying probability distribution of the data. Other typical methods include the Parzen window technique [54] the ANN (artificial neural networks) method [55], the SVM (Support Vector Machine) method [56], etc. Nonparametric modeling offers excellent estimation accuracy, but it often requires a large sample data set, complicated computations, and is time-consuming. As a result, it is seldom employed in any applications, with the exception of few studies focusing on the problem of ship target recognition in SAR image with plain sea backgrounds [54].

3.2.2 Parametric models

Parametric models are a class of statistical models that make assumptions about the underlying probability distribution of the data. The models have a finite number of parameters, such as the mean and variance of a Gaussian distribution, that are estimated from the data. The parameters of the normal distribution can then be estimated from the data using methods, such as the MLE or Bayesian inference. Once the parameters have been estimated, the model can be used to make predictions or draw inferences about the data.

Parametric models are often used when the underlying distribution of the data can be described by a known family of distributions. In general, the product model has been widely accepted to be an appropriate statistical model for the sea clutter due to its flexibility [8]. With the analysis of data from different sensors and the scattering mechanism of different kinds of terrain, many concrete SAR statistical distributions for different cases have been proposed. In the following subsection we will describe several statistical models that have been suggested to model radar clutter.

Rayleigh distribution: The Rayleigh distribution is widely used to represent the amplitude distribution of low resolution sea clutter. A clutter return X is said to have a log-normal distribution if its PDF is given by [57]

$$f_X(x) = \frac{2x}{b^2} \exp\left(-\frac{x^2}{b^2}\right) \tag{3.1}$$

where b is the scale parameter of the distribution.

Log-normal Distribution: The Log-normal distribution is well-suited for modeling radar returns that exhibit long-tailed behavior. A clutter return X is said to have a log-normal distribution if its PDF is given by [58]

$$f_X(x) = \frac{1}{\sqrt{2\pi}\sigma x} exp\left(-\frac{(\ln(x)-\mu)^2}{2\sigma^2}\right) \tag{3.2}$$

where $\mu \in \mathcal{R}$ and $\sigma \in \mathcal{R}_{>0}$ are location and scale parameters, respectively.

Weibull distribution: The Weibull distribution has been found to provide a good fit to both sea and land clutter [Dong, 2004]. The PDF of the Weibull distribution on a linear scale is given [58]

$$f_X(x) = \frac{C}{B}\left(\frac{x}{B}\right)^{C-1} \exp\left[-\left(\frac{x}{B}\right)^{C}\right]; x \geq 0, B > 0, C > 0 \tag{3.3}$$

where B and C are the scale and shape parameters, respectively.

K-Distribution: Many researchers have reported that both sea clutter and land clutter obey the K-distribution [Jao, 1984, Watts, 1985 and 1987, Oliver, 1993]. The PDF of the K-distribution is given by [58]

$$f_X(x) = \frac{4}{b\Gamma(\nu)}\left(\frac{x}{b}\right)^{\nu} K_{\nu-1}\left(\frac{2}{b}x\right) \tag{3.4}$$

where $\Gamma(\cdot)$ is the gamma function, $K_\nu(\cdot)$ the modified Bessel function, b the scale parameter and ν the shape parameter.

Generalized Rayleigh distribution: A random variable X is said to have a Generalized Rayleigh distribution if its density function is given by [25]

$$f_X(x;\beta,\gamma) = 2\beta\gamma^2 x e^{-(\gamma x)^2}\left(1-e^{-(\gamma x)^2}\right)^{\beta-1}; x > 0, \beta, \gamma > 0 \tag{3.5}$$

where β and γ are the shape and scale parameters, respectively. Note that Eq. (3.5) is also known as the two-parameter Burr Type X distribution.

Parametric models have several advantages over nonparametric models. They can be more efficient in using data to estimate the model parameters and can make strong assumptions about the underlying distribution, leading to more accurate and interpretable results.

However, parametric models can be limited in their flexibility and may not be appropriate for modeling complex or unknown distributions. Instead, some researchers resort to Mixture models [42]. Mixture models can be useful for modeling SAR images, as they can capture the complex statistical properties of the data. SAR images often contain a mixture of different types of scatterers, each type of which can exhibit different statistical properties. A mixture model can be used to model the distribution of the radar returns from each type of scatterer separately and then combine these distributions to model the overall distribution of the data. In this thesis, we develop an estimation algorithm addressing the problem of parametric PDF estimation for modeling the complex SAR clutter by adopting two novel mixtures, namely, the Weibull Log-normal mixture model and the Generalized Rayleigh mixture model. The two new mixtures show a promising results as details in the conference papers [24, 25].

Weibull Log-normal mixture model: The WLMM (Weibull Log-normal Mixture Model) has its PDF as [24]

$$f_X(x) = f_{\mathrm{wbl}}(x) + (1-)f_{\mathrm{lgn}}(x) \tag{3.6}$$

where $f_{wbl}(x)$ and $f_{lgn}(x)$ are, respectively, the PDF of the Weibull Eq.(3.3) and the log-normal Eq.(3.2) and a mixture weight that is a real number between 0 and 1.

Generalized Rayleigh mixture model: The GRMM (Generalized Rayleigh Mixture Model) considers that the SAR's RVs (Random Variables) result from the contributions of K distributions, such as [25]

$$f_{X_i}(x_i \mid \Theta) = \sum_{k=1}^{K} w_k f_{X_i}(x_i \mid \Theta_k) \tag{3.7}$$

where $f_{X_i}(.)$ is the GR distribution given by Eq. (6.2), Θ a vector of the parameters of the GRMM, Θ_k the parameters of the k^{th} GR distribution (β_k, γ_k), and w_k the weighting parameter. To ensure that $p_{X_i}(x_i \mid \Theta)$ is a well-defined probability distribution, the condition $\sum_{k=1}^{K} w_k = 1$ must hold.

The choice between parametric and nonparametric models depends on the specific application and the characteristics of the data. Parametric models may provide more accurate estimates of the underlying distribution if the assumptions of the model are met, but they may be less flexible in fitting complex data. Nonparametric models, on the other hand, may be more appropriate when the underlying distribution is complex or unknown, but may require more data to achieve the same level of accuracy as parametric models. Overall, the choice between parametric and nonparametric models depends on the specific application and the characteristics of the data. Therefore, it is important to carefully evaluate the assumptions and limitations of both types of models before choosing a model for a particular analysis.

3.3 Target statistical models

The target represents the object we want to detect. For a target to be detected, it must satisfy two conditions. It must be above the radar horizon and be able to return a sufficiently strong echo. The strength of a target's return echo depends greatly on its width and height above the radar horizon. However, these factors are not sufficient. Indeed, a small, highly reflective target may well return a greater echo than a larger target with low reflectivity [26]. In statistical decision theory, a target can be characterized by an echo signal whose amplitude or SCR is unknown and non-fluctuating, random and following a Rayleigh law, or random and following a one-dominant-plus Rayleigh law. Generally, most radar targets are fluctuating because their dimensions are larger than the wavelength. However, only spherical targets or reflector wedges, viewed at a constant angle are non-fluctuating (constant RCS). Fig 3.1 shows how the fluctuations in the RCS of an aircraft flying toward the radar manifest themselves. On the other hand, note that for the same value of P_D, non-fluctuating targets require a smaller SNR than that required by fluctuating targets. Furthermore, for fluctuating targets, the SNR is a function of the type of fluctuation. Swerling observed and classified targets according to their SNR fluctuations into five statistical patterns called Swerling 0 or V (non-fluctuating pattern), Swerling I, Swerling II, Swerling III and Swerling IV (fluctuating patterns) [59, 60].

3.3.1 Swerling models

Swerling I or SWI model: This is a scan-to-scan model, characterized by a slowly fluctuating target whose envelope amplitude q (Should unify the notation) of the reflected signal

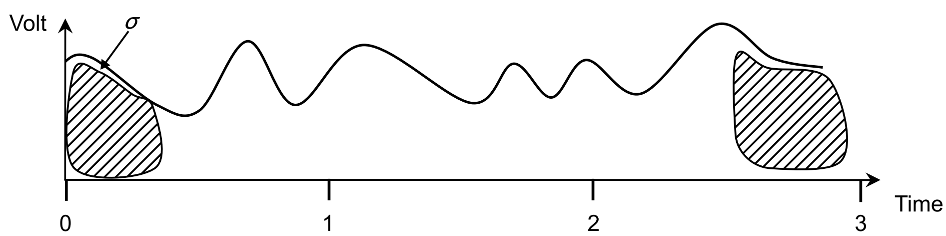

Figure 3.1: Echo signal from an aircraft flying towards the radar.

follows a Rayleigh law, such that its PDF is described by [26]

$$f(q) = \frac{q}{\sigma^2_{\text{target}}} \exp\left(-\frac{q^2}{2\sigma^2_{\text{target}}}\right), \quad q \geq 0 \tag{3.8}$$

The parameter σ^2_{target}, represents the variance of the target, which is proportional to its SCR.

Swerling II or SWII model: This is a pulse-to-pulse model, characterized by a rapidly fluctuating target whose envelope amplitude q of the reflected signal follows a Rayleigh law such that its PDF is described by Eq. (3.8).

In practice, the SW I and SW II types are similar to independent reflective elements, none of which is predominant. Many targets fall into this category, including aircraft.

Swerling III or SW III model: This is a scan-to-scan model, characterized by a slowly fluctuating target whose envelope amplitude q of the reflected signal follows a modified Rayleigh law (one-dominant-plus Rayleigh), such that its PDF is written by [26]

$$f(q) = \frac{9q^3}{2\sigma^4_{\text{target}}} \exp\left(-\frac{3q^2}{2\sigma^2_{\text{target}}}\right), \quad q \geq 0 \tag{3.9}$$

Swerling IV or SW IV model: This is a pulse-to-pulse model, characterized by a rapidly fluctuating target whose envelope amplitude q of the reflected signal follows a modified Rayleigh law or one-dominant-plus Rayleigh such that its PDF is written by Eq.(3.9).

In practice, the SWIII and SWIV models are similar to a preponderant but non-fluctuating reflective element, associated with many less important and independent elements. Missiles fall into this category of targets.

Correlated chi-square targets: In a more general case than the one given by the four models of fluctuating Swerling targets, we find in the literature so-called chi-square targets with several degrees of freedom. The SW I and SW II models then characterize chi-square targets with two degrees of freedom and the SW III and SW IV models targets with four degrees of freedom. Furthermore, all of these multi-degree-of-freedom targets can be considered in some applications to be partially correlated. Unlike the partial correlation of the clutter whose origin is due to the radar receiver, the partial correlation of the targets is due solely to the nature of the RCS of the target itself. As a special case, we find completely correlated targets (SW I and SW III) and those that are completely decorrelated (SW II and SW IV).

3.4 Goodness of fit testing

Detecting bright targets at sea with CFAR algorithms poses a significant challenge due to the varying degrees of homogeneity on sea surfaces. The primary objective is to achieve high target detection while maintaining the FAR below a predetermined level [61]. To achieve this, it is important to determine whether the statistical model being used to represent the radar returns accurately captures the underlying distribution of the data. If the model does not fit the data well, it may not be effective for detecting targets in the image.

GoF is a statistical technique used to evaluate how well a given probability distribution model fits a particular clutter return. It is commonly used to determine if a particular distribution model is a good fit for a set of observed data. GoF testing involves comparing the distribution of the observed data to the expected distribution of the proposed model. The basic idea of GoF testing is to compare the observed data to the theoretical probability distribution, to determine if the data is consistent with the distribution. The most commonly used method for GoF testing are the following tests.

3.4.1 KS Test

The KS (Kolmogorov-Smirnov) statistic for a given CDF (Cumulative Distribution Function) $F_0(x)$ is given by DN, a measure of the deviation of EDF (Empirical Distribution Function) from $F_0(x)$, as [61]

$$D_N = \sup_x \mid \hat{F}_X(x) - F_0(x) \mid \tag{3.10}$$

where sup S is the supremum or LUB (Least Upper Bound) of the set S, $\hat{F}$ the EDF and N the number of observations.

3.4.2 AD Test

To assess whether the N observations come from a distribution with CDF $F_0(\cdot)$, we can use the AD (Anderson–Darling) test, where [61]

$$A^2 = -N - S \tag{3.11}$$

with

$$S = \sum_{i=1}^{N} \frac{2i-1}{N} \left[\ln F_0(x_{(i)}) + \ln(1 - F_0(x_{(N+1-i)}))\right] \tag{3.12}$$

where the $x_{(i)}$'s are the rank ordered observations.

3.4.3 MSE Test

The MSE (Mean Squared Error) test is a simple method for measuring the deviation between an input histogram and an estimated PDF. The MSE is defined by [62]

$$\text{MSE} = \frac{1}{M}\sum_{i=0}^{M-1}\left(h(i) - h_e(i)\right)^2 \tag{3.13}$$

where M is the maximum of the image intensity values, $h(\cdot)$ the normalized histogram and $h_e(\cdot)$ the suitable PDF.

3.5 Adaptive threshold algorithms

Adaptive threshold algorithms are the most common prescreening algorithms for target detection in radar imagery that address some of the limitations of global thresholding [5]. Unlike global thresholding, which uses a fixed threshold value for the entire image, adaptive thresholding adjusts the threshold value locally, depending on the characteristics of the image in each neighborhood. The basic idea of adaptive thresholding is to divide the image into small regions or blocks and compute the threshold value for each block based on the statistical properties of the pixel intensities in that block. This allows for more accurate separation of targets and clutter in areas with varying illumination, contrast and noise.

The constant P_{FA} is an obvious objective when building adaptive threshold detectors. In this instance, the threshold is selected to ensure a steady percentage of background pixel values go above the threshold. The FAR (number of false alarms per unit area of imaging) should remain constant. If this is done, these detectors are known as CFAR detectors. Working directly with the histogram of the background values and setting the threshold at the proper place in its tail is one way for CFAR detection. However, the required FARs are typically very low, and large background samples with a corresponding computational burden would be required to estimate the threshold accurately. As a result, it is more common to parametrically model the background distribution and utilize the background samples to estimate the model parameters [5].

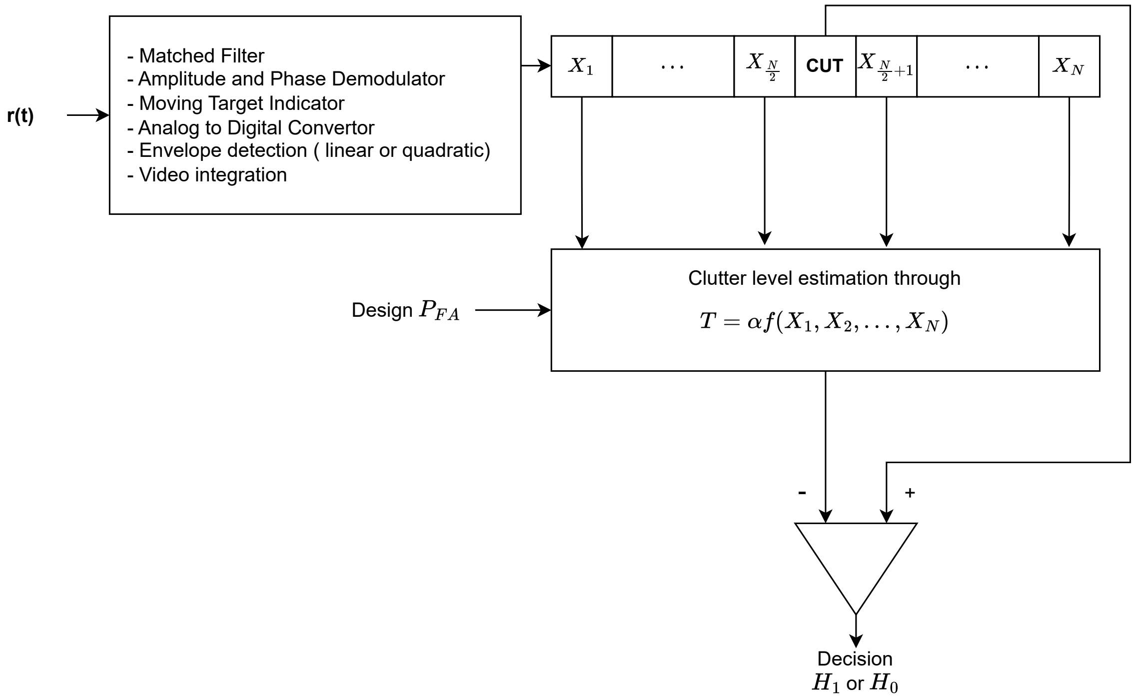

Figure 3.2: General synoptic of a CFAR detector.

3.6 A typical CFAR detector block diagram

Fig 3.2 shows the general block diagram of a CFAR detector. This detector uses an adaptive threshold called $\alpha T(x)$. The multiplicative factor α is calculated to maintain a constant P_{FA}. The mathematical relationship between and $X_1, X_2, \ldots, X_N$ has been the subject of several research works. The Mean Level class of detectors is the most suitable for homogeneous environments. The CA-CFAR detector [43], for which the adaptive threshold is obtained from the averaging of reference samples, is the most popular of the CFAR detectors. However, the presence of inhomogeneities in the clutter significantly degrades the performance of CA-CFAR detector. For this, several research works that take into account changes in the clutter exist in the literature. First, there were the GO-CFAR and SO-CFAR detectors and several variants of detectors based on the fixed-censored and self-censored order statistics [44, 45, 46, 47].

3.7 Likelihood Criteria

To perform automatic target detection, the received signal r(t) is observed in each range-resolved cell (or range) for a time t such that $0 \leq t \leq \tau$. The problem of target detection amounts to considering an optimal decision rule that, based on the observation r(t), can decide on the presence of the signal s(t) that originates from the target or the presence (or absence of s(t)) of a signal n(t) that originates from the environmental noise. Therefore, r(t) is written as

$$r(t) = \begin{cases} s(t) + n(t) & \text{Target} \\ n(t) & \text{Target absent} \end{cases} \tag{3.14}$$

The principles of statistical detection theory are used to determine the structure of the radar receiver to obtain an optimal decision. Therefore, in order to choose an optimal decision rule, it is necessary to evaluate the relative performances of each of them. This leads us to introduce two important statistical parameters, namely the risk and the cost. For an M-Ary hypothesis testing, the risk or average cost is given by [58]

$$\Re = E[C] = \sum_{i=0}^{M-1} \sum_{j=0}^{M-1} P_j C_{ij} Prob(D_i \mid H_j) \tag{3.15}$$

where $Prob(\cdot)$ and $E[\cdot]$ designate, respectively, the probability and the expectation operators and C the cost. Expression (3.15) describes the risk incurred by the receiving system when a decision D_i is made for the hypothesis H_j, with a cost C_{ij} and *a priori* probability $P_j = P(H_j)$. In radar applications, i.e., $M = 2$ hypotheses testing, the criterion that associates optimality with risk is Bayes'. Generally, the costs of correct decisions (detection and null detection) are considered to be zero. In this case, the costs are reduced to C_{01} and C_{10} (non-detection and false alarm). However, when either the costs or the *a priori* probabilities are not available, we recourse to the N-P (Neyman-Pearson) criterion.

3.7.1 Bayes criterion

A decision rule is called Bayes' if it describes a radar receiver with a minimum average cost. It can be shown that minimizing the average cost leads to the following likelihood test [58].

$$\Lambda(x) \underset{H_0}{\overset{H_1}{\gtrless}} \eta \tag{3.16}$$

where

$$\Lambda(x) = \frac{f_{X|H_1}(x \mid H_1)}{f_{X|H_0}(x \mid H_0)} \tag{3.17}$$

and

$$\eta = \frac{P_0\left(C_{10} - C_{00}\right)}{P_1\left(C_{01} - C_{11}\right)} \tag{3.18}$$

are the likelihood ratio and the detection threshold, respectively. where $f_{X|H_1}(x \mid H_1)$ and $f_{X|H_0}(x \mid H_0)$ are the PDFs of the observation X corresponding to each hypothesis H_1 and H_0, respectively.

Since, in general, the a *priori* probabilities and costs are not known, we cannot obtain η from Eq. (3.18). However, the statistical characteristics of s(t) and n(t) allow us to do so [63].

3.7.2 N-P criterion

The N-P (Neyman-Pearson) criterion consists in maximizing the P_D or minimizing the P_M (Probability of Miss), knowing that the P_{FA}, is maintained fixed at a constant value α. For this purpose, we construct the objective function [58]

$$J(\lambda) = P_M + \lambda(P_{FA} - \alpha) \tag{3.19}$$

where λ is the Lagrange multiplier. The minimization of $J(\lambda)$ leads to the following N-P rule

$$\Lambda(x) = \frac{f_{X|H_1}(x \mid H_1)}{f_{X|H_0}(x \mid H_0)} \begin{array}{c} H_1 \\ > \\ < \\ H_0 \end{array} \lambda \tag{3.20}$$

λ is the detection threshold obtained from the constraint $P_{FA} = \alpha$.

The Bayes and N-P detection criteria thus lead to the same decision rules. They are given, respectively, by Eqs. (3.16) and (3.20). Indeed, both criteria reduce to the maximization of the P_D for a particular value of the P_{FA}. However, the N-P criterion is easier to use because it only uses the variance of the environment (noise and clutter).

According to Eq. (3.19), the X_{CUT} is compared to the adaptive threshold T according to the following statistical test

$$X_{\text{CUT}} \begin{array}{c} H_1 \\ > \\ < \\ H_0 \end{array} T \tag{3.21}$$

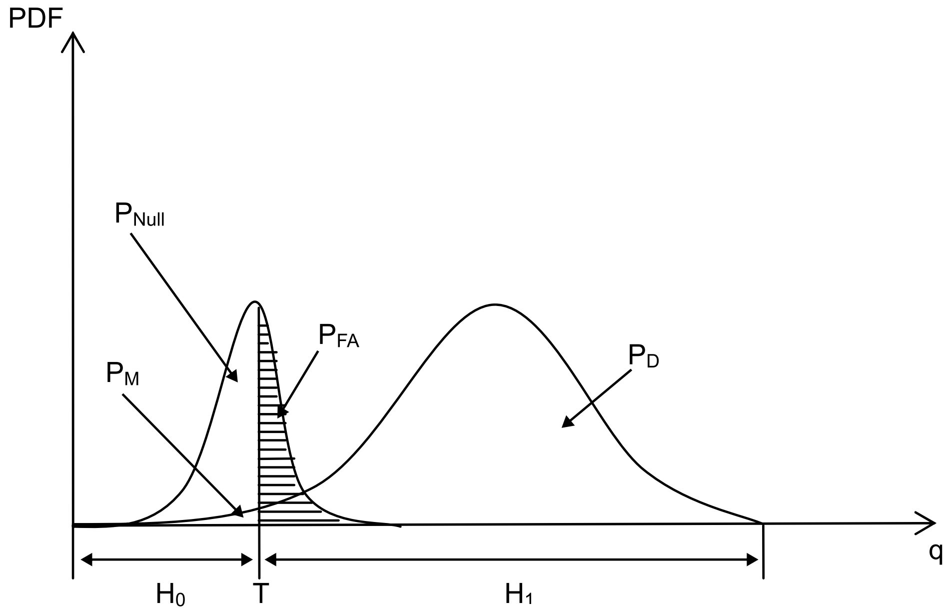

Figure 3.3: Decision-making regions.

where λ is a multiplicative factor and T the clutter level. In this adaptive detection context, the P_D and P_{FA} can be written, respectively, as [26]

$$P_D = Prob\,(X_{\mathrm{CUT}} \geq T \mid H_1) \tag{3.22}$$

and

$$P_{FA} = Prob\,(X_{\mathrm{CUT}} \geq T \mid H_0) \tag{3.23}$$

Using the PDF $f_T(T)$ of the statistics T, we obtain

$$P_D = \int_0^{\infty} f_T(t) \int_T^{\infty} f_{X_{\mathrm{CUT}}|H_1}\,(x_{\mathrm{CUT}} \mid H_1)\, dx_{\mathrm{CUT}} dt \tag{3.24}$$

and

$$P_{FA} = \int_0^{\infty} f_T(t) \int_T^{\infty} f_{X_{\mathrm{CUT}}|H_0}\,(x_{\mathrm{CUT}} \mid H_0)\, dx_{\mathrm{CUT}} dt \tag{3.25}$$

Fig 3.3 shows, for a Gaussian target immersed in a Gaussian clutter, the decision regions with respect to the detection threshold T. Sliding T along the x-axis allows for different scenarios of P_D and P_{FA}. P_{Null} is the Probability of Null detection and P_M the probability of non-detection.

3.8 Conclusion

The CFAR adaptive detection is the essential innovation in the modern radar detection system. In order to avoid confusion, the clutter and target models must be rigorously listed.

The choice of the performance criterion is decisive for the calculation of the detection and false alarm probabilities. To this effect, we first recalled the statistical models of clutter and targets used in radar detection. Then, we presented most of the used GoF statistical methods to describe how well the model fits the radar clutter. Finally, we introduced the principles of adaptive CFAR detection.

Chapter 4

Maximum Likelihood QM-CFAR Detection in Weibull Clutter

Summary

This chapter constitutes our first contribution to CFAR target detection. A recent survey has revealed that radar researchers still encounter difficulties to develop detectors that cope with non-Gaussian backgrounds. On another note, in real-world applications, many modeling research papers show a high agreement between radar sea clutter data and the Weibull distribution. This being, we introduce the QM-CFAR detector for a Weibull background. Specifically, assuming a non-stationary Weibull clutter with the presence or not of interfering targets, the QM and the MLE are concomitantly used to allow the proposed detector to perform robustly in multiple target situations with a *priori* unknown Weibull parameters. MC simulations show that, compared to recent existing CFAR algorithms, the QM-CFAR detector provides robust and accurate estimates of the Weibull distribution parameters and achieves less degradation of the P_D in multiple target situations.

4.1 Introduction

As it is well-known, automatic signal detection is the central task of a modern radar system. Behind this very attractive and challenging field are the non-stationary clutter and environments heterogeneities. For clutter scenarios such as multiple target situations, the basic goal is mainly the derivation of the optimum receiver to automatically detect a target with *a priori* unknown information about the environment. Solutions to this classical problem are very efficient in diverse fields such as civilian applications, military tasks, and sea monitoring [64, 58].

The mean level detectors or CA-CFAR family has long been used for Gaussian environments [43, 44, 45]. The OS-CFAR detector was intended to overcome the problem of multiple targets situations arising in the CA-CFAR family [46]. However, in many practical situations, the Gaussian density in high-resolution radar is shown to be a poor fit to the clutter envelope. In such cases, a family of biparametric distributions is required to achieve a suitable fit to the real-world data.

In [65, 66, 67, 68, 69, 70, 71], some detectors for non-Gaussian environments are considered. Goldstein [65] introduced the log-t-CFAR for log-normal and Weibull environments. In a homogeneous environment, this detector is optimal for a log-normal clutter and performs well for a Weibull clutter. Afterward, Weber and Haykin [66] introduced a nonparametric technique, namely the WH-CFAR (Weber-Haykin-CFAR) detector, for which the threshold is based on pairs of the OS samples of the Weibull random sequence. This method is more robust to interferences but still yields an excessive detection loss. Later, based on the MLEs of the Weibull parameters Ravid and Levanon [67] introduced the ML-CFAR detector. In a homogeneous environment, the ML-CFAR detector exhibits a small $\mathrm{CFAR}_{\mathrm{Loss}}$, yielding considerable detection performances with respect to the previous detectors. They also introduced the CML-CFAR (Censored ML-CFAR) in multiple target situations. Recently, Almeida *et al.* [68] found a closed form expression of the P_{D} (Detection Probability) for a square-law detector of an exponential target in a Weibull distributed clutter. Based on the zlog(z) estimators of the Weibull parameters, Gouri *et al.* [69] proposed the zlog(z)-CFAR detector. This detector exhibits almost similar detection performances as the ML-CFAR detector, but with a lower time-consuming procedure. Weinberg *et al.* [70] developed three robust detectors that achieve the CFAR property in Weibull clutter disturbances, namely the

GMOS-CFAR (Geometric Mean Order Statistics-CFAR), the TMOS-CFAR (Trimmed Mean Order Statistics-CFAR) and the IE-CFAR (Inclusion/Exclusion-CFAR) detectors. Based on the WL (Weighted Likelihood) estimator for a Weibull clutter with known shape parameter, Zhang *et al.* [71] developed the WL-CFAR detector which aims to overcome problems that weaken the performances of the detector in heterogeneous environments, i.e., multiple target and clutter power transition scenarios.

A shown in Table. 4.1, except the proposed QM-CFAR detector whose optimality, in both Weibull homogeneous clutter and multiple target situations is to be assessed in this paper, all other cited detectors work effectively in a homogeneous clutter but degrade significantly in multiple target situations. To this effect, we propose and analyze the QM-CFAR detector, whose detection threshold is estimated through the QM theory. This new detector relies upon a fixed number of quantiles (ordered statistics) drawn from the reference cells, allowing censoring of the upper end of the reference window. In doing this, it simply uses selected quantile information to estimate the distribution parameters using QME (QM Estimation).

4.2 Parameter Estimation and CFAR Detection

The received signal is first processed by a LED (Linear Envelope Detector) matched filter. The resulting samples are then stored in a tapped delay line of length $N+1$, corresponding to the N reference cells surrounding the CUT. We assume that the N random samples $X = (X_1, X_2, ..., X_N)^{Tr}$, where Tr denotes the transpose operator, are IID (Independent and Identically Distributed), drawn from the same Weibull distributed RV (Random Variable) X, whose PDF is given by [69]

$$f_X(x) = \frac{C}{B}\left(\frac{x}{B}\right)^{C-1} \exp\left[-\left(\frac{x}{B}\right)^{C}\right]; x \geq 0, B > 0, C > 0 \tag{4.1}$$

where B and C are the scale and shape parameters, respectively. Its CDF is given by

$$F_X(x) = 1 - \exp\left[-\left(\frac{x}{B}\right)^{C}\right]; x \geq 0, B > 0, C > 0 \tag{4.2}$$

In real-world applications, many modeling research papers show a high agreement between the radar sea clutter data and the Weibull distribution [72]. Note that for $C = 1$ and 2, the Weibull PDF reduces to the exponential and the Rayleigh PDFs, respectively. $C < 1$,

Table 4.1: Advantages and Disadvantages of the detectors subjected to the comparative study in a Weibull clutter
NIT (Number of Interfering Targets).

Detector	Advantages and Disadvantages
logt-CFAR [65]	Performs fairly in a homogeneous clutter / Performance degrades in multiple target situations when *ICR* increases.
WH-CFAR [66]	Performs well in multiple target situations when NIT is *a priori* known / $\text{CFAR}_{\text{Loss}}$ is somewhat high in a homogeneous clutter.
TMOS-CFAR [70]	Performs well in presence of one interfering target / $\text{CFAR}_{\text{Loss}}$ is somewhat high in a homogeneous clutter.
IE-CFAR [70]	Optimal in a homogeneous clutter / Performance degrades in multiple target situations when either *ICR* or NIT increases.
zlog(z)-CFAR [69]	Optimal in a homogeneous clutter / Performance degrades drastically in multiple target situations when either *ICR* or NIT increases.
WL-CFAR [71]	Optimal in a homogeneous clutter / Performance degrades in multiple target situations.
QM-CFAR	$\text{CFAR}_{\text{Loss}}$ is optimal in both homogeneous clutter and multiple target situations / NIT should be *a priori* known.

implies a longer tailed PDF, i.e., spiky clutter. Then the $X_i s, i = 1, 2, ..., N$, are ranked in an ascending order to get the quantile information for each sample.

4.2.1 Quantile Matching Theory

As stated earlier, CFAR detectors for a Weibull background have been proposed in [67, 69]. Their respective adaptive thresholds are based on the estimation of the shape and scale parameters. This is accomplished through the use of the ML or the zlog(z) estimator. In addition, it has been shown that the $\text{CFAR}_{\text{Loss}}$ is proportional to the variance of the estimated parameters [67]. To lower the variance, and therefore, the $\text{CFAR}_{\text{Loss}}$, the QM-CFAR detector is developed here. Note that Nirwan and Bertschinger [73] have proposed the BQME (Bayesian QME), while, here, we develop the estimates of the Weibull parameters through the MLE. The QME has shown to be a useful technique that allows one to infer the underlying distribution from only the quantile information.

Let us select M quantiles $\boldsymbol{q} = (q_1, q_2, \ldots, q_M)^{Tr}$, $\boldsymbol{q} \in [0,1]^M$ and their corresponding rank ordered empirical values $X = (X_{(1)}, X_{(2)}, ..., X_{(M)})^{Tr}$. Note that, to simplify the analysis, we adopt the same notation of RV (Random Variable) X as for the underlying received sequence. Here, as we have access to all N cells, the selected number of quantiles, $M = N - R$, where $R = 0, 1, 2, \ldots$ is the NIT. Thus, in order to estimate the parameter $\theta = (\theta_1, \theta_2, ..., \theta_p)^{Tr}$, $\theta \in \Theta$, p denotes the number of the unknown parameters, from the selected quantiles $X \in R^M$ and their corresponding order $\boldsymbol{k} = (k_1, k_2, ..., k_M)^{Tr}$, $\boldsymbol{k} \in N^M$, we need to evaluate the conditional joint PDF $p_{X|\boldsymbol{k},N}(x \mid \boldsymbol{k}, N)$ of the order statistics, which is shown to be, for any distribution [73]

$$\begin{aligned} p_X\left(x \mid \boldsymbol{k}, N\right) &= \eta F_X\left(x_{(1)}\right)^{k_1-1}\left(1 - F_X\left(x_{(M)}\right)\right)^{N-k_M} \\ &\times \prod_{m=2}^{M}\left(F_X\left(x_{(m)}\right) - F_X\left(x_{(m-1)}\right)\right)^{k_m-k_{m-1}-1} \\ &\times \prod_{m=1}^{M} f_X(x_{(m)}) \end{aligned} \tag{4.3}$$

where η is a normalization constant given by

$$\eta = \frac{N!}{(k_1-1)!\,(N-k_m)!\,\prod_{m=2}^{M}(k_m-k_{m-1}-1)!} \tag{4.4}$$

Next, instead of relying on the order k, we rely on the quantile information $q \in [0,1]^M$ and $X \in R^M$. Note that, generally, the order k may not be such as $k_m - k_{m-1} = 1$. Now, we just need to replace k_m in Eq. 4.3 by the product of the quantile q_m and N, i.e., $k_m = q_m N$. Taking these definitions into account, the conditional joint PDF of the order statistics becomes

$$\begin{aligned} &P_X\left(x \mid \boldsymbol{q}, \theta, N\right) = \\ &\eta F_\theta\left(x_{(1)}\right)^{q_1N-1}\left(1 - F_\theta\left(x_{(M)}\right)\right)^{N-q_MN} \\ &\times \prod_{m=2}^{M}\left(F_\theta\left(x_{(m)}\right) - F_\theta\left(x_{(m-1)}\right)\right)^{q_mN-q_{m-1}N-1} \\ &\times \prod_{m=1}^{M} f_\theta(x_{(m)}) \end{aligned} \tag{4.5}$$

Note that the conditional joint PDF of Eq. 4.5 is parameterized by θ, which needs to be estimated. The likelihood function is defined as

$$L(\theta) = P_{X|\boldsymbol{q},\Theta,N}(x \mid \boldsymbol{q}, \theta, N) \tag{4.6}$$

In order to maximize the likelihood function of Eq. 4.6, standard techniques of calculus may be used. Here, instead of using the BQME [73], the estimate $\hat{\theta} = (\hat{\theta}_1, \hat{\theta}_2, ..., \hat{\theta}_p)^{Tr}$ that maximizes the likelihood function is computed through the MLE of θ. Because the logarithmic is a monotonically increasing function, maximizing $L(\theta)$ is equivalent to maximizing $lnL(\theta)$. Hence, it can be shown that a necessary but not sufficient condition to obtain the ML estimate $\hat{\theta}$ is to solve the log likelihood equation

$$\frac{\partial \ln L(\theta)}{\partial \theta} = 0 \tag{4.7}$$

As we could not find any closed form expressions of the MLEs of the shape and scale parameters of the Weibull distribution, we had to recourse to the `fminsearch.m` Matlab function.

CFAR property

Recall that CFAR data processing techniques are widely used in radar target detection to control the FAR when the clutter parameters are unknown *a priori*. A CFAR processor dynamically selects the parameters based on an estimator which is specific to the environment under consideration. Then, a detection threshold algorithm is adjusted for each cell so that the P_{FA} remains constant. The QM-CFAR detector is summarized as follows. We first use the rank ordered reference samples $X_{(1)}, X_{(2)}, \ldots, X_{(M)}$ to select the quantile information that shares the same clutter parameters as the CUT and eliminate any outliers within the data. Then, we resort to the QM and the MLE to get the clutter parameters. Finally, we carry out target decision through the following hypothesis test

$$X_{CUT} \underset{H_0}{\overset{H_1}{\gtrless}} T \tag{4.8}$$

where T is the adaptive detection threshold, X_{CUT} the random sample within the CUT, H_1 refers to the presence of a target hypothesis and H_0 to the absence of a target hypothesis. For a Weibull clutter, if the scale B and the shape C parameters were known *a priori*, then a design $\mathrm{P_{FA}}$ would be readily achieved by setting a fixed threshold noted T_{ideal} such that

$$P_{FA} = Pr\left\{X > T_{ideal} \mid H_0\right\} \tag{4.9}$$

where Pr denotes the probability operator. In other words, T is the $(1 - P_{FA})$ quantile of the distribution of X. An ideal CFAR processor would have a threshold $T_{ideal} = F^{-1}(1 - P_{FA})$, where $F^{-1}(\cdot)$ is the ICDF (Inverse CDF). For the Weibull distribution [67],

$$T_{ideal} = B\left(-lnP_{FA}\right)^{\frac{1}{C}} \tag{4.10}$$

Since, in general, the parameters are *a priori* unknown, in order to regulate the actual $\mathrm{P_{FA}}$ of the proposed detector, the threshold T should be written as [67]

$$T = \hat{B}\alpha^{\frac{1}{\hat{C}}} \tag{4.11}$$

where α is the threshold multiplier that maintains CFAR, and $\hat{B}$ and $\hat{C}$ (solutions of Eq. 4.7), are, respectively, the estimates of B and C.

Because of the difficulties that arise in the derivation of an analytic expression of the $\mathrm{P_{FA}}$, proving the CFAR property of a detector remains a challenging task. Instead of the conventional approach, a new research reveals that if the derived detector meets certain criteria, it can be declared CFAR. Specifically, any invariant test with respect to a minimally invariant group is CFAR [71]. To begin the numerical analysis, we resort to MC simulations to study the CFAR property of the QM detector with respect to the scale parameter. As shown in Fig. 4.1a, we first show the curves of the simulated $log_{10}(P_{FA})$ versus the threshold scale factor $\alpha(dB)$ under various scale parameter values ($B = 0.0322, 0.5, 1.5,$ and 2) and a fixed shape parameter value $C = 0.9439$. The results clearly show that there is a complete overlap between all curves regardless of the value of B. As a result, the proposed detector maintains the CFAR property with respect to the scale parameter. To investigate the CFAR property of the proposed detector with respect to shape parameter, Fig. 4.1b shows the curves of the simulated $\mathrm{P_{FA}}$ versus the threshold scale factor $\alpha(dB)$ for different shape parameter values ($C = 0.1, 0.5, 0.9439$ and 3) and a fixed scale parameter ($B = 0.032$). Although the curves show tiny bifurcations, the inferred values of the $\mathrm{P_{FA}}$ are likewise acceptable in real-world applications. As a result, the proposed detector maintains the CFAR property with respect to the shape parameter. Consequently, the QM detector is CFAR irrespective of the values of B and C. Hence, from now on, we may name it as the QM-CFAR detector.

In this chapter, we perform a comparison study of the QM-CFAR detector with the log-t-, WH-, TMOS-, IE-, zlog(z)-, WL-CFAR, and the fixed threshold (ideal) detector. As we already know from the radar literature, the log-t-, WH-, TMOS-, IE-, zlog(z)-, and WL-CFAR detectors have the CFAR property in a Weibull clutter [65, 66, 70, 69, 71], respectively. Hence, here, we only intend to confirm such a property and get the values of the respective threshold multipliers α, for the design $\mathrm{P_{FA}}$. That is, Fig. 4.2. shows the curves of $log_{10}(P_{FA})$

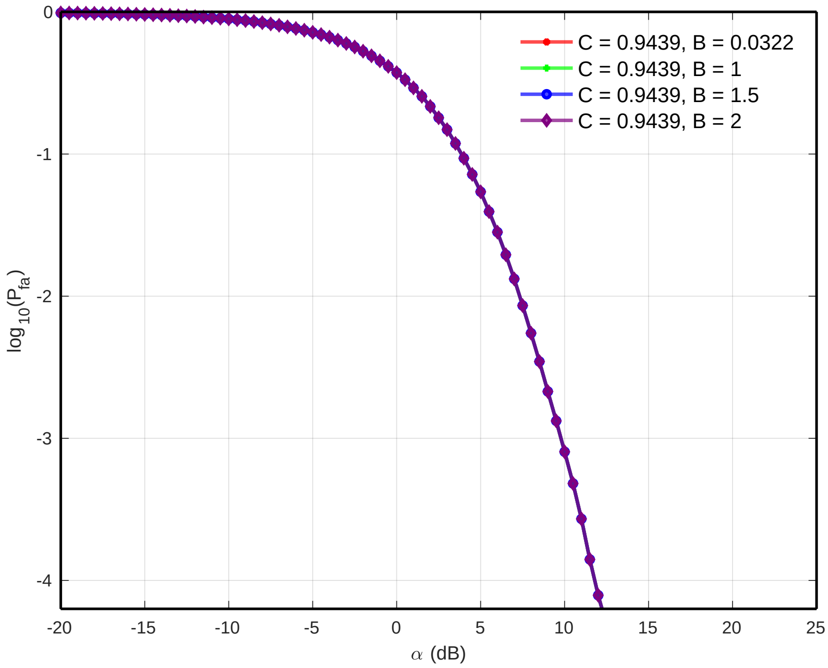

(a)

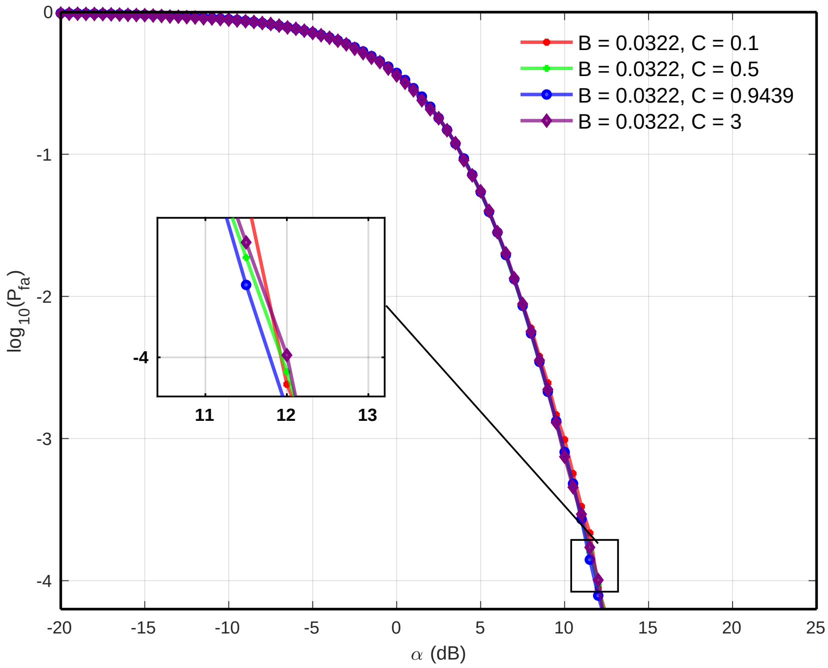

(b)

Figure 4.1: CFAR property of the QM detector with respect to (a) scale parameter; (b) shape parameter.

versus $\alpha(dB)$ for all detectors; for $N = 32, B = 0.0322$ and $C = 0.9432$. Their corresponding threshold multiplier values for $P_{FA} = 10^{-4}$ are $\alpha_{\text{logt-CFAR}} = 4.33dB$, $\alpha_{\text{WH-CFAR}} = 1.07dB$, $\alpha_{\text{TMOS-CFAR}} = 1.71dB$, $\alpha_{\text{IE-CFAR}} = -5.35dB$, $\alpha_{\text{zlog(z)-CFAR}} = 12.12dB$, $\alpha_{\text{WL-CFAR}} = 11.98dB$

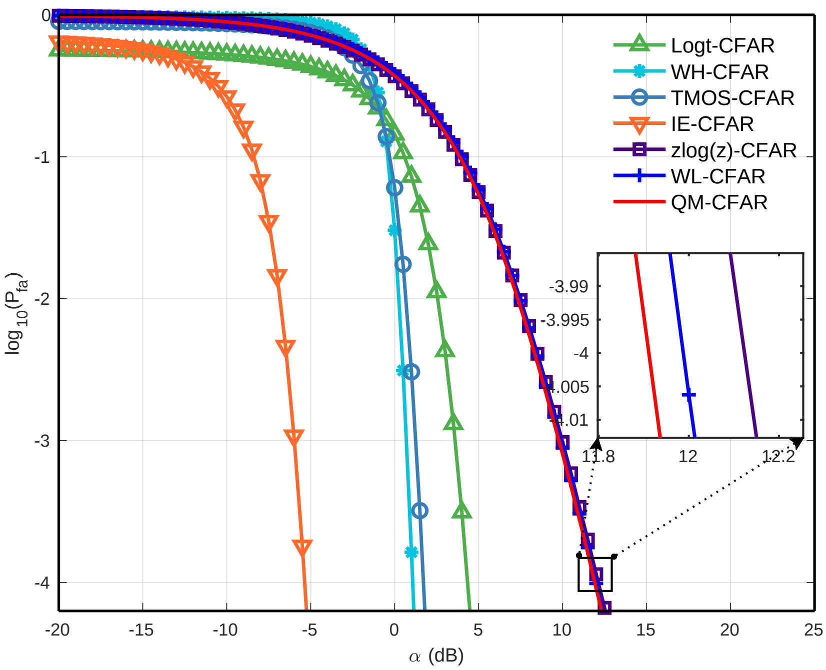

Figure 4.2: CFAR property of the different detectors; for $N = 32, B = 0.0322$ and $C = 0.9439$.

and $\alpha_{\text{QM-CFAR}}= 11.91dB$. Note that, as stated in [70], we have chosen $k = 31$ and $\mathcal{I} = [2, 3, 4, 5]$ for the TMOS-CFAR detector, $\mathcal{I} = [1, 2, 3, ..., 25]$ for the IE-CFAR detector, and $\alpha = 0.05$ measures the desired robustness level of the WL-CFAR detector. In addition, the WL-CFAR detector requires the *a priori* knowledge of the Weibull shape parameter [71]. Here, the Weibull shape parameter is estimated based upon the clutter measurements in the reference cells.

4.3 Analysis of the proposed QM-CFAR Detector

4.3.1 Homogeneous environment

For a homogeneous Weibull environment, we first evaluate the detection performances of the proposed detector versus all detectors cited above. Fig. 4.3. shows the $\mathrm{P_D}$ against the SCR (Signal-to-Clutter Ratio) $\in [0dB\ 60dB]$, for $N = 32, P_{FA} = 10^{-4}$. Throughout all the subsequent simulations, the Weibull shape and scale parameters are set to $B = 0.0322$ and $C = 0.9439$. These clutter parameter estimates have been obtained by their respective MLEs applied to real clutter returns [70, 74]. It is clear, from this figure, that the $\mathrm{P_D}$ curves of

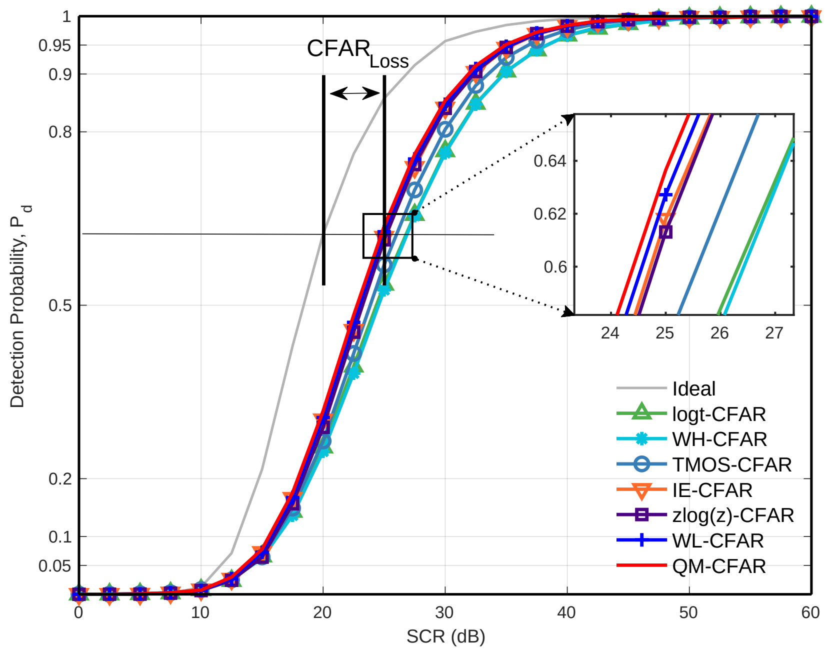

Figure 4.3: Detection probabilities ($\mathrm{P_D}$) against SCR in a homogeneous background of the different detectors; for $N = 32, B = 0.0322, C = 0.9439$, and $P_{FA} = 10^{-4}$.

the WH-CFAR and logt-CFAR detector are the lowest, then comes that of the TMOS-CFAR detector. While, all remaining detectors seem to have the same $\mathrm{P_D}$, the magnifier of Fig. 4.3 shows that the $\mathrm{P_D}$ of the QM-CFAR detector is slightly higher. Furthermore, as shown in the $\mathrm{CFAR_{Loss}}$ of Table 4.2 (row 1), the QM-CFAR detector exhibits the lowest $\mathrm{CFAR_{Loss}}$ value. The $\mathrm{CFAR_{Loss}}$ is the ratio between the SCR required to achieve specified $\mathrm{P_D}$ and $\mathrm{P_{FA}}$, and the SCR of the ideal detector; it is given by [67]

$$\mathrm{CFAR_{Loss}} = \frac{SCR(P_D, P_{FA}, \hat{C}, N)}{SCR_{\mathrm{ideal}}(P_D, P_{FA}, C)} \tag{4.12}$$

As the numerator of Eq. 4.12 is difficult to evaluate, we resort to the graphical method illustrated in Fig. 4.3. Namely, for given $\mathrm{P_{FA}}$ (10^{-4}) and N (32), the $\mathrm{CFAR_{Loss}}$ ($4.78dB$; Table 4.2, row 1) is the difference between the SCR ($24.78dB$) required to achieve a specified $\mathrm{P_D}$ (0.6234), and the SCR ($20dB$) of the ideal detector given by Eq. 4.10.

4.3.2 Multiple target situations

In real-world scenarios, some interfering targets may appear in the reference cells. To this effect, we now investigate the detection performances of the proposed detector in multiple target situations. In this case, the threshold raises and the detection degrades. This is known

Table 4.2: $\text{CFAR}_{\text{Loss}}$ (dB) of the different detectors with respect to the ideal detector in a homogeneous environment and in the presence of interfering targets; for $N = 32, B = 0.0322, C = 0.9439$, $SCR = 20dB$ and $P_{FA} = 10^{-4}$ (Bold numbers designate the lowest values of the $\text{CFAR}_{\text{Loss}}$)

NIT	*ICR*	logt-	WH-	TMOS-	IE-	zlog(z)-	WL-	QM-CFAR
0	$-\infty$	6.81	6.89	6.03	5.11	5.19	4.94	**4.78**
	15dB	8.44	9.44	8.56	7.96	9.54	8.24	**7.34**
1	20dB	9.38	9.91	9.03	9.34	13.98	10.26	**7.74**
	30dB	11.74	10.13	9.26	12.24	28.26	16.56	**7.93**
2		12.02	12.84	19.36	13.50	18.80	14.62	**10.64**
3	20dB	14.46	15.08	23.29	17.38	22.03	18.34	**13.09**
4		16.83	17.52	25.23	21.21	24.27	21.34	**15.74**

Table 4.3: P_{FA} regulation of the different detectors in multiple target situations; for $N = 32, B = 0.0322, C = 0.9439$ and $P_{FA} = 10^{-4}$ (Bold numbers designate the highest values of the ratio)

NIT	Ratio = Simulated P_{FA}/Design $P_{FA} = 10^{-4}$							
	ICR	logt-	WH-	TMOS-	IE-	zlog(z)-	WL-	QM-CFAR
1		0.10	0.23	0.25	0.08	0.02	0.03	**0.26**
2	20dB	$9.00e^{-3}$	0.06	0.01	$2.30e^{-3}$	$5.69e^{-4}$	$6.42e^{-4}$	**0.07**
3		$1.00e^{-3}$	0.02	$1.96e^{-4}$	$5.50e^{-5}$	$1.00e^{-5}$	$1.65e^{-5}$	**0.03**
4		$1.85e^{-5}$	**0.01**	$1.92e^{-5}$	$1.55e^{-5}$	$1.55e^{-8}$	$3.24e^{-8}$	**0.01**

as the capture effect. By means of the same working conditions as before, two examples are shown in Figs. 4.4. and 4.5.

In Fig. 4.4, we consider the presence of one interfering target ($R = 1$) within the reference cells. Figs.4.4a–c show the P_{D} against SCR for values of the ICR (Interference-to-Clutter Ratio) $= 15, 20$ and $30dB$, respectively. Note that the QM-CFAR detector, and to a lesser degree, the TMOS-CFAR detector, are robust in the sense that no excessive $\text{CFAR}_{\text{Loss}}$, Table 4.2 (row 2), occurs when the ICR values increase. All remaining detectors show a significant $\mathrm{CFAR_{loss}}$, particularly for $ICR = 20$ and $30dB$.

To further investigate the robustness of the QM-CFAR in the presence of more than one interfering target, we consider, respectively, the presence of two, three, and four interfering targets within the reference cells ($R = 2, 3$ or 4). For instance, let us assume that the ICR value of all interfering targets is set to $ICR = 20dB$. According to Fig. 4.5, in contrast to

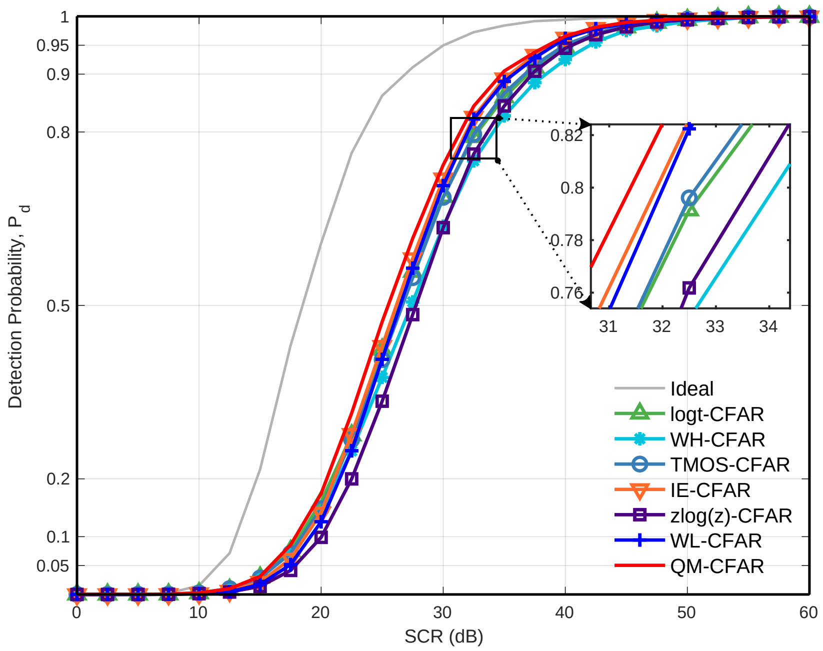

(a)

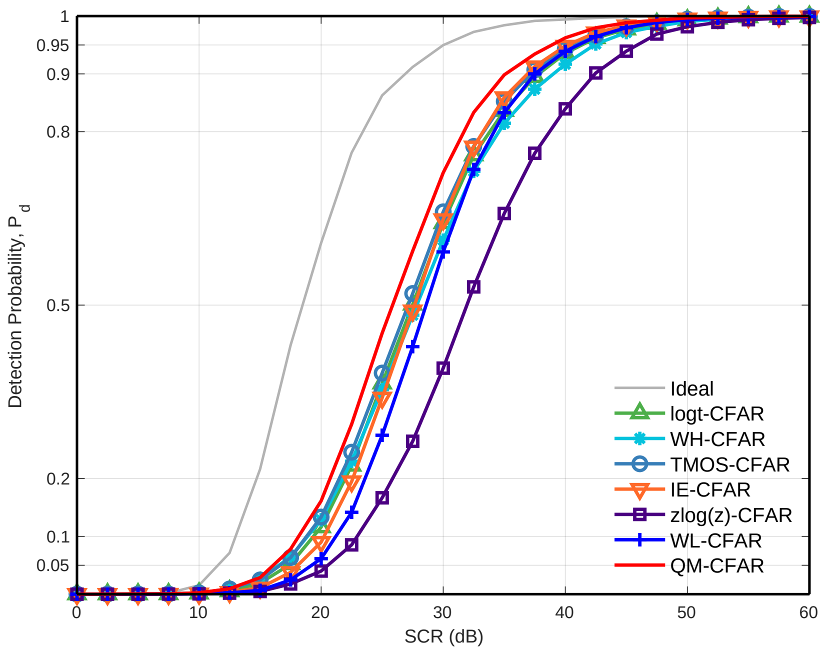

(b)

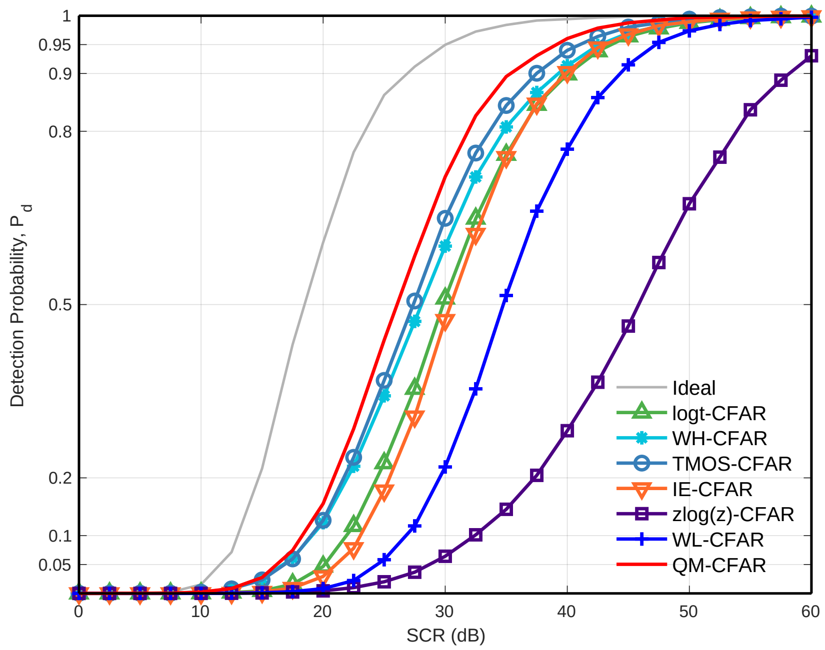

(c)

Figure 4.4: Detection probabilities ($\mathrm{P_D}$) against SCR of the different detectors in multiple target situations; for $N = 32, B = 0.0322, C = 0.9439$, $P_{FA} = 10^{-4}$ and NIT = 1 at (a) $ICR = 15dB$, (b) $ICR = 20dB$ and (c) $ICR = 30dB$.

the TMOS-CFAR whose $\mathrm{CFAR_{loss}}$, Table 4.2 (row 3), seems to degrade drastically in the presence of more than one interfering target, the QM-CFAR detector remains ahead of all detectors.

Referring to Fig. 4.4a and Figs. 4.5a–c, Table 4.3 shows the regulation of the $\mathrm{P_{FA}}$ for the multiple target situations. Although the values of the ratio of the simulated $\mathrm{P_{FA}}$ to the design $P_{FA} = 10^{-4}$ are relatively low, the ones corresponding to the QM-CFAR and WH-CFAR detectors are the highest.

Notwithstanding the fact that we are performing fixed-point censoring of the upper end of the reference cells, there could be real-world situations in which the NIT is either under estimated or over estimated. Figs. 4.6a shows the effect of censoring 2 interfering targets rather than 3 (under censoring situation) on the $\mathrm{P_D}$ of all detectors. Due to the MLE's sensitivity to interfering targets, which has a major effect on the distribution parameters, the $\mathrm{P_D}$ of the QM-CFAR detector exhibits a significant degradation when compared to that of Fig. 4.5b. Alternatively, Fig. 4.6b shows the effect of censoring 4 interfering targets rather than 3 (over censoring situation) on the $\mathrm{P_D}$ of all detectors. Here, the $\mathrm{P_D}$ of the QM-CFAR detector shows a better detection performance than that of Fig. 4.5b. This gain can be explained by the spiky nature of the clutter, for which a clutter return could be assimilated to an interfering target and therefore effectively censored. In consequence, the detection performance of the QM-CFAR becomes suboptimal whenever it is confronted to under censoring situations. To circumvent such limitation, automatic censoring remains the best suited solution.

As a final point, rather than as it is shown in Figs. 4.4 and 4.5, where the robustness of all detectors is assessed through their detection curves, another way would be to resort to their detection thresholds. For the same working conditions as before, Fig. 4.7 shows the detection thresholds of all detectors for a Weibull clutter return, to which 6 Rayleigh targets have been injected in the 80^{th}, 100^{th}, 120^{th}, 140^{th}, 160^{th} and 180^{th} range cells at $SCR = 20dB$. It can be easily seen that the detection threshold of the QM-CFAR detector progresses closely to that of the ideal detector, while the other detectors show exorbitant sawtooth profiles which impact negatively on their detection performances.

4.4 Experimental Results with a Real SAR Image

To validate the advantages of the suggested QM-CFAR for ship detection in SAR images, a dataset of stripMap TerraSAR-X images is used in this study. We consider a SRW size of 33×33. The pixel in the center of the SRW is regarded as the CUT. The size of the guard window is 7×7 pixels so that the CUT is placed at its center. These choices provide 1040

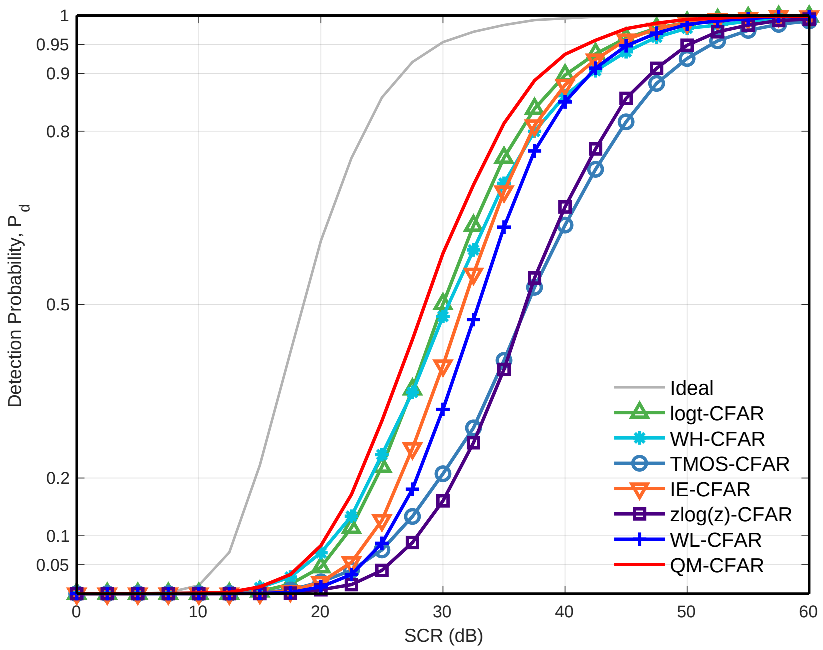

(a)

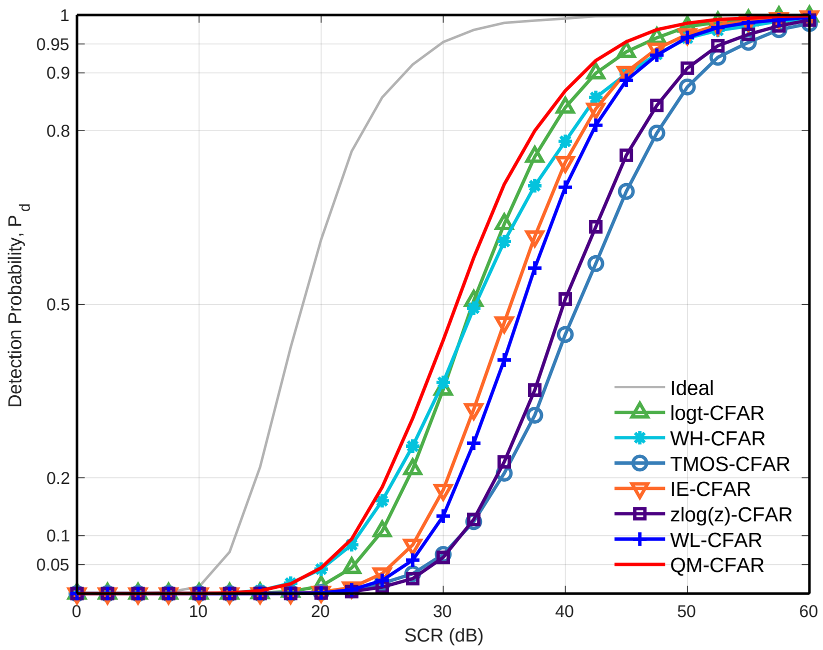

(b)

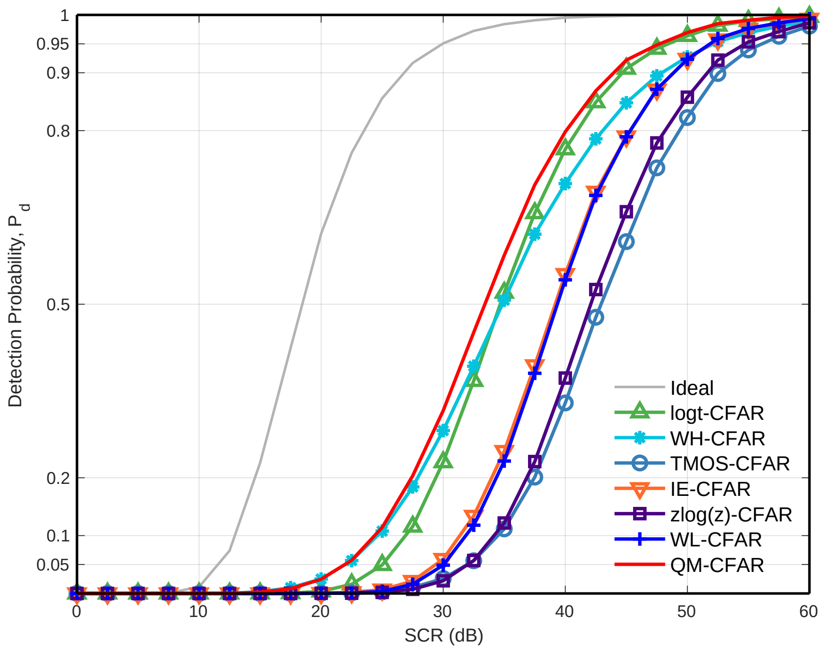

(c)

Figure 4.5: Detection probabilities ($\mathrm{P_D}$) against SCR of the different detectors in multiple target situations; for $N = 32, B = 0.0322, C = 0.9439$ and $P_{FA} = 10^{-4}$. (a) NIT = 2; (b) NIT = 3; (c) NIT = 4, at $ICR = 20dB$.

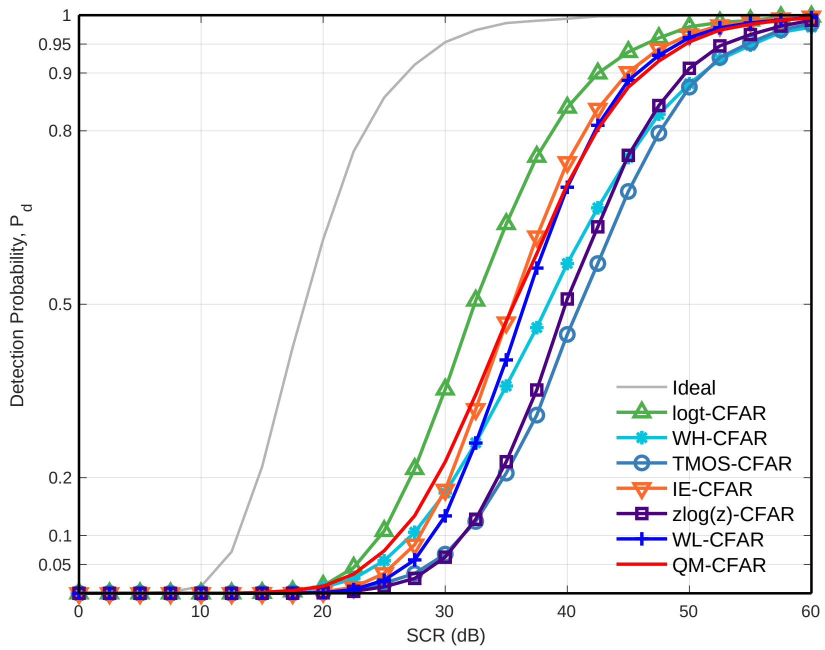

(a)

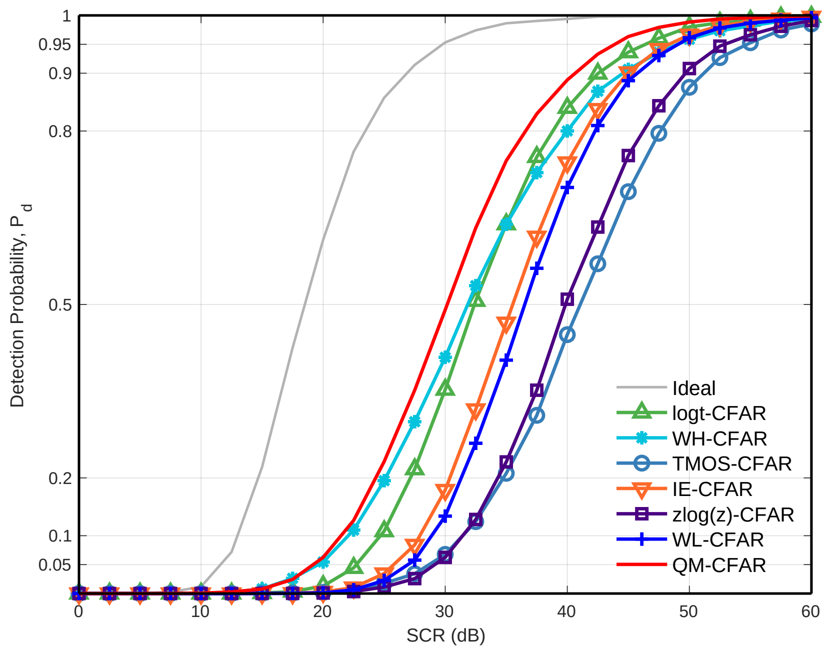

(b)

Figure 4.6: Detection probabilities ($\mathrm{P_D}$) against SCR of the different detectors in multiple target situations; for $N = 32$, $B = 0.0322$, $C = 0.9439$, $P_{FA} = 10^{-4}$ and NIT = 3 at $ICR = 20dB$. (a) Under censoring situation; (b) Over censoring situation.

samples to estimate the clutter level, 48 samples as a guard and 1 sample as a CUT.

In Fig. 4.8, we compare all detectors for a large ship as an extended target. Fig. 4.8a

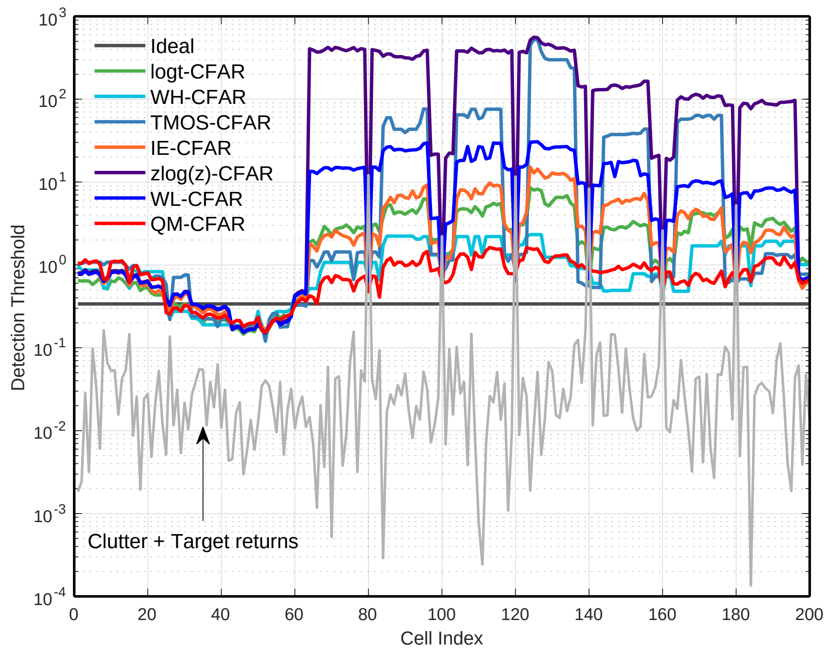

Figure 4.7: Detection thresholds of the different detectors in multiple target situations; for $N = 32, B = 0.0322, C = 0.9439$ and $P_{FA} = 10^{-4}$. Injected Rayleigh targets are located at the 80^{th}, 100^{th}, 120^{th}, 140^{th}, 160^{th}, and 180^{th} range cells at $SCR = 20dB$.

shows the original SAR image. In this example, despite using guard pixels, some pixels in the SRW are still contaminated with returns from an extended target. These returns can be considered as interfering targets. The WH-CFAR detector offers some improvement compared to the other competitors. As shown in Fig. 4.8g, compared to WH-CFAR detector, the proposed QM-CFAR detector is superior in detecting the total number of target pixels while reducing the FAs.

4.5 Conclusion

In this chapter, we proposed and analyzed the QM-CFAR detector for a Weibull clutter and multiple target situations. Assuming a non-stationary Weibull clutter with the presence or not of interfering targets, the QM theory and the MLE have been used to allow the detection threshold to perform fixed censoring of the upper end of the reference window cells. We first showed through MC simulations that the QM detector guarantees the CFAR property irrespective of the scale and the shape parameters. Then, we compared its detection performances to some recent CFAR algorithms. We showed that, due to the accurate estimates of the Weibull distribution parameters, the QM-CFAR achieves an optimal $\text{CFAR}_{\text{Loss}}$

in both homogeneous clutter and multiple target situations. However, its detection performance becomes suboptimal whenever it is confronted to under censoring situations. Finally, we validate the superiority of the proposed QM-CFAR through SAR image. The QM-CFAR detector acquires a high detection performance and fair P_{FA} regulation with regard to the challenging state-of-the-art detectors.

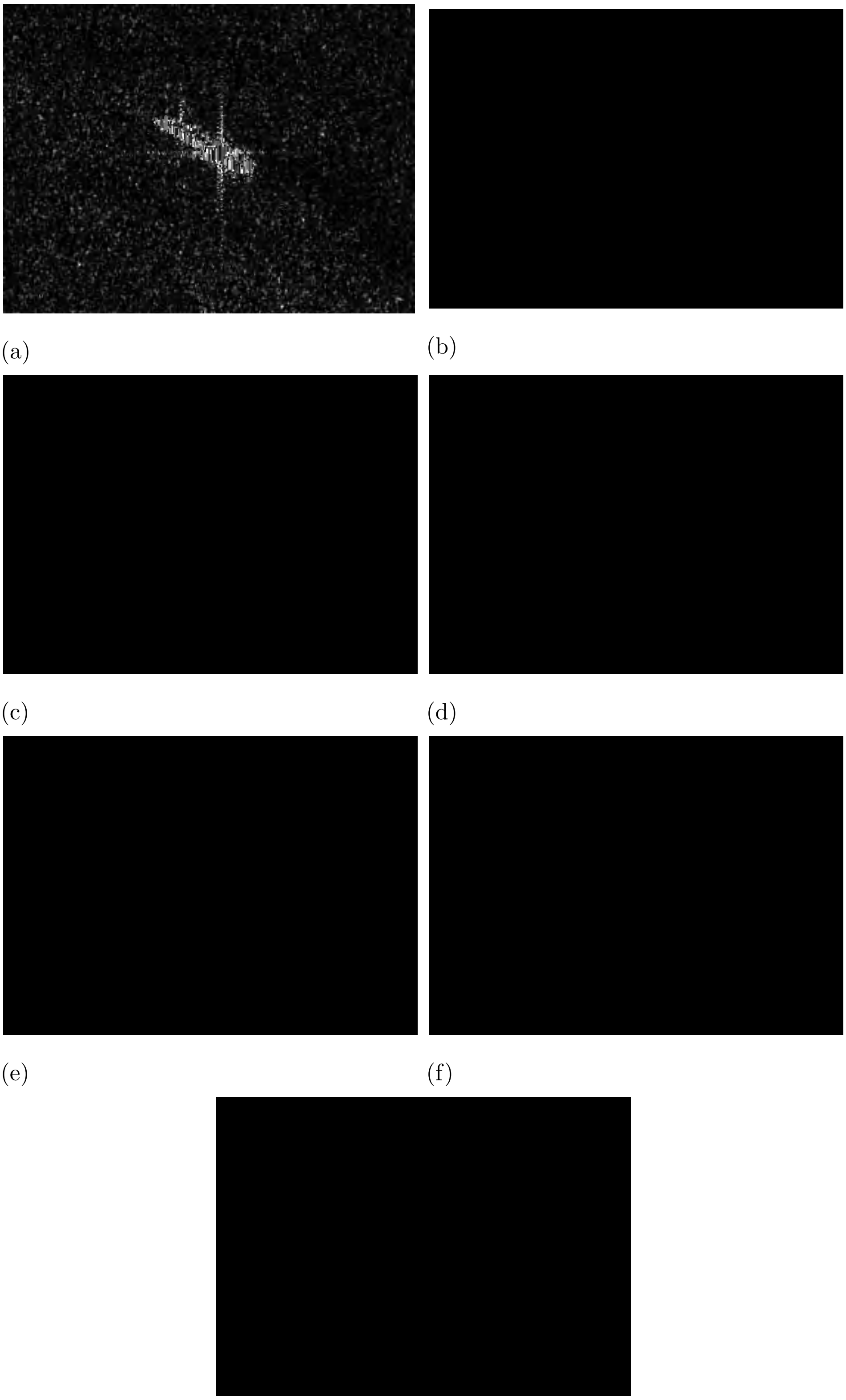

(a) (b)

(c) (d)

(e) (f)

(g)

Figure 4.8: Detection performance comparison on extended ship target. SAR image is applied with $P_{FA} = 10^{-5}$ on TerraSAR-X image. (a) Original SAR image, (b) CA-CFAR, (c) logt-CFAR, (d) WH-CFAR, (e) zlog(z)-CFAR, (f) WML-CFAR, (g) QM-CFAR.

Chapter 5

MAD-CFAR Detection for Ship Targets in Log-normal Sea Clutter in SAR imagery

Summary

This chapter constitutes our second contribution to CFAR ship detection in SAR imagery. In doing this, we propose and analyze the performance of the MAD-CFAR (Median Absolute Deviation) detector in the presence of multiple targets and oil spill embedded in a Log-normal sea clutter. In order to be confined to a real case of radar detection, i.e., no *a priori* knowledge of the homogeneity or heterogeneity of the clutter, we develop the MAD-CFAR detector in presence of both low/high contaminations. We show, through both simulated and real SAR images, the effect of the clutter parameters estimators on the detection thresholds of the MAD-CFAR detector.

5.1 Introduction

With the rising volume of image data collected from airborne and spaceborne SAR systems, computer-aided or automated exploitation of SAR images, particularly for ATR systems, is becoming increasingly attractive. Ship detection, as the initial step of ATR systems for ship targets, provides a foundation for the validity of future identification. Over the previous two decades, many approaches for detecting ship targets from SAR images have been developed. Of those methods, the well-known CFAR is the most frequently used conceptual framework in both point and spread targets [75, 76, 77]. To utilize the CFAR method, first select an acceptable PDF or CDF that appropriately describes the statistical properties of the backscattering energy. In low-resolution SAR radars, the clutter generally obeys Gaussian distribution in the intensity domain or Rayleigh distribution in the amplitude domain [78, 79]. As the spatial resolution of SAR instruments increases, the associated reduction of scatterers per resolution cell lends to an increase of the appreciability of backscattering responses from distinct ground features. This means that SAR images with complex land/sea topologies now exhibit even more heavy-tailed models [41]; which have led to the development of newer PDF models with longer tails such as the most notable statistical models of log-normal, Weibull, K, Gamma, and compound-Gaussian distributions [80, 81, 82]. Latest trends of clutter modeling deal with mixture models. Yi *et al.* [42] proposed the LMM-CFAR (Log-normal Mixture Model-CFAR) ship detector. The LMM enables to model complex distributions in a similar way to Parzen-Window-Kernel-based CFAR detector proposed by Gao [54]. This approach is adaptive to the clutter variation over the image.

Most of the cited CFAR detectors are implemented with the standard SRW scheme, with a guard region configured to prevent ship targets parts from leaking into the background region. However, in practice, the clutter in the SRW is contaminated by outliers, especially in crowded harbors and busy shipping lines. Recently, numerous researches have been carried out on the approaches of selecting background pixels to eliminate the influence of the non-clutter pixels or outliers. To dispose the effect of the target pixels near the PUT, Pappas *et al.* [41] proposed a superpixel-level CFAR detection method. It utilizes superpixels instead of rectangular sliding windows to define CFAR guard areas and clutter. The objective is to enhance target exclusion from outliers while reducing false detections. Tao *et al.* [47] proposed the TS-CFAR detector. This latter uses data truncation to eliminate all potential statistical outliers; the remaining truncated statistics are utilized for rigorous clutter modeling. If the pixel intensity is higher than a specified truncation rate, for example, 25% of the samples are discarded, they are excluded from the training samples and truncated data is used to estimate clutter statistics. This detector improves the P_D, but the FAR inevitably rises due to the non-exclusion of the high-intensity clutter pixels from the SRW. Recently, Ai *et al.* [83, 84] proposed multiple CFAR detectors based on censoring methods; namely, the two-parameter LNTS-CFAR (Log-Normal Truncated Statistics-CFAR) detector based on the adaptively truncated clutter statistics, and the BTSR-CFAR (Robust Bilateral-Trimmed-Statistics-CFAR) detector. While the former improves the P_D in multiple target environments, the latter greatly eliminates the capture effect arising in conventional CFAR detectors. Furthermore, the parameters and the local detection threshold can be acquired through simple calculation, without any iterative numerical solutions. The specific problem addressed here is how to deal with distribution models of SAR data when the sea clutter is statistically contaminated by outliers. The suggested solution is the use of the Median Absolute Deviation, commonly shortened to MAD, as it is robust and fast, and does not rely on any bulky estimation method [85]. The newly presented MAD-CFAR detector only sets a background test window which does not take into consideration any design of guard pixels. Furthermore, due to the simple calculation of the median and the MAD, its detection threshold can be computed straightforwardly; yielding a significant gain in the processing time.

The rest of this chapter is devoted to the exposition of this new MAD-CFAR detector.

5.2 Analysis of the MAD-CFAR Detector

The concept map of the proposed MAD-CFAR detector is shown in Figure 5.1. The general structure of this detector is such that the SAR image is passed through a logarithmic amplifier to transform, before storing them in a new image. The logarithm can be considered in an arbitrary base, however, throughout this manuscript the natural logarithm is used. The main advantage of this logarithmic transformation lies in the use of an LS (Location Scale) type distribution. Since the sea clutter intensity PDF meets the log-normal distribution, the log-intensity value follows the Gaussian distribution.

The content of the sliding window, i.e., the random variables, except for the PUT (Pixel Under Test), are sorted in ascending order according to their amplitudes (or powers) to obtain the samples, which will be processed first by the estimation algorithm and then by the detection algorithm. The rest of this chapter is devoted to the exposition of this new MAD-CFAR detector.

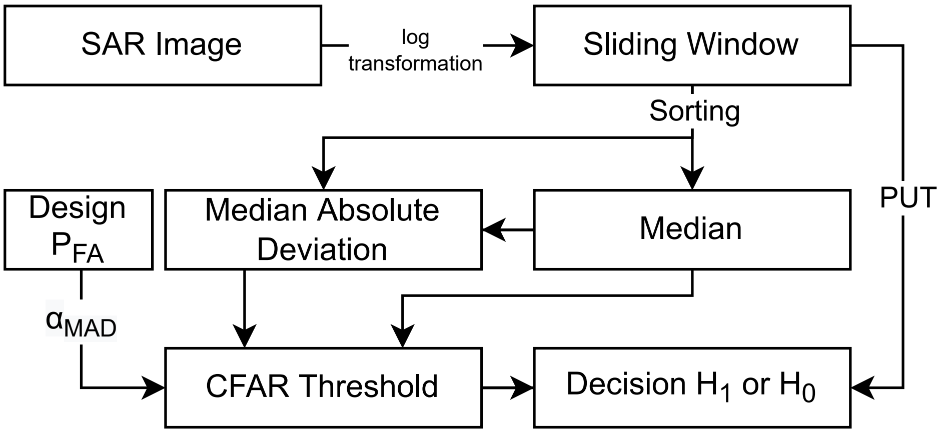

Figure 5.1: Concept map of the MAD-CFAR detector

5.3 Heuristic MAD Thresholding Derivation

In statistics, the MAD is a reliable measure of the variability of a univariate sample of quantitative data. Absolute deviation from the median was discovered and popularized by Hampel (1974) who attributes the idea to Gauss (1777–1855). The median is, like the mean, a measure of central tendency but offers the advantage of being very insensitive to the presence of outliers. Consider a set of N clutter samples in the local reference window, for which $X = \{X_i\}_{i=1}^{N}$ obeys a log-normal PDF, X_i being the intensity value of the i^{th} sample of the clutter in the local reference window. Since the sea clutter intensity PDF meets the log-normal distribution, the log-intensity value $ln(X)$ follows the Gaussian distribution. Calculating the MAD of the resulting set of samples is straightforward, as it only involves finding the median of absolute deviations from the median. More precisely, the MAD is defined as follows [85]

$$\mathrm{MAD} = \mathrm{median}(\mid X - \tilde{X} \mid) \tag{5.1}$$

where $\tilde{X} = \text{median}(X)$ is the median of the samples. Henceforth, the ship targets detection algorithm of the MAD-CFAR refers to declaring a target if

$$X_0 \underset{H_0}{\overset{H_1}{\underset{\leq}{>}}} T_{\text{MAD}} = \tilde{X} + \alpha_{\text{MAD}}\text{MAD} \tag{5.2}$$

where T_{MAD} is the adaptive detection threshold and X_0 is the Pixel Under Text (PUT). The binary hypotheses H_1 and H_0 refer to PUT belongs either to a target or to the clutter, and α_{MAD}, is the scale factor to maintain the design value of the P_{FA}.

The coefficient α_{MAD} of the adaptive detection threshold T_{MAD} is obtained in such a way that the P_{FA} is kept constant for a homogeneous environment. Therefore, knowing that the is defined by

$$\begin{aligned} P_{FA} = \quad & Prob\left\{X_0 > \hat{T}_{\text{MAD}} \mid H_0\right\} = \text{Constant} \\ P_{FA} = \quad & Prob\left\{\frac{X_0 - \tilde{X}}{\text{MAD}} > \alpha_{\text{MAD}} \mid H_0\right\} = \text{Constant} \end{aligned} \tag{5.3}$$

The scale factor α_{MAD} can be obtained through the ICDF of the standard normal, i.e., N(0, 1) distribution as

$$\alpha_{\text{MAD}} = c\ \phi^{-1}(1 - P_{FA}) \tag{5.4}$$

where $\phi^{-1}(\cdot)$ is the ICDF of the standard normal distribution and c = 1.4826 is the consistency constant of the MAD to be a consistent standard deviation estimator of a Normal distribution [85]. Therefore, for $P_{FA} = 10^{-5}$, we obtain, from Eq. (5.4), $\alpha_{\text{MAD}} = 6.3231$.

Moreover, since the pdf of does not have an analytical form for a Log-normal clutter, we resort to Monte Carlo simulations to determine the P_D defined by

$$P_D = Prob\left\{X_0 > \hat{T}_{\text{MAD}} \mid H_1\right\} \tag{5.5}$$

Next, we investigate the CFAR property of the proposed detector along with performance. In doing this, for simulation purposes, we compare the proposed MAD-CFAR detector to three recent studies that have been conducted to deal with heterogeneous sea surfaces [42, 83, 84]. Namely, the LMM-CFAR detector proposed by Cui *et al.* [42], the LNTS-CFAR and the BTSR-CFAR [83, 84] proposed by Ai *et al.* We also introduce the SDM-CFAR detector. That is, unlike the MAD-CFAR detector, the SDM-CFAR detector uses a threshold which relies on the mean and the standard deviation of the background clutter.

CFAR property

Due to the difficulties that arise in the derivation of an analytic expression of the P_{FA}, we validate the CFAR property of the MAD-CFAR detector through extensive MC simulations. In doing this, we resort to the Matlab R2022a, installed on a Laptop powered by an Intel Core 7 CPU (Central Processing Unit), with a speed of up to 2.8 GHz (Giga Hertz) and a RAM (Random Access Memory) of 16 GB (Giga Bytes). To begin the numerical analysis, let us consider that the basic simulation scenario is a simulated 512×512 image, embedded in a log-normal clutter with log-mean value $\mu_{ln} = 3$ and log-standard-deviation value $\sigma_{ln} = 0.2$. The sliding window size is set to 41×41.

Fig. 5.2 shows the CFAR property of the proposed detector for a design P_{FA}=10^{-5}. Specifically, Fig. 5.2a, shows the experimental P_{FA} of all detectors with respect to μ_{ln} whose values range from 0.2 to 3 with step 0.2, and a fixed value $\sigma_{ln} = 0.2$.

Similarly, Fig. 5.2b, shows the CFAR property of all detectors with respect to the log-standard-deviation σ_{ln} parameter whose values range from 0.1 to 4.3 with step 0.3 and a fixed log-mean value $\mu_{ln} = 3$. Despite the fact that the curves have minor departures from the design P_{FA}, the inferred values are likewise realistic in real-world applications. As a result, all detectors are also CFAR with respect to the log-standard-deviation σ_{ln}.

5.4 Experimental Results

5.4.1 Simulated SAR Image

Next, we evaluate the detection performances of the MAD-CFAR detector against the remaining ones on a simulated SAR image. Fig. 5.3a corresponds to the simulated SAR image of size 512×512 pixels, used to evaluate the virtue of the MAD-CFAR in complex sea scenarios. In this case, we assume that the simulated sea clutter follows a log-normal law with $\mu_{ln} = 3$ and $\sigma_{ln} = 0.2$. The image includes the densely-distributed ship target area as marked by the white solid ellipse, the land, a few ships and the ship-oil-mixed area marked by the white solid rectangle. The intensity values of the ship targets are evenly distributed between 1.4 and 1.8 times the maximum value of the sea clutter. While the land and breakwater are simulated through a log-normal distribution with $\mu_{ln} = 3.8$ and $\sigma_{ln} = 0.2$, the intensity values of the spilled-oil are evenly distributed between 0.1 and 0.3 the minimum value of the sea clutter. Fig. 5.3b corresponds to the GT image of Fig. 5.3a.

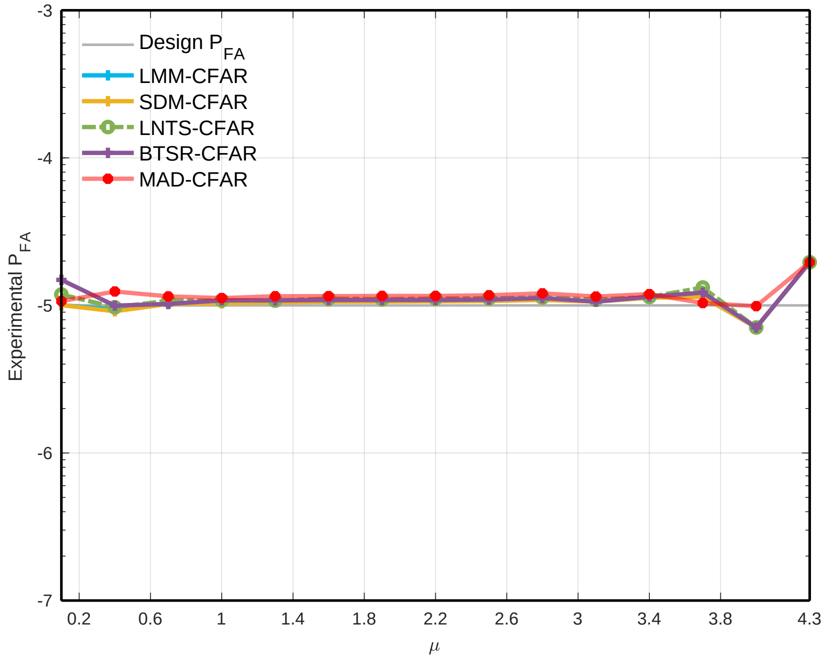

(a)

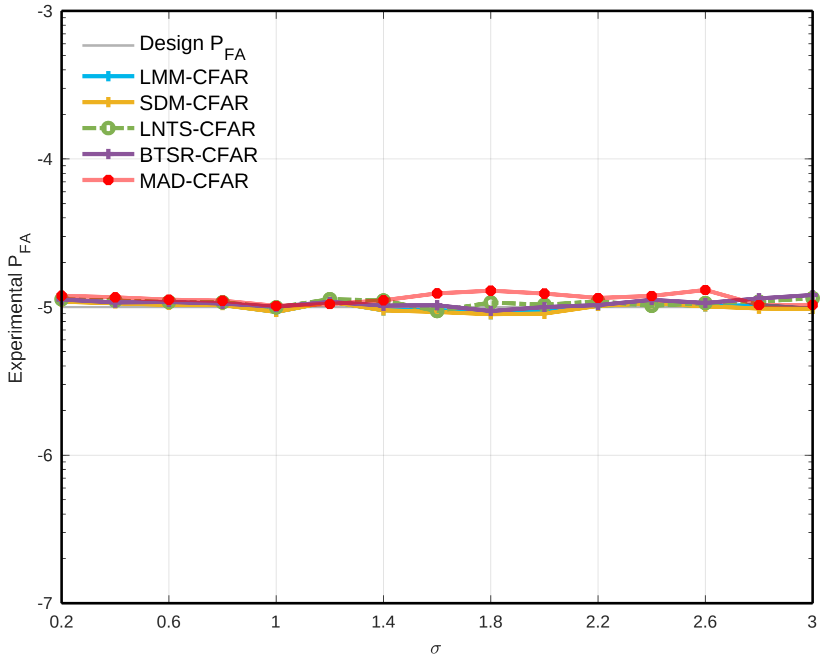

(b)

Figure 5.2: CFAR property of the MAD-CFAR, LMM-CFAR, SDM-CFAR, LNTS-CFAR and BTSR-CFAR detectors; for $P_{FA} = 10^{-5}$ with respect to (a) log-mean parameter $\mu_{ln} = 3$ and (b) log-standard-deviation parameter σ_{ln}.

For $P_{FA} = 10^{-5}$, Fig. 5.3c–g show the detection outcome images of the MAD-CFAR detector versus the existing ones in the heterogeneous scenario described above and represented by Fig. 5.3a. It can clearly be seen that the MAD-CFAR detector identifies all pixels of all ship targets. In contrast, except the BTSR-CFAR detector which misses only one ship target, i.e., 68 pixels, the LNTS-CFAR, SDM-CFAR and LMM-CFAR detectors miss quite a lot of the ship targets (red circles), i.e., 678, 827, and 1200 missing pixels, respectively.

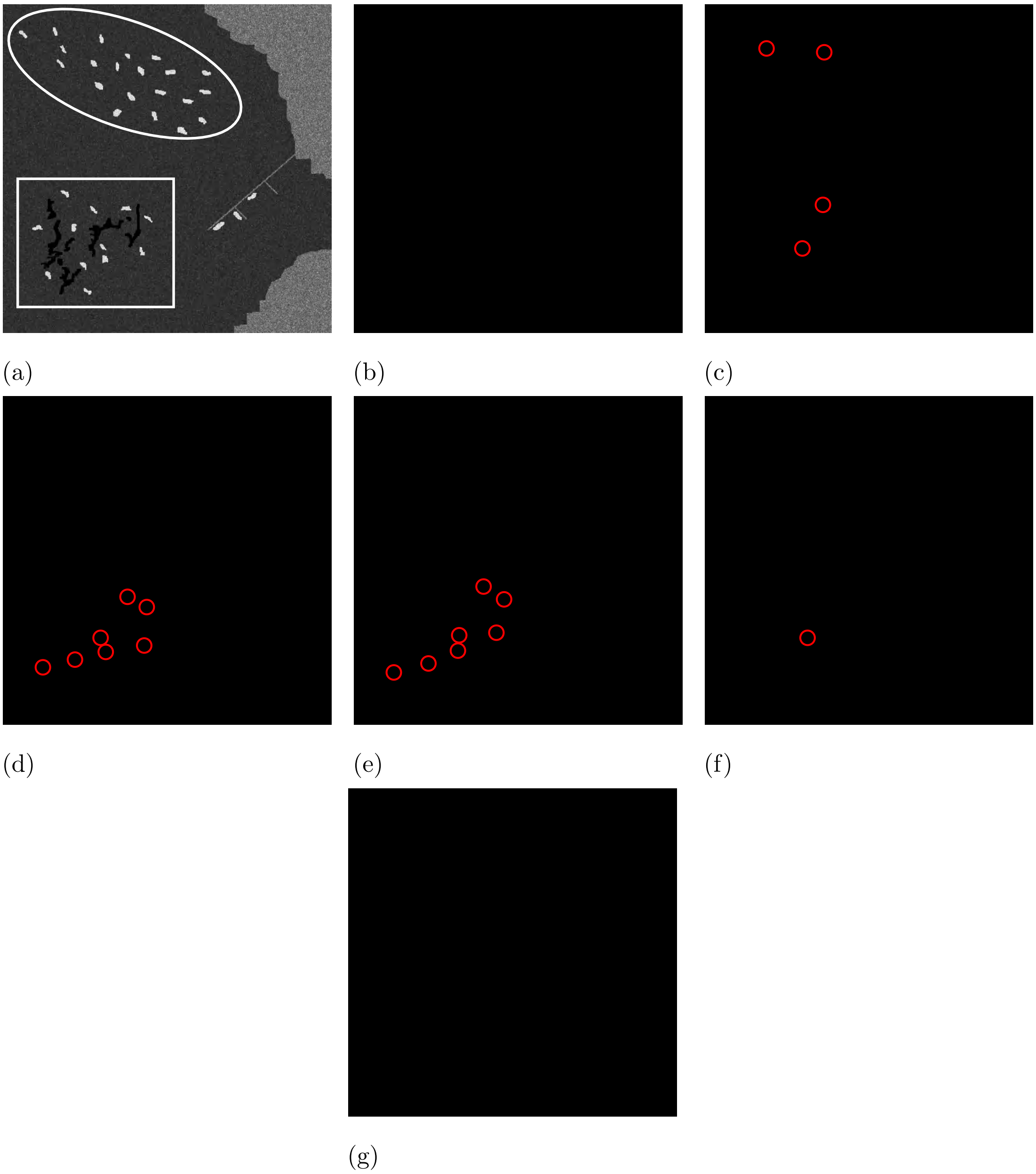

Figure 5.3: Detection performances of all detectors in a heterogeneous scenario for $P_{FA} = 10^{-5}$; (a) Simulated SAR image, (b) Corresponding GT image, (c) LMM-CFAR detector, (d) SDM-CFAR detector (e) LNTS-CFAR detector with $\gamma = 1$, (f) BTSR-CFAR detector with $t_1 = 2$ and $\gamma = 0.7$, (g) MAD-CFAR detector. The red circles denote missing targets.

5.4.2 Real SAR Images

In addition to the simulated SAR image, as shown in Figs. 5.4a–c, the performances of the MAD-CFAR detector are also assessed through three real images; two produced by the TerraSAR-X, and one by the Sentinel-1. It is worth noting that the real SAR images are embedded in a log-normal background with only densely-distributed ship targets. Recall that the images of Figs. 5.4a–b have been acquired by the StripMap mode, respectively, on September 14, 2014, over China (Longitude E119 and Latitude N37), and on January 22, 2019, over The Netherlands (Longitude E006 and Latitude N53). The image of Fig. 5.4c has been acquired by the Interferometric Wide mode on September 20, 2022, over China (Longitude E116 and Latitude N23) [86, 87].

In order to validate the proposed method, the observed detection metrics, namely the Detection Rate (DR) or P_D and FAR or P_{FA} are introduced to evaluate quantitatively the detectors performances through the following expressions

In order to further validate the proposed method, the observed detection metrics, namely the DR (Detection Rate) and FAR are introduced to evaluate quantitatively the detectors performances through the following expressions

$$\mathrm{DR} = \frac{N_{DT}}{N_{GT}} 100\% \tag{5.6}$$

where N_{TD} is the number of total true detections in either simulated or real SAR image and N_{GT} is the number of target pixels in their corresponding GT images,

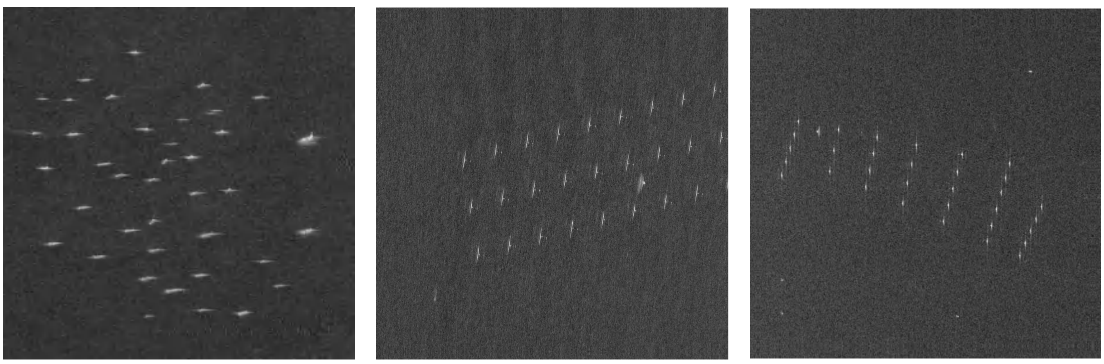

(a) (b) (c)

Figure 5.4: Real SAR images. (a) 571 × 575 TerraSAR-X SAR image, (b) 1678 × 2598 TerraSAR-X SAR image, (c) 1037 × 1612 Sentinel-1 image.

and

$$\text{FAR} = \frac{N_{FA}}{mn - N_{GT}} \tag{5.7}$$

Table 5.1: DR metric of all detectors for the simulated and real SAR images (Bold numbers designate the results of the MAD-CFAR detector).

Detector	LMM-CFAR	SDM-CFAR	LNTS-CFAR	BTSR-CFAR	MAD-CFAR
Simulated SAR image (Fig. 5.3a)	22.79%	18.49%	73.55%	75.80%	**96.04%**
CPU time (Sec)	63.48	3.21	6.55	21.04	**16.65**
Real SAR image (Fig. 5.4a)	34.93%	82.54%	88.83%	93.33%	**99.91%**
CPU time (Sec)	25.10	1.15	2.19	5.86	**4.86**
Real SAR image (Fig. 5.4b)	17.73%	51.60%	72.31%	73.35%	**88.62%**
CPU time (Sec)	265.71	14.42	30.09	80.733	**67.37**
Real SAR image (Fig. 5.4c)	50.32%	84.26%	84.69%	87.82%	**96.87%**
CPU time (Sec)	104.26	5.53	11.70	30.86	**24.27**

where N_{FA} is the number of false alarms, m and n the dimensions of either the simulated or the real SAR image. Note that, due to a lack of space, neither the corresponding GT images of the three real images of Figs. 5.4a–c, nor the outcome images of all detectors are shown here. Instead, Tables 5.1 and 5.2 summarize, respectively, the DR and the CPU time, and the experimental FAR of all detectors yielded from both the simulated and the real SAR images. By CPU time, we merely intend to estimate and compare the consumption time of all detectors via the "`tic-toc`" Matlab built-in function, i.e., the time between the start and the completion of a given detector's routine. It should be noted that we perform multilooking on Figs. 5.4a–c by averaging non-overlapping pixel blocks of size 2×2, to alleviate the spatial dependence and increase the SCR.

Inspection of Table 5.1 (rows 1-2), for the simulated SAR image of Fig. 5.3a, reveals that due to the presence of high-intensity outliers of the interfering ship target pixels, land/breakwater and spilled-oil in the local reference window, the MAD-CFAR detector, and to a lesser degree, the BTSR-CFAR and the LNTS-CFAR detectors are robust. That is, their respective scores indicate only few missing pixels, i.e., 102, 624 and 682. On the other hand,

Table 5.2: Experimental P_{FA} or FAR metric of all detectors for the simulated and real SAR images (Bold numbers designate the results of the MAD-CFAR detector).

Detector	LMM-CFAR	SDM-CFAR	LNTS-CFAR	BTSR-CFAR	MAD-CFAR
Simulated SAR image (Fig. 5.3a)	$1.54\ 10^{-5}$	$1.15\ 10^{-5}$	$21.18\ 10^{-5}$	$10.01\ 10^{-5}$	$\mathbf{37.37\ 10^{-5}}$
Real SAR image (Fig. 5.4a)	$22.3\ 10^{-5}$	$26.0\ 10^{-5}$	$1.24\ 10^{-5}$	$3.72\ 10^{-5}$	$\mathbf{39.63\ 10^{-5}}$
Real SAR image (Fig. 5.4b)	$3.31\ 10^{-5}$	$2.66\ 10^{-5}$	$2.57\ 10^{-5}$	$2.57\ 10^{-5}$	$\mathbf{3.31\ 10^{-5}}$
Real SAR image (Fig. 5.4c)	$4.32\ 10^{-5}$	$7.44\ 10^{-5}$	$3.36\ 10^{-5}$	$3.84\ 10^{-5}$	$\mathbf{6.72\ 10^{-5}}$

the LMM-CFAR and the SDM-CFAR detectors remain the worst of them all, with a lot of missing pixels, i.e., 1991 and 2102, respectively.

Likewise, for the real SAR images of Figs. 5.4a–c, Table 5.1 (rows 3-8) also shows that the MAD-CFAR is the only detector that achieves the highest P_D, and then comes the BTSR-CFAR and the LNTS-CFAR detectors with reasonable scores. For its part, the SDM-CFAR detector seems to catch up more or less with the previous detectors. Finally, the LMM-CFAR does not show any improvement with respect to the simulated SAR image. Notice that the BTSR-CFAR detector is the only one that tracks the MAD-CFAR detector in both DRs and CPU times. The LMM-CFAR detector, however, realizes the lowest scores.

Table 5.2 summarizes the experimental P_{FA} or FAR of all detectors. As stated earlier, even though the FAR of the MAD-CFAR detector slightly departs from the design P_{FA} for the simulated SAR image of Fig. 5.3a and the real SAR images of Figs. 5.4a–c, the inferred values are realistic in real-world applications.

5.5 Conclusion

In this chapter, we analyzed the detection algorithms of the MAD-CFAR detector for a heterogeneous Log-normal sea clutter without any prior knowledge of the presence or not of a clutter edge and/or interfering targets in the sliding window. In doing so, we first showed heuristic MAD thresholding derivation. Then, we validate the CFAR property of the MAD-CFAR detector through extensive MC simulations. Finally, we have analyzed and evaluated through simulated and real SAR images the detection performances of the MAD-

CFAR detector in a log-normal sea clutter when no prior knowledge is made available about the number of interfering targets and/or any other sea clutter heterogeneities, such as targets, off-shore oil-spilled sea areas and land. The MAD-CFAR detector makes use of the median absolute deviation, which is less affected by outliers and easier to implement than the standard deviation based detector. The MAD-CFAR detector acquires higher detection performances and a faster CPU processing time than the first challenging BTSR-CFAR detector.

Chapter 6

AMLE Based Automatic Bilateral Censoring CFAR Ship Detection for Log-Normal Sea Clutter in SAR Imagery

Summary

This chapter constitutes our third contribution to CFAR ship detection in SAR imagery. To this effect, we the AML-CFAR detector in the presence of complex scenes of log-normal sea clutter. In order to be confined to a real case of radar detection, i.e., no *a priori* knowledge of the homogeneity or heterogeneity of the clutter, we develop the CFCR algorithm suited for the bilateral censoring of undesirable samples and the CFAR detection of the primary targets. That is, resorting to linear biparametric adaptive thresholds for both censoring and detection algorithms, we introduce a logarithmic amplifier to get a transformed Gaussian distribution. Assuming a homogeneous middle half ranked sub-SRW, we first compute the lower and upper censoring thresholds through the closed form solutions of the AML estimates of the unknown mean and standard deviation parameters. Then, upon censoring of both ends, we use the remaining set of data to estimate the unknown distribution parameters through the AMLs to yield the detection threshold. Base on the accuracy of the AMLs of the clutter parameters, we show, through MC simulations, the robustness of the AML-CFAR detector.

6.1 Introduction

The empirical distributions have no sound deduction in theory. They come from the experience of analyzing real data. Several empirical models have been used to characterize the statistics of SAR amplitude or intensity data, such as Weibull, log-normal, and K distributions, Table 3.1. Among the goals expected by researchers in the field of radar detection, we find the design of robust CFAR detectors in a Gaussian or non-Gaussian clutter, homogeneous or heterogeneous, i.e., presence of a clutter edge and/or interference in the reference window, correlated or uncorrelated [88]. In the case of a non-Gaussian clutter, some works have been able to solve independently the problem of the automatic localization of a clutter edge and that of the interfering targets [89, 90]. Nevertheless, in some real-life situations, we have to detect targets when these two clutter heterogeneities are concomitant. We note that the detection of ship targets embedded in a non-Gaussian and heterogeneous clutter becomes complex because of the inability of existing detectors to jointly localize the clutter edge and the interferences both present in the reference window. Moreover, since the clutter is non-stationary, with the exception of the non-parametric WH-CFAR detector [66], all other detectors [89, 90] require real-time estimation of the parameters of the distribution that models the clutter. Therefore, the quality of CFAR detection depends on several important factors, including the choice of the estimators and the choice of automatic censoring and detection algorithms [88]. It is in this perspective that we intend to propose and analyze the performances of the AML-CFAR detector. It is a detector dedicated to improving the performance of the detection of primary ship targets embedded in a Log-normal clutter. Therefore, to perform ship target detection, we first resort to a CFCR algorithm by assuming a homogeneous middle half ranked sub-SRW and compute the lower and upper censoring thresholds, which guarantees an accurate rejection of an *a priori* unknown number of outliers. Then, based on a CFAR algorithm, we estimate the detection threshold. In doing this, instead of using the MLEs of a censored normal distribution, which need quite complex and inefficient iterative numerical calculations [84], here we make use of the AML estimators to generate closed-form expressions of the mean and standard deviation parameters. Note that the AML estimators have been shown to be valuable in statistical theory [91, 92].

The rest of this chapter is organized as follows. In Section 2, we first introduce and discuss the general flowchart of the AML-CFAR ship detector. We then introduce the joint ordered statistics PDF to yield the likelihood equations of the mean and standard deviation

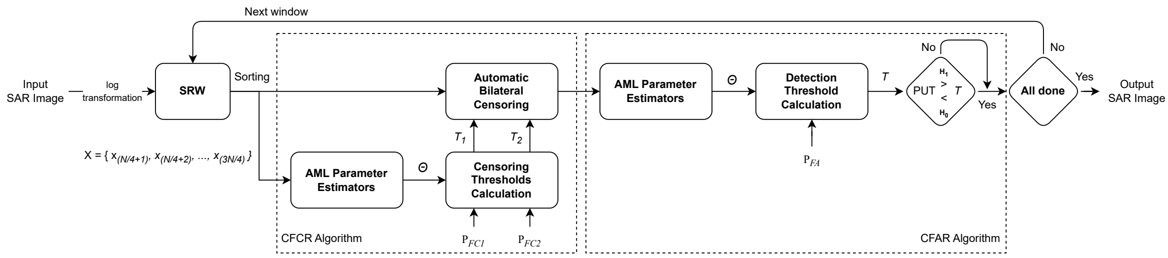

Figure 6.1: General flowchart of the proposed AML-CFAR detector.

of the log-normal distribution in the log intensity domain. We finally determine the bilateral CFCR thresholds and the CFAR threshold through the AMLEs of their respective means and standard deviations, and summarize the main steps of the AML-CFAR ship detector. In Section 3, first, we assess the AMLEs performances of the mean and standard deviation of the transformed Gaussian distribution in terms of the upper and lower P_{FC} (Probabilities of False Censoring). Then, we show the CFAR property of the AML-CFAR detector and compare, via a series of experiments conducted on simulated and real SAR images, the detection and P_{FA} regulation of the proposed detector to the prevailing detectors in the radar literature. Finally, in Section 4, we summarize the contribution of this work and conclude the paper.

6.2 Proposed AML-CFAR Detector

Fig. 6.1 summarizes the detection process of the proposed AML-CFAR detector. First, rank in ascending order the pixels within the SRW. Next, consider the assumption that a fixed portion of the clutter is uncontaminated by outliers. Then, estimate the initial parameters of the clutter using the AMLEs to censor out outliers. Here, the selected outlier-free portion runs from the $(N/4+1)^{\text{th}}$ pixel to the $(3N/4)^{\text{th}}$ pixel. That is, 25% of the upper pixels and 25% of the lower pixels are assumed to be contaminated by outliers. Based on the initially estimated parameters, the lower threshold T_1 and the upper threshold T_2 are determined according to the desired P_{FC_1} and P_{FC_2}, respectively. Then, the pixels in the SRW are automatically censored using T_1 and T_2 in such a way that outliers like interfering ship target pixels, ghosts, side-lobes, breakwaterd, spilled oil, etc. are removed. Next, using the AMLE again, the final parameters are estimated via the remaining clutter pixels. Only then, the scale factor is determined according to the desired P_{FA}, and the detection threshold T computed, to be compared to the PUT, according to the following hypothesis test

$$PUT \underset{H_0}{\overset{H_1}{\gtrless}} T \tag{6.1}$$

where H_0 designates the null hypothesis and H_1 the alternative hypothesis. The process is repeated until all pixels of the input image are depleted.

Let $X = \{X_{(k_i)}\}_{i=1}^{N}$ be the rank ordered clutter pixels within the SRW, i.e., $X_{(k_1)} \leq X_{(k_2)} \leq \cdots \leq X_{(k_N)}$, $K = \{k_i\}_{i=1}^{N}$ their corresponding order, and $X_{(k_i)}$ the ${k_i}^{th}$ ordered statistic of the RV (Random Variable) X whose PDF and CDF are $f_X(x)$ and $F_X(x)$, respectively.

It is well known that the presence of outliers within the reference window can drastically degrade the performance of a CFAR detector. In fact, as the outliers affect the distribution parameters estimates, CFAR detectors require an outlier-free reference window. To this effect, we introduce the joint distribution of the ordered statistics X, which enables censoring at both ends using a general formula suited for all distributions [93].

Suppose that after having removed all outliers, the remaining clutter pixels become $X = \{X_{(k_i)}\}_{i=1}^{M}$ where $M = N - r_1 - r_2$. Their corresponding order are $K = \{k_i\}_{i=r_1+1}^{N-r_2}$ where r_1 and $r_2 = 0,\ 1,\ 2,\ \ldots$ are the numbers of removed outliers with lower and higher intensities, respectively. Thus, in order to estimate the parameter θ from the remaining pixels $X \in R^M$ and their corresponding order $K \in N^M$, we need to know the conditional joint PDF $p_{X_{(k_1)},X_{(k_2)},\cdots,X_{(k_M)}|\Theta}(x_{(k_1)}, x_{(k_2)}, \cdots, x_{(k_M)} \mid \theta)$ of the ordered statistics, which is shown to be [93]

$$p_{X|K,\Theta,N}(x \mid K, \theta, N) = \eta F_{X_{(k_1)}|\Theta}(x_{(k_1)} \mid \theta)^{k_1-1}(1-F_{X_{(k_M)}|\Theta}(x_{(k_M)} \mid \theta))^{N-k_M} \prod_{i=1}^{M} f_{X_{(k_i)}|\Theta}(x_{(k_i)} \mid \theta) \tag{6.2}$$

where η is a normalization constant given by

$$\eta = \frac{N!}{(k_1 - 1)!(N - k_M)!} \tag{6.3}$$

Note that the conditional joint PDF of Eq. (6.2) is parameterized by θ, which needs to be estimated. The likelihood function is defined as

$$L(\theta) = p_{X|K,\Theta,N}\,(x \mid K, \theta, N) \tag{6.4}$$

The estimate $\hat{\theta}$ that maximizes the likelihood function is computed through the MLE of θ. Because the logarithm is a monotonically increasing function, maximizing $L(\theta)$ is equivalent to maximizing $\ln L(\theta)$, ln designate the natural logarithm. Hence, it can be shown that a necessary but not sufficient condition to obtain the ML estimate $\hat{\theta}$ is to solve the following log-likelihood equation

$$\frac{\partial \ln L(\theta)}{\partial \theta} = 0 \tag{6.5}$$

Recall that the PDFs of the sea clutter intensity and its transformed log-intensity ($X_{(k_i)} = \ln Y_{(k_i)}$) obey, respectively, the log-normal and normal distributions as [94]

$$f_{Y_{(k_i)}}(y_{(k_i)}) = \frac{1}{\sqrt{2\pi}\sigma y_{(k_i)}} exp\left(-\frac{(\ln(y_{(k_i)}) - \mu)^2}{2\sigma^2}\right) \tag{6.6}$$

$$f_{X_{(k_i)}}(x_{(k_i)}) = \frac{1}{\sqrt{2\pi}\sigma} exp\left(-\frac{(x_{(k_i)} - \mu)^2}{2\sigma^2}\right) \tag{6.7}$$

On the other hand, the CDF of Eq. (6.7) is given by [58]

$$F_{X_{(k_i)}}(x_{(k_i)}) = \frac{1}{2}\left[1 + \text{erf}\left(\frac{x_{(k_i)} - \mu}{\sigma\sqrt{2}}\right)\right] = \Phi\left(\frac{x_{(k_i)} - \mu}{\sigma}\right) \tag{6.8}$$

where $y_{(k_i)} \in \mathcal{R}_{>0}$, $x_{(k_i)} \in \mathcal{R}$, for $i = 1, 2, ..., M$, $\mu \in \mathcal{R}$, $\sigma \in \mathcal{R}_{>0}$, erf(.) is the error function and $\Phi(x) = 1/\sqrt{2\pi}\int_{-\infty}^{x} \exp\left(-t^2/2\right) dt$.

Now, inserting Eqs. (6.7) and (6.8) into Eq. (6.4) or Eq. (6.2), yields the likelihood function as

$$L(\mu, \sigma) = \Phi\left(\frac{x_{(k_1)} - \mu}{\sigma}\right)^{k_1 - 1}\left(1 - \Phi\left(\frac{x_{(k_M)} - \mu}{\sigma}\right)\right)^{N - k_M}\left(\frac{1}{\sigma}\right)^M \prod_{i=1}^{M} \exp\left(-\frac{(x_{(k_i)} - \mu)^2}{2\sigma^2}\right) \tag{6.9}$$

Taking the logarithm of both sides of Eq. (6.9), we get the log-likelihood function as

$$\ln L(\mu, \sigma) = (k_1 - 1)\ln\Phi\left(\frac{x_{(k_1)} - \mu}{\sigma}\right) + (N - k_M)\ln\left(1 - \Phi\left(\frac{x_{(k_M)} - \mu}{\sigma}\right)\right) - M\ln\sigma - \frac{1}{2}\sum_{i=1}^{M}\left(\frac{x_{(k_i)} - \mu}{\sigma}\right)^2 \tag{6.10}$$

Finally, maximizing Eq. (6.10) through Eq. (6.5) with respect to μ and σ, respectively, we get the following likelihood equations [92]

$$\frac{\partial \ln L(\mu, \sigma)}{\partial \mu} = -\frac{1}{\sigma}\left((k_1 - 1)\frac{\phi(\xi_{k_1})}{\Phi(\xi_{k_1})} - (N - k_M)\frac{\phi(\xi_{k_M})}{\bar{\Phi}(\xi_{k_M})} - \sum_{i=1}^{M}\xi_{k_i}\right) = 0 \tag{6.11}$$

and

$$\frac{\partial \ln L(\mu, \sigma)}{\partial \sigma} = -\frac{1}{\sigma}\left(M + (k_1 - 1)\xi_{k_1}\frac{\phi(\xi_{k_1})}{\Phi(\xi_{k_1})} - (N - k_M)\xi_{k_M}\frac{\phi(\xi_{k_M})}{\bar{\Phi}(\xi_{k_M})} - \sum_{i=1}^{M}\xi_{k_i}^2\right) = 0 \tag{6.12}$$

where $\xi_{k_i} = (X_{(k_i)} - \mu)/\sigma$, $i = 1, 2, ..., M$. $\phi(.)$, $\Phi(.)$ and $\bar{\Phi}(.)$ are, respectively, the PDF, the CDF and the CCDF (Complementary CDF) of the standard normal distribution. It is clear that the likelihood Eqs. (6.11) and (6.12) do not have a closed form except for $M = N$. Some numerical techniques to solve the simultaneous equations may be used, but these methods take quite a long time. Therefore, we consider a simple method to derive explicit forms of the AMLEs $\hat{\mu}$ and $\hat{\sigma}$ of μ and σ with no iterations involved. This is the object of the next subsection.

6.2.1 Approximate Maximum Likelihood Estimators

As the MLEs of the censored normal distribution parameters do not have explicit forms, they should be solved in an iterative way. Here, we propose a simple method to derive closed-form expressions of the AMLEs with no iterations, by expanding the nonlinear parts of the likelihood Eqs. (6.11) and (6.12) in Taylor series around some suitable points. The approximation method was first developed in [91] to find the AMLE of the scalar parameter in the Rayleigh distribution with left and right censoring. To do this, let the ordered pixel-associated probability be $p_{k_i} = k_i/(N+1)$ and its complement $q_{k_i} = 1 - p_{k_i}$ for $i = 1, 2, ..., M$. The idea is to expand the functions $\phi(\xi_{k_1})/\Phi(\xi_{k_1})$ and $\phi(\xi_{k_M})/\bar{\Phi}(\xi_{k_M})$ of Eqs. (6.11) and (6.12) in Taylor series around the points $\vartheta_{k_1} = \Phi^{-1}(p_{k_1})$ and $\vartheta_{k_M} = \Phi^{-1}(p_{k_M})$, respectively. We may then approximate them by [92]

$$\frac{\phi(\xi_{k_1})}{\Phi(\xi_{k_1})} \approx \alpha - \beta \xi_{k_1} \tag{6.13}$$

and

$$\frac{\phi(\xi_{k_M})}{\bar{\Phi}(\xi_{k_M})} \approx \gamma + \delta \xi_{k_M} \tag{6.14}$$

where

$$\alpha = \frac{\phi(\vartheta_{k_1})\left(1 + \vartheta_{k_1}^2 + \vartheta_{k_1}\frac{\phi(\vartheta_{k_1})}{p_{k_1}}\right)}{p_{k_1}} \tag{6.15}$$

$$\beta = \frac{\phi(\vartheta_{k_1})\left(\phi(\vartheta_{k_1}) + p_{k_1}\vartheta_{k_1}\right)}{p_{k_1}^2} \tag{6.16}$$

$$\gamma = \frac{\phi(\vartheta_{k_M})\left(1 + \vartheta_{k_M}^2 - \vartheta_{k_M}\frac{\phi(\vartheta_{k_M})}{q_{k_M}}\right)}{q_{k_M}} \tag{6.17}$$

and

$$\delta = \frac{\phi(\vartheta_{k_M})\left(\phi(\vartheta_{k_M}) - q_{k_M}\vartheta_{k_M}\right)}{q_{k_M}^2} \tag{6.18}$$

Substituting $\phi(\xi_{k_1})/\Phi(\xi_{k_1})$ and $\phi(\xi_{k_M})/\bar{\Phi}(\xi_{k_M})$, with their respective approximate expressions of Eqs. (6.13) and (6.14), in Eqs. (6.11) and (6.12), we get the following approximate likelihood equations

$$\frac{\partial \ln L(\mu,\sigma)}{\partial \mu} \approx -\frac{1}{\sigma}\Big((k_1-1)(\alpha-\beta\xi_{k_1})-(N-k_M)(\gamma+\delta\xi_{k_M})-\sum_{i=k_1}^{k_M}\xi_i\Big)=0 \tag{6.19}$$

and

$$\frac{\partial L(\mu,\sigma)}{\partial \sigma} \approx -\frac{1}{\sigma}\Big(M+(k_1-1)\xi_{k_1}(\alpha-\beta\xi_{k_1})-(N-k_M)\xi_{k_M}(\gamma+\delta\xi_{k_M})-\sum_{i=k_1}^{k_M}\xi_i^2\Big)=0 \tag{6.20}$$

Solving Eq. (6.19) for μ, we obtain the AMLE $\hat{\mu}$ of μ as

$$\hat{\mu}=B-\hat{\sigma}C \tag{6.21}$$

where

$$B=\frac{\Big((k_1-1)\beta X_{(k_1)}+(N-k_M)\delta X_{(k_M)}+\sum_{i=k_1}^{k_M}X_{(i)}\Big)}{m} \tag{6.22}$$

$$C=\frac{(k_1-1)\alpha-(N-k_M)\gamma}{m} \tag{6.23}$$

and

$$m=M+(k_1-1)\beta+(N-k_M)\delta \tag{6.24}$$

Substituting Eq. (6.21) into Eq. (6.20), and solving the quadratic equation, we obtain the AMLE $\hat{\sigma}$ of σ as

$$\hat{\sigma}=\frac{-D+(D^2+4AE)^{\frac{1}{2}}}{2M} \tag{6.25}$$

where

$$D=(k_1-1)\alpha X_{(k_1)}-(N-k_M)\gamma X_{(k_M)}-mBC \tag{6.26}$$

and

$$E=(k_1-1)\beta X_{(k_1)}^2+(N-k_M)\delta X_{(k_M)}^2+\sum_{i=k_1}^{k_M}X_{(i)}^2-mB^2 \tag{6.27}$$

Note that, solving Eq. (6.20) leads to a quadratic equation in σ, which has two roots. However, one of them drops out since $\beta>0$ and $\delta>0$ and, hence $E>0$.

6.2.2 Bilateral CFCR Thresholds

Due to its simple computational model and controlled FAR, the CFAR detection approach is a popular framework used in many methods for ship detection in SAR images. Here, based on the statistical difference between the PUT reflectivity and its surrounding background, we use an SRW with no guard region in order to determine whether or not is a target at

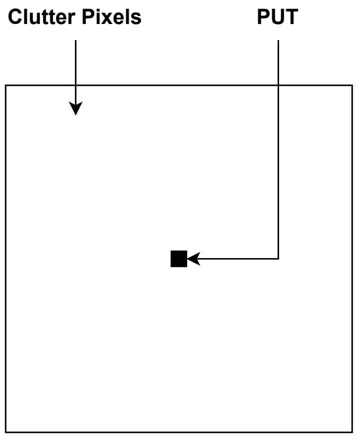

Figure 6.2: SRW of the AML-CFAR detector.

each pixel of the image. Fig. 6.2. shows the adopted SRW. All pixels including the PUT are of size 1×1 each, and the clutter region size should be large enough to estimate the local clutter statistics accurately [95].

Given the drawbacks of the conventional CFAR detectors, the AML-CFAR detector attempts to improve the detection performance of complex sea scenes contaminated by outliers. Outliers are data points that distinguish themselves from the main group of the data by their extreme values. It is worth noting that we used the word outlier to indicate both low and high returns from such a natural sea surface, formed by constructive interference between oceanic scatterers, harbor areas, urban areas, and oil spills. Inspired by the CFAR detection methodology, Fig. 6.3 shows how the AML-CFAR detector mitigates the influence of the outliers on the parameters estimation of the clutter distribution within the SRW. The desired P_{FC_1} and P_{FC_2} would be readily achieved by setting the adaptive threshold T_1 and T_2 such that

$$\begin{aligned} P_{FC_1} &= Pr\{X < T_1 \mid H_h\} \\ P_{FC_2} &= Pr\{X > T_2 \mid H_h\} \end{aligned} \tag{6.28}$$

where H_h designates homogeneous background, and T_1 and T_2 the (P_{FC_1}) and $(1 - P_{FC_2})$ quantiles of the distribution of X, respectively. That is

$$\begin{aligned} T_1 &= F_X^{-1}(P_{FC_1}) \\ T_2 &= F_X^{-1}(1 - P_{FC_2}) \end{aligned} \tag{6.29}$$

where $F_X^{-1}(.)$ is the ICDF of X. For a normally distributed clutter, the thresholds can be

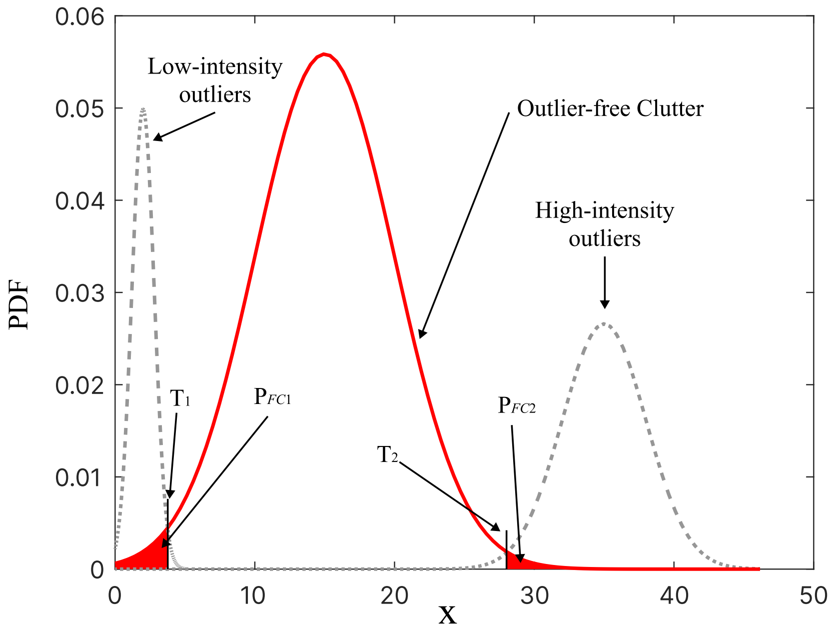

Figure 6.3: Probability density curves of the outlier-free clutter and high/low-intensity outliers, showing the lower and upper probabilities of false censoring.

expressed as

$$\begin{aligned} T_1 &= \hat{\mu}_\mathrm{C} + \alpha_{T_1}\hat{\sigma}_\mathrm{C} \\ T_2 &= \hat{\mu}_\mathrm{C} + \alpha_{T_2}\hat{\sigma}_\mathrm{C} \end{aligned} \tag{6.30}$$

where $\hat{\mu}_\mathrm{C}$ and $\hat{\sigma}_\mathrm{C}$ are the AMLEs of μ_C and σ_C, respectively, with

$$\begin{aligned} \alpha_{T_1} &= \Phi^{-1}(P_{FC_1}) \\ \alpha_{T_2} &= \Phi^{-1}(1 - P_{FC_2}) \end{aligned} \tag{6.31}$$

where $\Phi^{-1}(.)$ is the ICDF of the standard normal distribution.

6.2.3 CFAR Detection Threshold

One of the earliest forms of the CFAR detection approach is the CA-CFAR detector [43]. This latter relies on a simple averaging over the N pixels in the clutter region to estimate the detection threshold. However, this detector performs poorly in heavy-tailed background clutter, which is the case for SAR images. What has instead become more common is the use of statistical distribution models for the sea clutter [41]. We assume that, if the clutter alone is present in the SRW (H_0 hypothesis), then the RV X has a PDF with parameters Θ. In this case, the desired P_{FA} would be readily achieved by setting an adaptive threshold T such that

$$P_{FA} = Pr\left\{X > T \mid H_0\right\} \tag{6.32}$$

where T is the $(1 - P_{FA})$ quantile of the distribution of X. That is

$$T = F_X^{-1}(1 - P_{FA}) \tag{6.33}$$

For a normally distributed clutter, the thresholds can be expressed as

$$T = \hat{\mu}_{\mathrm{D}} + \alpha_T \hat{\sigma}_{\mathrm{D}} \tag{6.34}$$

where $\hat{\mu}_{\mathrm{D}}$ and $\hat{\sigma}_{\mathrm{D}}$ are, respectively, the AMLEs of μ_{D} and σ_{D}, with

$$\alpha_T = \Phi^{-1}(1 - P_{FA}) \tag{6.35}$$

According to the above, the AML-CFAR ship detector can be summarized through the following steps

- Step 1: System Setup
  1. Define the appropriate clutter region size of the SRW.
  2. Set the desired P_{FC_1} and P_{FC_2}.
  3. Set the desired P_{FA}.
- Step 2: Preprocessing
  1. If the SAR image is single look, perform spatial multilook processing by combining (averaging) nonoverlapping image blocks in the intensity domain; otherwise, skip this step.
  2. Transform the SAR intensity data into the log-intensity domain.
- Step 3: Automatic Adaptive Censoring and Detection
  1. Rank in an ascending order the pixels within the SRW.
  2. Use the pixels lying in the interval $]N/4, 3N/4]$ to estimate the initial parameters μ_{C} and σ_{C} through Eqs. (6.21) and (6.25), respectively, and compute the censoring thresholds T_1 and T_2 and their corresponding scale factors through Eqs. (6.30) and (6.31), respectively.
  3. Check if the pixels intensities are lower than T_1 or greater than T_2. If so, the pixels are censored.
  4. Use the remaining pixels to estimate the parameters μ_{D} and σ_{D} through Eqs (6.21) and (6.25), respectively.

5. Label the PUT as a target if the detection threshold given by Eq. (6.34) satisfies Eq. (6.1) for the H_1 hypothesis.
6. Move the SRW by one pixel along the image.
7. Repeat the process from Step 3 until all pixels are depleted.
8. Output the output image and detection results.

6.3 Analysis of the proposed AML-CFAR Detector

6.3.1 Evaluation of the AMLE

As accurate modeling of the statistical SAR image reflectivity distribution plays a significant role in CFAR ship detection, we propose to compare, through MC (Monte Carlo) simulations, both estimation accuracy and detection performances of the AML-CFAR and two MLE based CFAR detectors; namely, the LNTS-CFAR and BTSR-CFAR detectors.

Specifically, for a homogenous and a heterogeneous backgrounds, respectively, we want to evaluate the parameters estimation accuracy involved in the proposed AML-CFAR detector, through a comparison to those used in the LNTS-CFAR and BTSR-CFAR detectors; in regards to the benchmark of the estimators, namely the uncensored MLE [5]. In doing this, we resort to a simulated log-normal sea clutter data. The truncation depth of the LNTS-CFAR detector is set to $t_1 = 1$, while the BTSR-CFAR detector lower truncation depth is set to $t_1 = 2$, along with an adaptive upper trimming depth set to $\gamma = 0.7$. The log-normal sea clutter distribution parameters are set to $\mu = 1.2$ and $\sigma = 0.2$. For each iteration (the number of iterations $N_I = 5000$), the SRW size $N = 41 \times 41$. For comparison purposes, based on a prospection of the structure of several performance metrics reported in the literature, we suggest the use of the RRMSE (Relative Root Mean Square Error) metric. It is defined as [84]

$$\mathrm{RRMSE}_\mu = \left(\frac{1}{N_I} \sum_{i=1}^{N_I} \frac{(\hat{\mu}_i - \mu)}{\mu} \right)^{\frac{1}{2}} \tag{6.36}$$

$$\mathrm{RRMSE}_\sigma = \left(\frac{1}{N_I} \sum_{i=1}^{N_I} \frac{(\hat{\sigma}_i - \sigma)}{\sigma} \right)^{\frac{1}{2}} \tag{6.37}$$

where $\hat{\mu}_i$, $\hat{\sigma}_i$ are, respectively, the estimated values of μ and σ at the i^{th} iteration.

For a homogeneous clutter, Fig. 6.4 shows the plots of the RRMSEs of μ and σ corresponding to each of the estimators-based detectors versus P_{FC_1} and P_{FC_2}. For $P_{FC_1} = P_{FC_2} =$

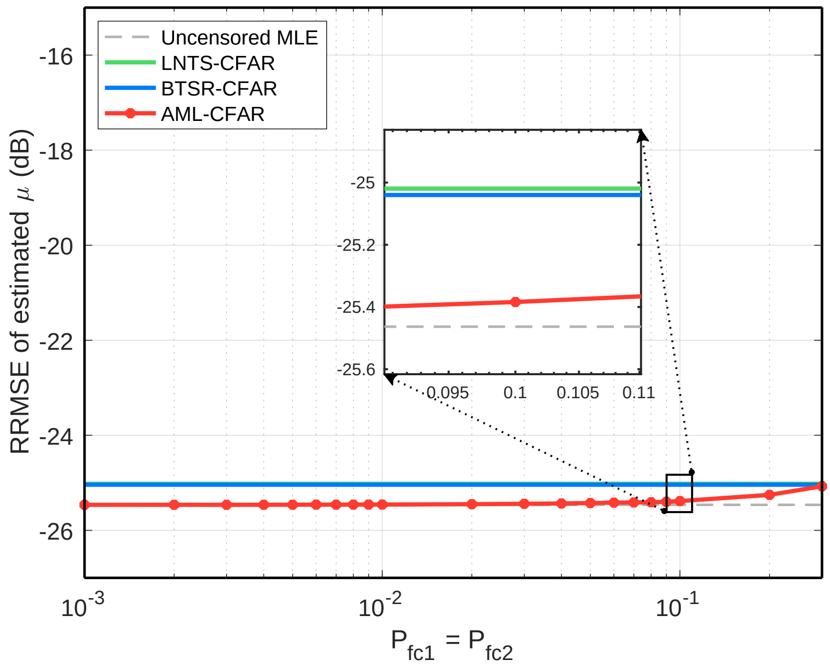

(a)

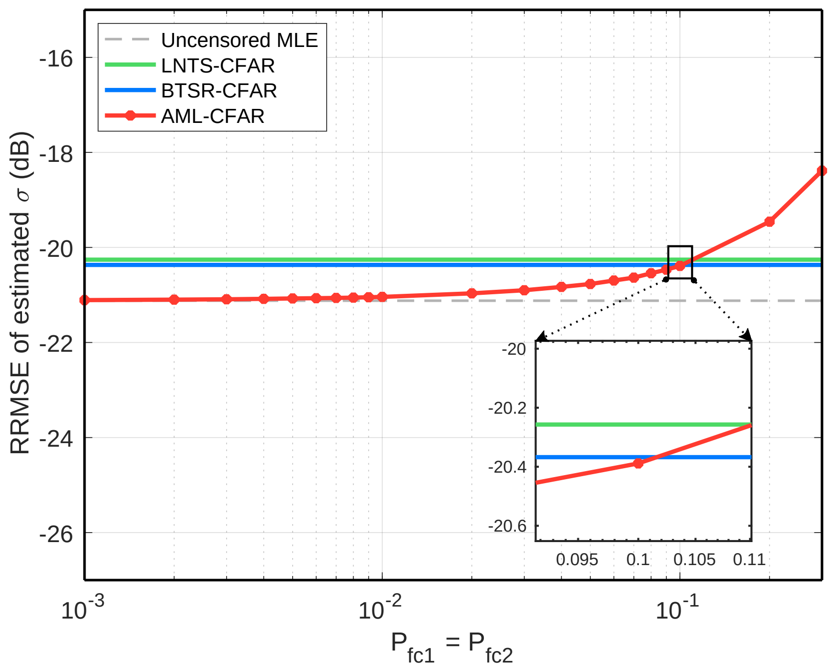

(b)

Figure 6.4: Parameter estimation errors of the LNTS-CFAR, BTSR-CFAR, AML-CFAR detectors and the MLE against P_{FC_1} and P_{FC_2} for a homogeneous log-normal sea clutter; (a) RRMSE of the mean μ (b) RRMSE of the standard deviation σ.

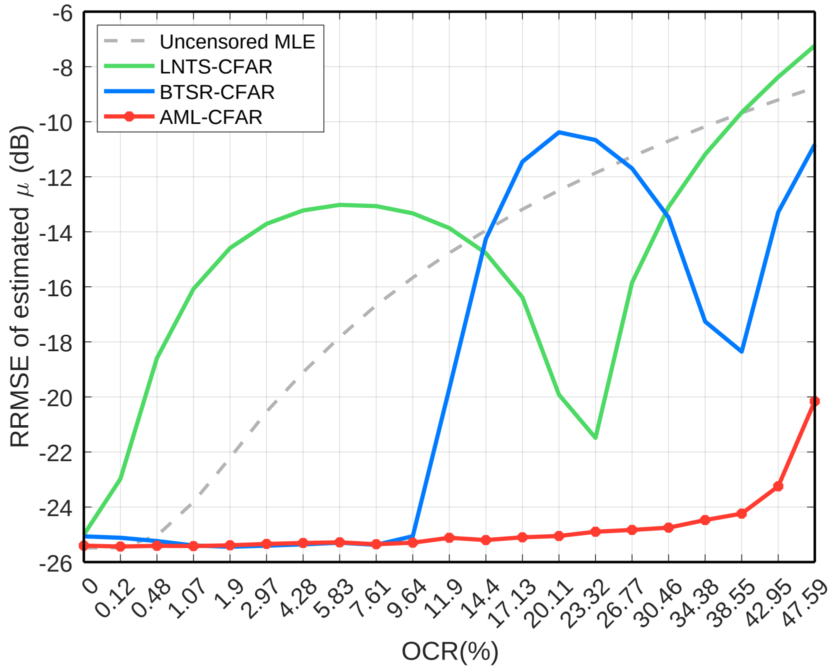

(a)

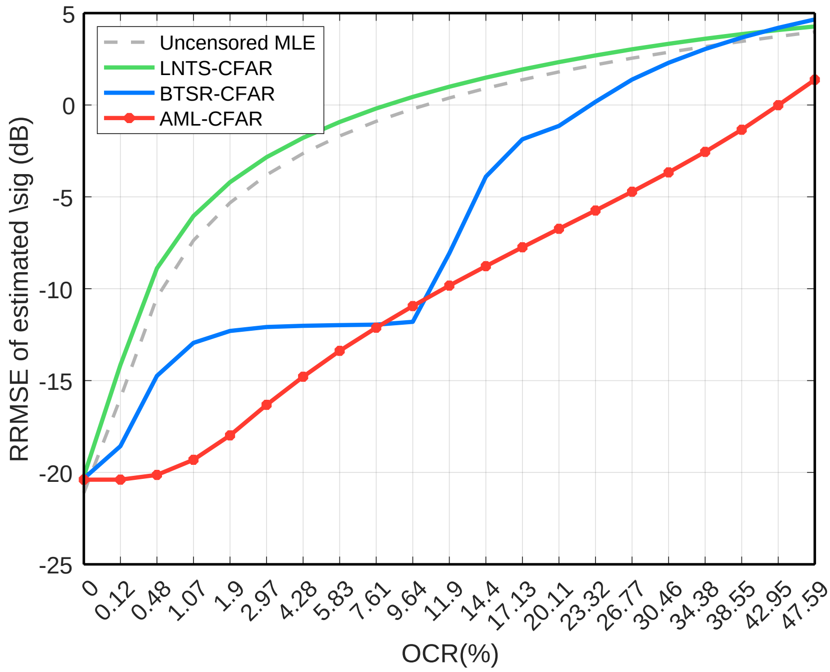

(b)

Figure 6.5: Parameter estimation errors of the LNTS-CFAR, BTSR-CFAR, AML-CFAR detectors and the MLE against P_{FC_1} and P_{FC_2} for a heterogeneous log-normal sea clutter, for $P_{FC_1} = P_{FC_2} = 10^{-1}$; (a) RRMSE of the mean μ (b) RRMSE of the standard deviation σ.

10^{-1}, Fig. 6.4a shows that the RRMSE of μ corresponding to the AML-CFAR detector is nearly equal to that obtained by the uncensored MLE. Although, Fig. 6.4b, the RRMSE of σ corresponding to the AML-CFAR detector departs from that of that obtained by the uncensored MLE, it is better than those obtained by the LNTS-CFAR and BTSR-CFAR detectors. For a heterogeneous sea clutter contaminated with both high and low intensity outliers, Fig. 6.5 shows the P_{FC_1} and P_{FC_2} parameterized plots of the RRMSEs of μ and σ corresponding to each of the estimators-based detectors versus the OCR (Outlier Contamination Ratio). The OCR is defined as the fraction of the number of outliers contaminated data points to the total number of the clutter data points. The intensity values of the high outliers are uniformly distributed between 1.8 and 2.2 times the maximum value of the sea clutter data, and so are the low intensity ones but between 0.1 and 0.3 times the minimum value of the sea clutter data. For $P_{FC_1} = P_{FC_2} = 10^{-1}$, Fig. 6.5a shows that the RRMSEs of μ corresponding to the uncensored MLE and LNTS-CFAR detectors are greatly affected by the presence of the outliers. This is due to the fact that the latter is only suited for upper censoring and the former for a homogeneous clutter. However, the RRMSE of the BTSR-CFAR detector overlaps that of the AML-CFAR detector up to $OCR \approx 10\%$. It is worth noting that the RRMSE curve of the proposed AMLE does not deviate much (RRMSE $\approx -26dB$ up to $OCR \approx 40\%$) from that obtained for the homogeneous case. Finally, Fig. 6.5b shows that the RRMSE curve of σ corresponding to the AML-CFAR detector, greatly departs from that of the homogeneous case, but remains better than those obtained by the LNTS-CFAR and BTSR-CFAR detectors.

CFAR property

Always for a log-normal sea clutter, we investigate the CFAR property of the AML-CFAR detector along with the LN-CFAR, LMM-CFAR, LNTS-CFAR and BTSR-CFAR detectors. In the lack of analytic expressions of the P_{FA}, recent studies show that if the derived detector satisfies some conditions, then it can be said to have the CFAR property [71]. Here, as shown in Fig. 6.6, we focus on the invariance of the experimental P_{FA} versus the design P_{FA} when either μ or σ varies. The basic simulation scenario is a 1024×1024 image, contaminated by a log-normal clutter and an SRW having the same characteristics as above. Note that, as stated in [42, 83, 84], we choose three log-normal components for the LMM-CFAR detector. The remaining detectors are set as before. In Fig. 6.6a, we consider $\mu = 0.2$, 1.2 and 3 and $\sigma = 0.2$. This figure clearly shows that there is a complete overlap between all curves regardless of the values of the design P_{FA} and μ. As a result, all detectors are CFAR with respect to the design P_{FA} and μ. In Fig. 6.6b, we consider $\sigma = 0.2$, 1.2 and 3 and $\mu = 1.2$. Here, the curves clearly show that, the most accurate fits to the design P_{FA} are achieved by the AML-CFAR, LMM-CFAR, LNTS-CFAR and LN-CFAR detectors. However, performance degradation is observed for the BTSR-CFAR detector, since it is based on the VI (Variability Index), which is not suited when the clutter gets spiker, i.e., $\sigma > 1$. Consequently, the AML-CFAR detector is CFAR irrespective of μ and σ.

6.3.2 Experimental Results with Simulated SAR Images

Now we should evaluate qualitatively and quantitatively the detection performances of the proposed detector versus the detectors cited above on simulated SAR images. Before proceeding any further, let us introduce the expressions of the P_D and P_{FA}, as

$$P_D = \frac{N_{TD}}{N_{GT}} \tag{6.38}$$

where N_{TD} is the number of true detections in the SAR image and N_{GT} the number of target pixels within its corresponding GT image,

and

$$P_{FA} = \frac{N_{FA}}{mn - N_{GT}} \tag{6.39}$$

where N_{FA} is the number of false alarms, and m and n the dimensions of the SAR image.

It is worth noting that the MC simulations were carried on a Laptop powered by an Intel Core 7 CPU, with a speed of up to 2.8 GHz and a RAM of 16 GB. Fig. 6.7 shows the two simulated SAR images each of size 512×512 pixels which are used to evaluate the performances of the AML-CFAR detector in complex sea scenarios. Fig. 6.7a represents a multiple target scenario for which the simulated sea clutter is characterized by the log-normal distribution with $\mu_{\text{Sea}} = 3$ and $\sigma_{\text{Sea}} = 0.2$. The image contains 37 ship targets, their intensity values are Weibull distributed with shape and scale parameters $\alpha_{Target} = 6$ and $\beta_{Target} = 124.40$, respectively. The SCR (Signal to Clutter Ratio) has been evaluated through Eq. (6.40) to be SCR = 15dB. They are densely clustered in the center of the image. Similarly, for the same characteristics as for the previous image, Fig. 6.7b includes the densely distributed ship target areas and breakwaters as marked by the red solid ellipse, a few ships, and the ship-oil-mixed area marked by the red solid rectangle. The intensity values of the ship targets are also Weibull distributed with $\alpha_{Target} = 6$ and $\beta_{Target} = 124.40$ (SCR = 15 dB). The land/breakwater and the spilled-oil pixels are log-normal distributed with $\sigma_{\text{Land}} = 0.3$

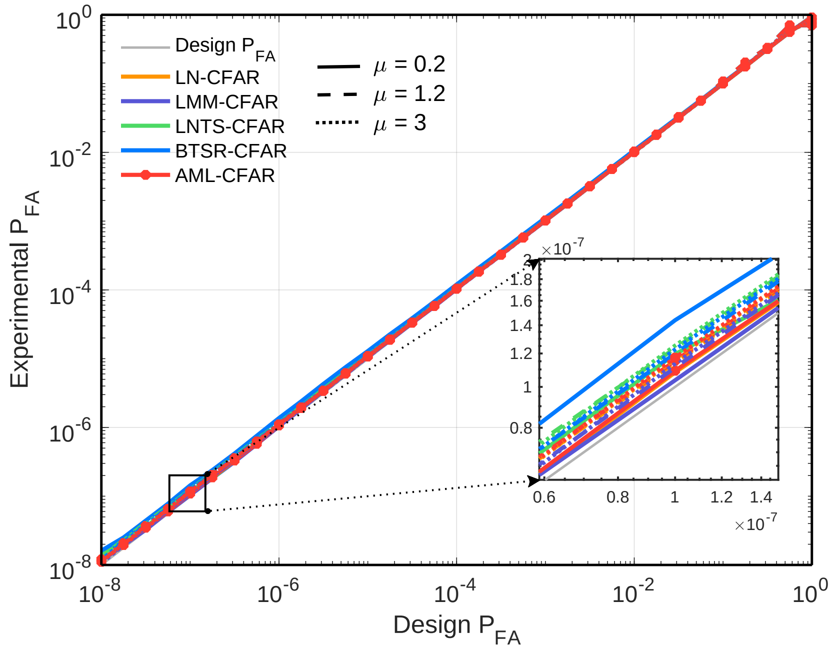

(a)

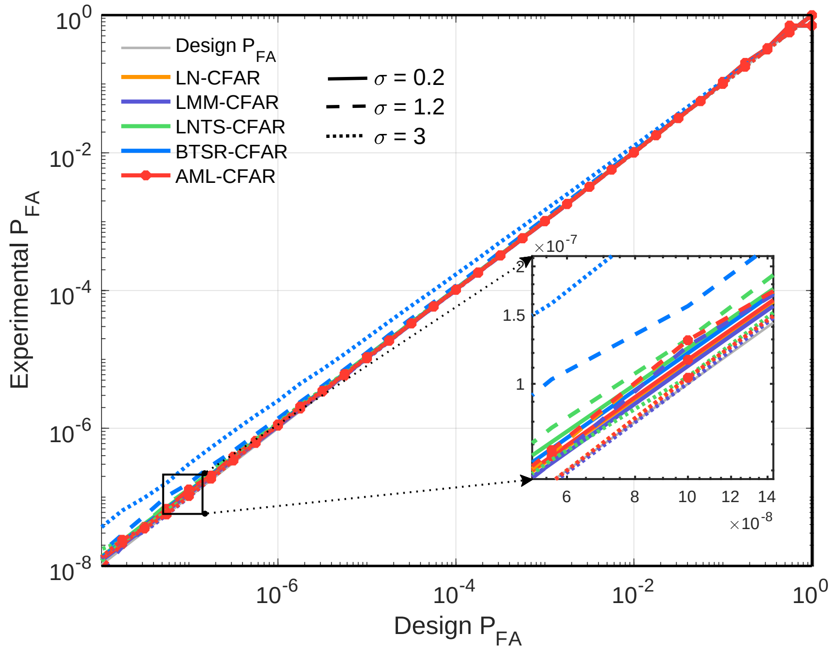

(b)

Figure 6.6: Experimental P_{FA} versus design P_{FA}; (a) μ as a parameter (b) σ as a parameter.

and $\mu_{\text{Land}} = 4.10$, and $\sigma_{\text{Oil}} = 0.1$ and $\mu_{\text{Oil}} = 1.87$, respectively. Their respective CCRs (Clutter to Clutter Ratio) have been evaluated through Eq. (6.41) to be CCR = 10dB and -10dB.

$$SCR = \frac{E\left[S^2_{\text{Target}}\right]}{E\left[Y^2_{\text{Sea}} \mid H_0\right]} = \frac{\alpha^2_{\text{Target}}\Gamma(1 + \frac{2}{\beta_{\text{Target}}})}{\exp(2\mu_{\text{Sea}} + 2\sigma^2_{\text{Sea}})} \tag{6.40}$$

$$CCR = \frac{E\left[Y^2_{\text{Land/Oil}} \mid H_0\right]}{E\left[Y^2_{\text{Sea}} \mid H_0\right]} = \frac{\exp(2\mu_{\text{Land/Oil}} + 2\sigma^2_{\text{Land/Oil}})}{\exp(2\mu_{\text{Sea}} + 2\sigma^2_{\text{Sea}})} \tag{6.41}$$

Figs. 6.8c–g. show the detection results of the proposed detector versus the detectors cited above, for $P_{FA} = 10^{-5}$. Note that we have to add a 21×21 guard region to the LN-CFAR and LMM-CFAR detectors. For a simulated multiple target scenario, i.e., sea and ships of Fig. 6.7a, Fig. 6.8 shows that the LN-CFAR and LMM-CFAR detectors are useless due to the lack of censoring mechanisms, the BTSR-CFAR misses some targets, while the LNTS-CFAR and the AML-CFAR detectors identify all ship targets.

The detection performance of the AML-CFAR detector is further verified through the simulated heterogeneous scenario, i.e., sea, ships, breakwater and ship-oil-mixed area of Fig. 6.7b. Figs. 6.9c–g show the outcome images of all detectors. In contrast to the previous scenario, here, while the proposed detector identifies all ship targets; according to their respective performances, the LN-CFAR, LMM-CFAR, LNTS-CFAR and BTSR-CFAR detectors, miss more or less targets (red circles).

Table 6.1 summarizes the P_D, P_{FA} and CPU time of all outcome images of Figs. 6.8c–g and Figs. 6.9c–g. To quantify the P_D and P_{FA} of all detectors, we resort to the images of Figs. 6.7a and b and their corresponding GT images shown in Figs. 6.8b and 6.9b. By CPU time, we merely intend to estimate and compare the consumption time of all detectors via

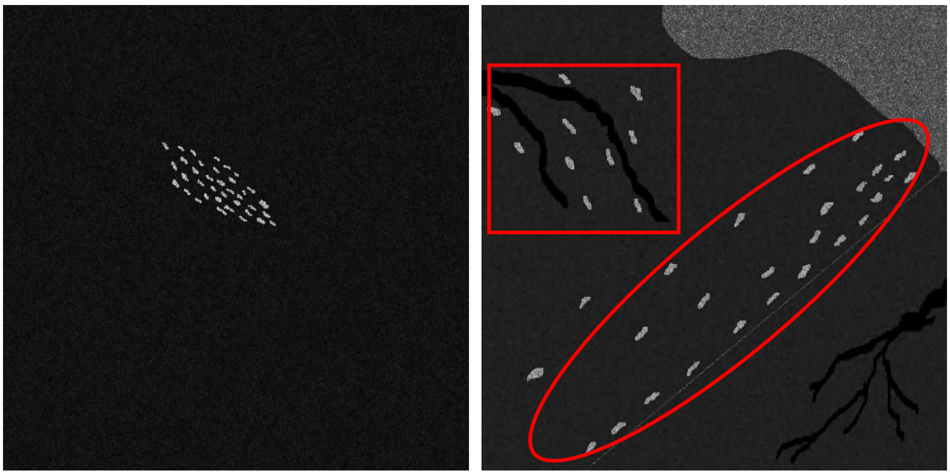

(a) (b)

Figure 6.7: Simulated SAR images, (a) Multiple target scenario and (b) Heterogeneous scenario.

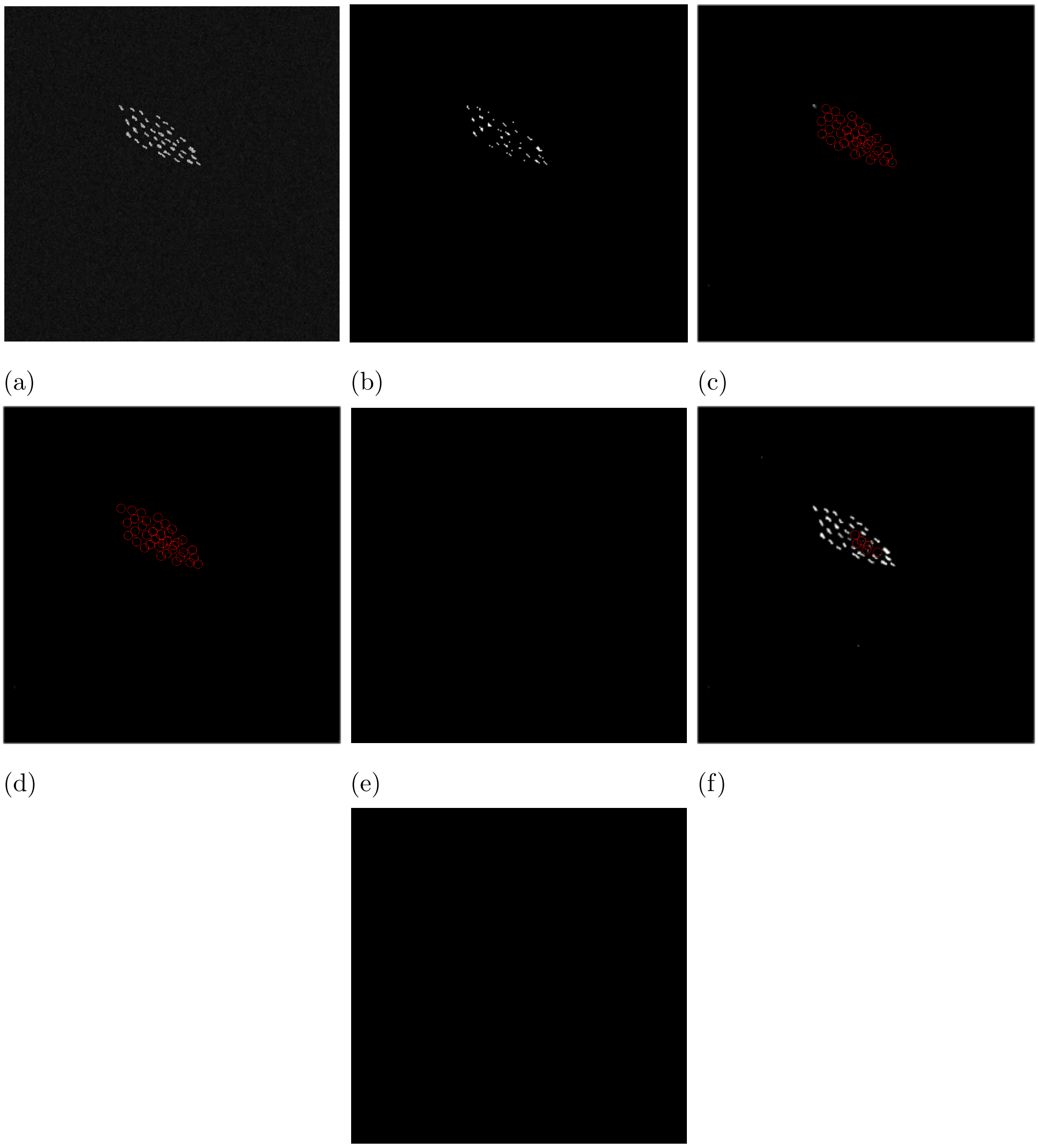

(a) (b) (c) (d) (e) (f) (g)

Figure 6.8: Qualitative detection performances of all detectors for a simulated multiple target scenario; (a) Simulated SAR image, (b) Corresponding GT image, (c) LN-CFAR detector, (d) LMM-CFAR detector, (e) LNTS-CFAR detector, (f) BTSR-CFAR detector and (g) AML-CFAR detector (Red circles designate missing targets).

the "tic-toc" Matlab built-in function, i.e., the time between the start and the completion of a given detector's routine. Inspection of this table shows that, the AML-CFAR is the only detector which achieves $P_D > 0.9$ and realistic scores in terms of $P_{FA} = 1.53 \times 10^{-5}$ and 109.67×10^{-5} and CPU time $= 16.74$ s and 15.71 s for both simulated scenarios of Fig. 6.7.

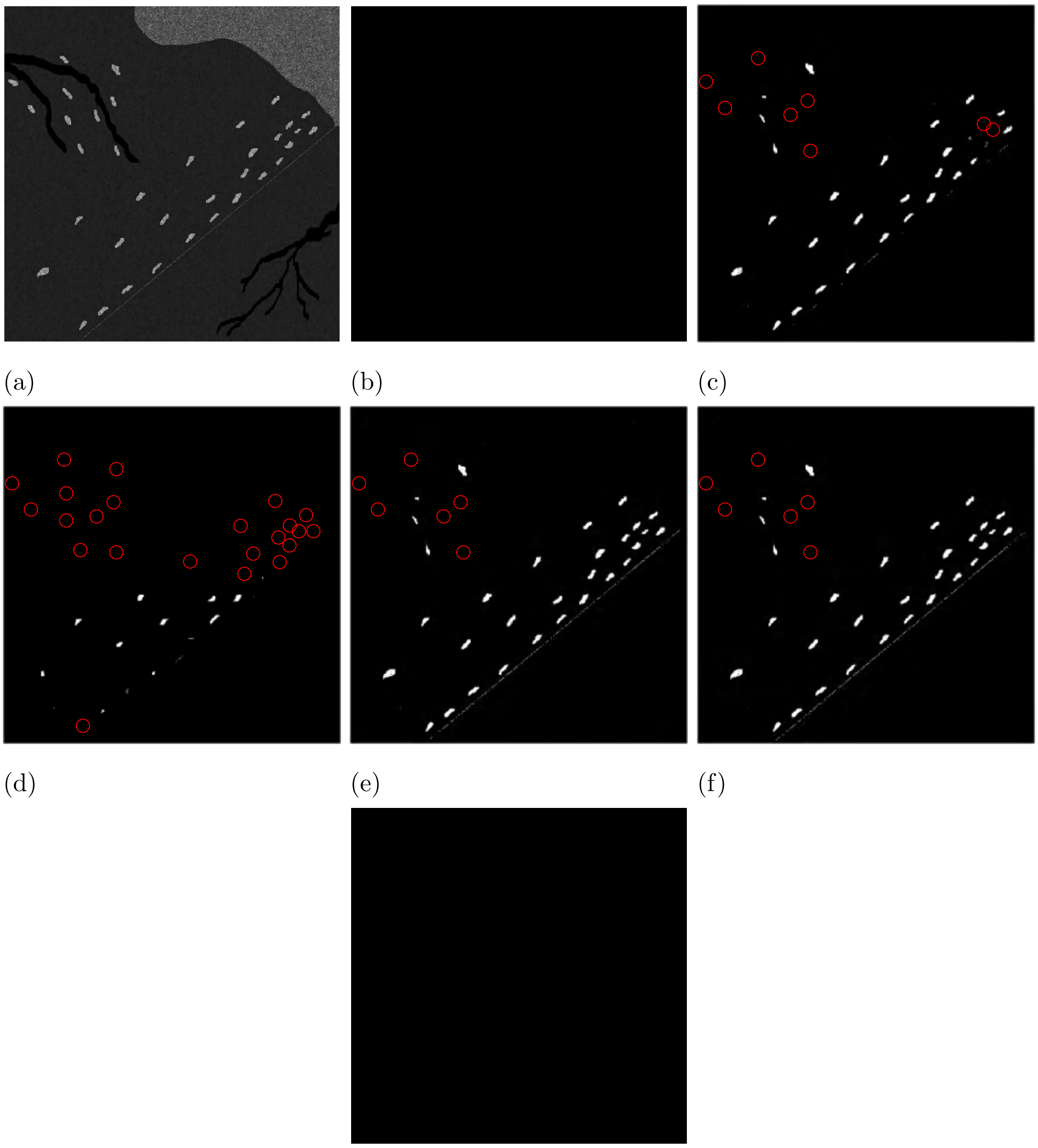

(a) (b) (c)

(d) (e) (f)

(g)

Figure 6.9: Qualitative detection performances of all detectors for a simulated heterogeneous scenario; (a) Simulated SAR image, (b) Corresponding GT image, (c) LN-CFAR detector, (d) LMM-CFAR detector, (e) LNTS-CFAR detector, (f) BTSR-CFAR detector and (g) AML-CFAR detector (Red circles designate missing targets).

Then comes the BTSR-CFAR detector with $P_D = 0.79$ and 0.77 and also reasonable scores in terms of $P_{FA} = 1.53 \times 10^{-5}$ and 96.15×10^{-5} and CPU time = 18.57 s and 18.23 s. The good performances of both detectors are owed not only to their respective parameter estimators and detection thresholds but also to their bilateral censoring strategies. Note though the

Table 6.1: CFAR Detection metrics of the detectors outcome images of Figs. 6.8 and 6.9 (Results of the proposed detector in bold).

Image	Detector	N_{TD}/N_{GT}	P_D	$P_{FA} \times 10^{-5}$	CPU time (s)
Fig. 6.8 / Fig. 6.9	LN-CFAR	14/1037	0.01	0.76	2.77
		2144/3196	0.67	12.35	2.87
	LMM-CFAR	0/1037	0	0.76	62.07
		509/3196	0.15	3.08	196.06
	LNTS-CFAR	1022/1037	0.98	0.76	6.39
		2479/3196	0.77	88.43	6.07
	BTSR-CFAR	823/1037	0.79	1.53	18.57
		2492/3196	0.77	96.15	18.23
	AML-CFAR	**1004/1037**	**0.96**	**1.53**	**16.74**
		3085/3196	**0.96**	**109.67**	**15.71**

ascendancy of the AML-CFAR detector over the BTSR-CFAR detector in the heterogeneous scenario which is due to its effective bilateral censoring. For its part, the LNTS-CFAR detector achieves $P_D = 0.98$ and 0.77, $P_{FA} = 0.76 \times 10^{-5}$ and 88.43×10^{-5} and CPU time = 6.39 s and 6.07 s. Although the performances of this detector are very challenging in the multiple target scenario, they are impacted by its one-side censoring when other heterogeneities are present in the SRW. Finally, the LMM-CFAR and LN-CFAR detectors seem to be inoperative for these examples of simulated SAR images.

According to the radar literature, the ROC curve is an interesting binary classifier to assess the performances of a detector. Figs. 6.10a–b shows the curves of P_D versus P_{FA}, i.e., ROC curves of all detectors for the simulated SAR image of Figs. 6.7a–b. Unfortunately, as show in Fig. 6.10a, the LNTS-CFAR detector outperforms all detectors and particularly the AML-CFAR detector. Although not shown, the AML-CFAR detector has similar performances as the LNTS-CFAR detector for SCR $\geq$ 20dB. In contrary, Fig. 6.10b shows that the AML-CFAR detector outperforms all detectors. Here also, although not shown, this remains true for all values of SCR.

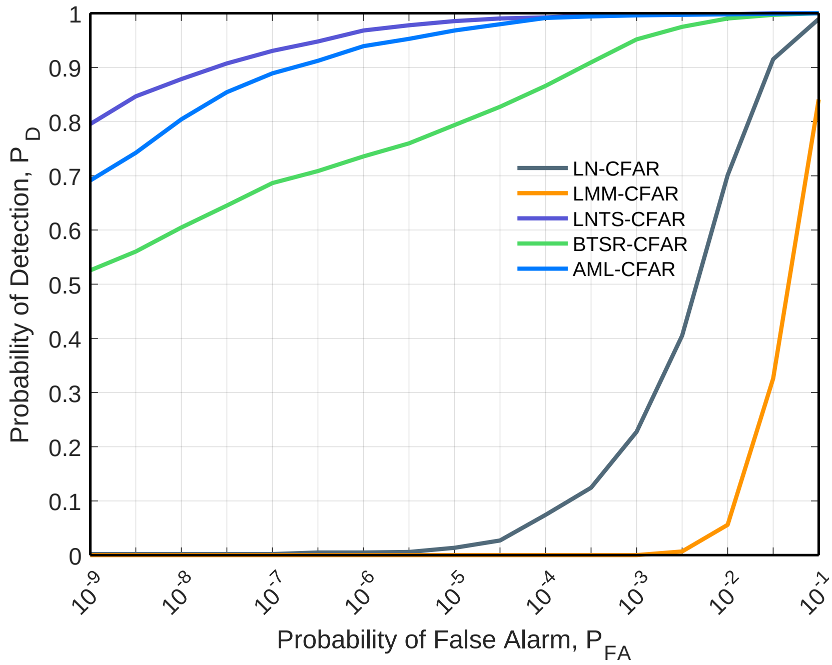

(a)

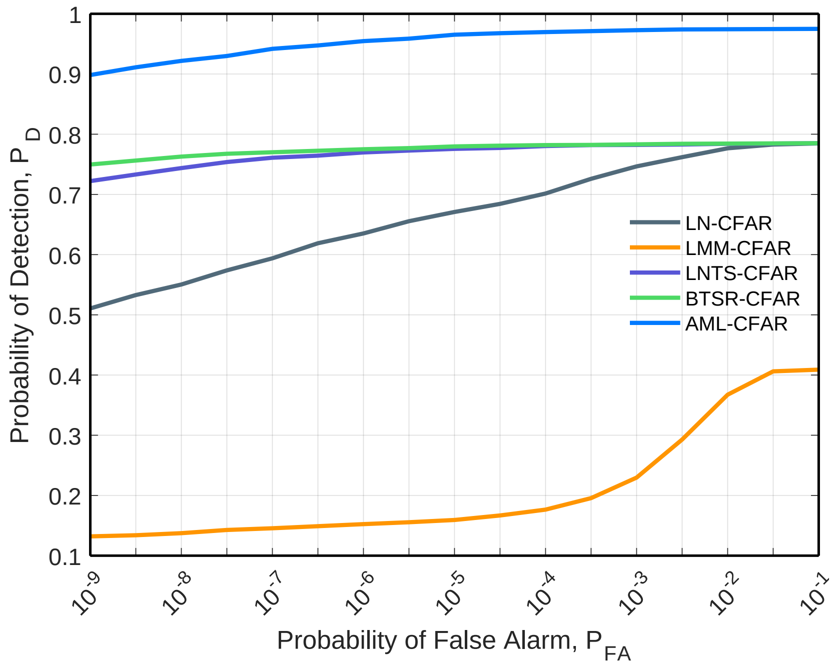

(b)

Figure 6.10: ROC curves of all detectors for the simulated SAR images of Figs. 6.7a–b.

6.3.3 Experimental Results with Real SAR images

In addition to the simulated SAR images, the performance of the proposed AML-CFAR detector is also assessed on the three real SAR images of Figs. 6.11a–c. Fig. 6.11a has been

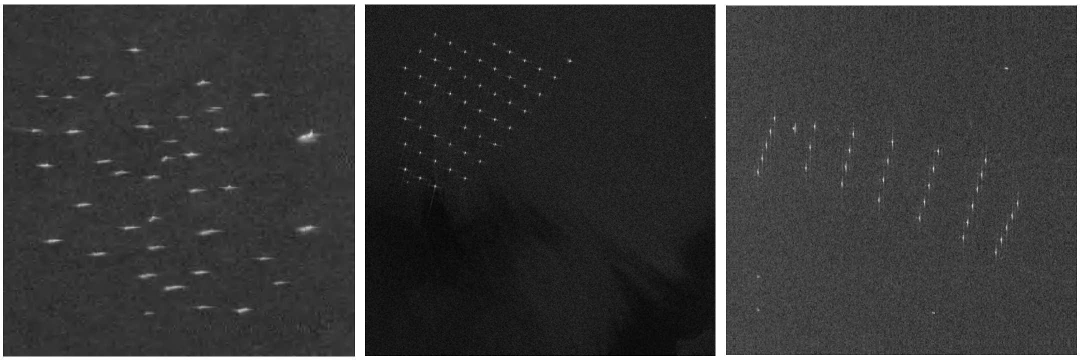

(a) (b) (c)

Figure 6.11: Real SAR images. (a) 571 × 575 TerraSAR-X SAR image, (b) 1000 × 1000 ALOS-2 SAR image, (c) 1037 × 1612 Sentinel-1 image.

Table 6.2: CFAR Detection metrics of the detectors outcome images of Figs. 6.12, 6.13 and 6.14 (Results of the proposed detector in bold).

Image	Detector	N_{TD}/N_{GT}	P_D	$P_{FA} \times 10^{-5}$	CPU time (s)
Fig. 6.12 / Fig. 6.13 / Fig. 6.14	LN-CFAR	879/1065	0.82	26.00	1.15
		576/716	0.80	2.82	3.41
		782/928	0.84	7.44	5.53
	LMM-CFAR	370/1065	0.34	21.10	25.10
		143/716	0.19	2.82	69.62
		460/928	0.49	4.08	104.26
	LNTS-CFAR	946/1065	0.88	1.24	2.19
		589/716	0.82	1.21	6.81
		786/928	0.84	3.36	11.70
	BTSR-CFAR	994/1065	0.93	3.72	5.86
		640/716	0.89	1.61	18.50
		815/928	0.87	3.84	30.86
	AML-CFAR	**1063/1065**	**0.99**	**16.10**	**4.93**
		690/716	**0.95**	**2.01**	**15.79**
		883/928	**0.96**	**6.72**	**26.00**

produced by the TerraSAR-X [86], Fig. 6.11b by ALOS-2 [96] and Fig. 6.11c by the Sentinel-1 [87]. Recall that these images have been acquired, respectively, by the StripMap mode, on September 14, 2014, over China (Longitude E119 and Latitude N37), the StripMap mode,

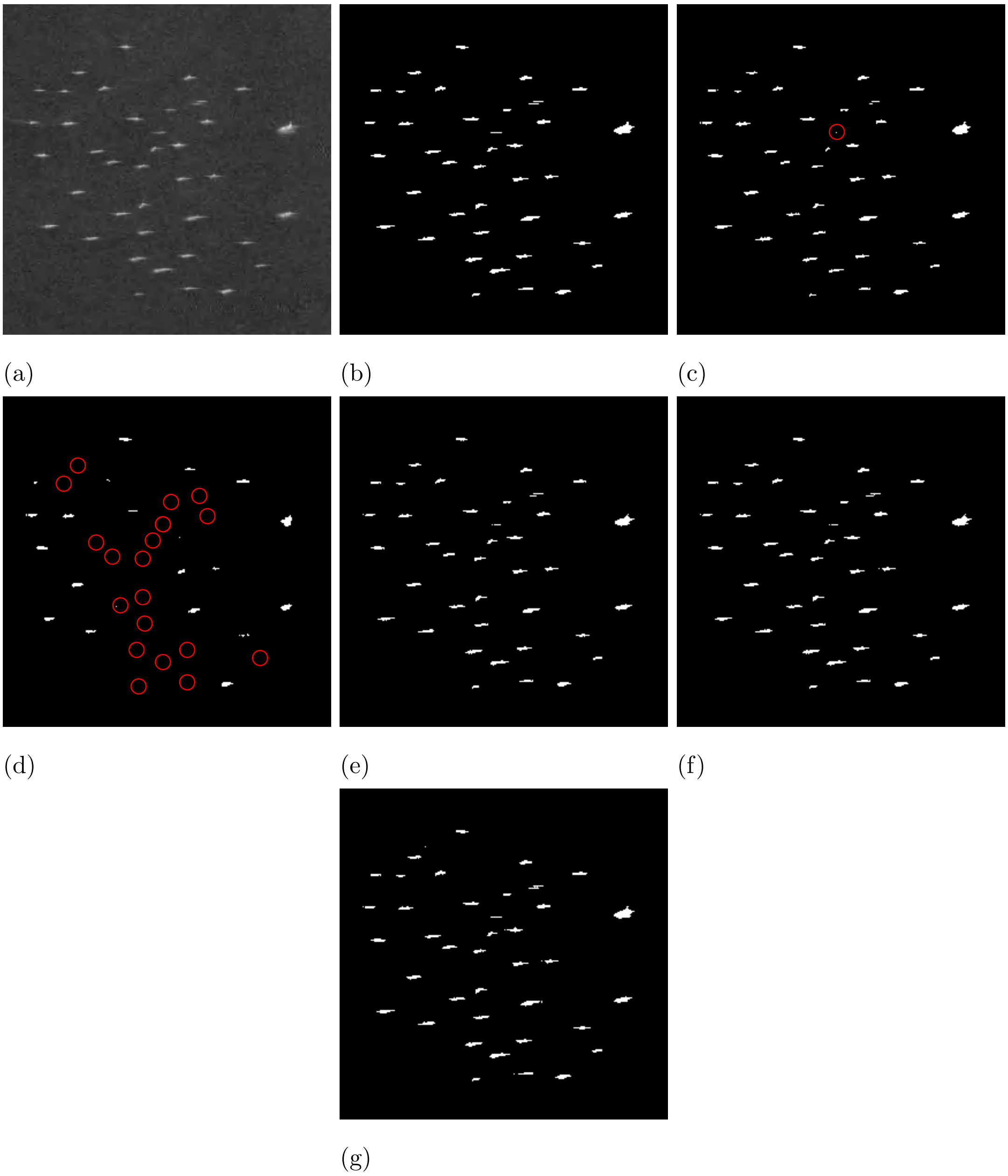

Figure 6.12: Qualitative detection performances of all detectors for a real ship densely distributed area scenario; (a) Real SAR image, (b) Corresponding GT image, (c) LN-CFAR detector, (d) LMM-CFAR detector, (e) LNTS-CFAR detector, (f) BTSR-CFAR detector and (g) AML-CFAR detector (Red circles designate missing targets).

on March 5, 2015, over Denmark (Longitude E12 and Latitude N55) and the Interferometric Wide mode on September 20, 2022, over China (Longitude E116 and Latitude N23).

To alleviate the spatial dependence and increase the SCR, we start by averaging non-overlapping 2×2 pixel blocks (multilooking) on the real SAR images of Figs. 6.11a–c, resulting in 285×287, 500×500, 518×806 SAR images, respectively. Note that here also, we have to add a 21×21 guard region to the LN-CFAR and LMM-CFAR detectors. As expected, the proposed AML-CFAR detector and, to a lesser degree, the BTSR-CFAR, LNTS-CFAR and LN-CFAR detectors are robust as they produce images with all ship targets with only some

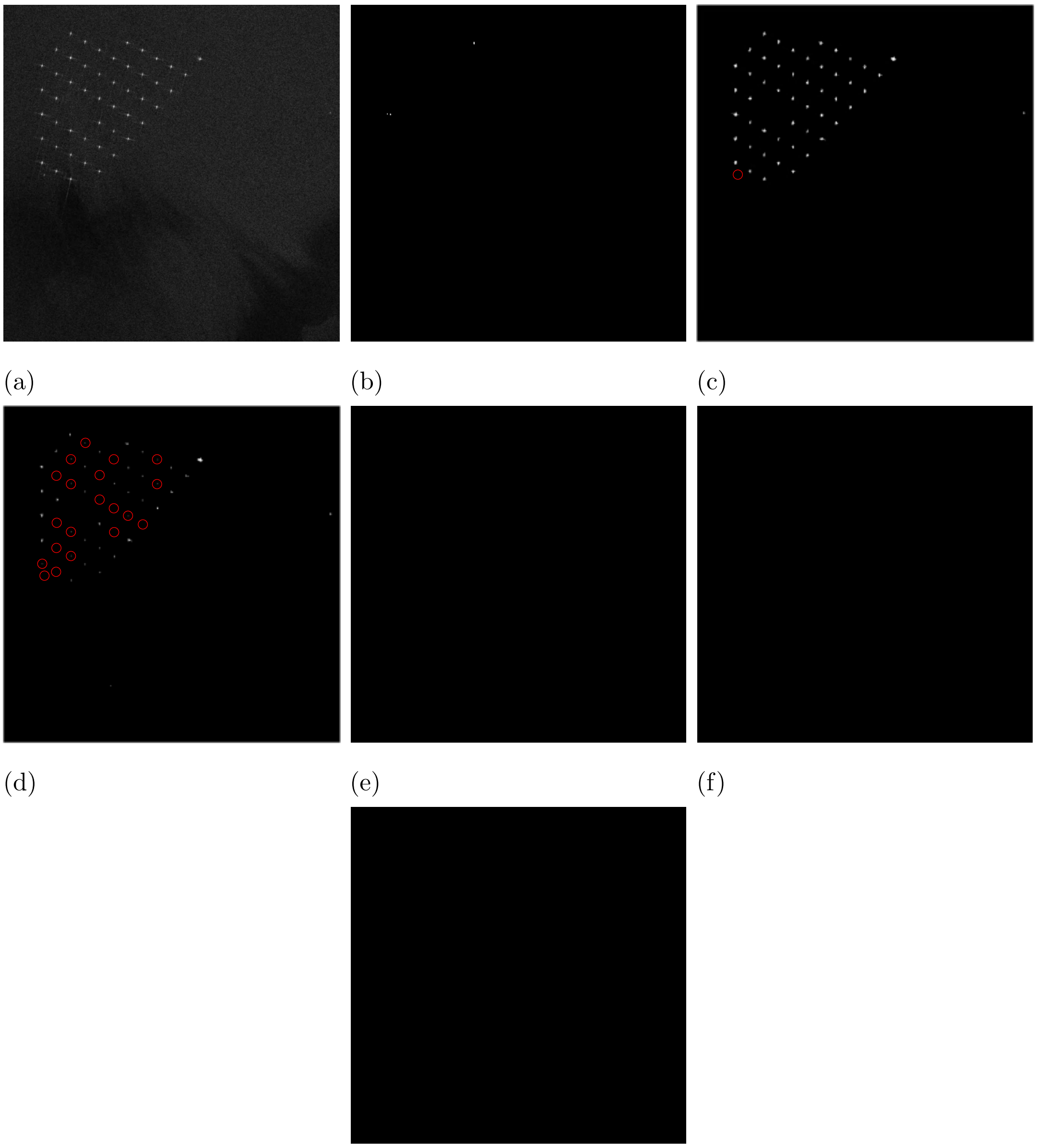

(a) (b) (c)

(d) (e) (f)

(g)

Figure 6.13: Qualitative detection performances of all detectors for a real ship densely distributed area scenario; (a) Real SAR image, (b) Corresponding GT image, (c) LN-CFAR detector, (d) LMM-CFAR detector, (e) LNTS-CFAR detector, (f) BTSR-CFAR detector and (g) AML-CFAR detector (Red circles designate missing targets).

missing pixels. However, having missed quite a lot of ship targets, the LMM-CFAR detector seems to be totally unsuited for the simulated and real SAR images under investigation.

Table 6.2 also summarizes the P_D, P_{FA} and CPU time of all outcome images of Figs. 6.12c–g, Figs. 6.13c–g and Figs. 6.14c–g. Here, to quantify the P_D and P_{FA} of all detectors, we re-

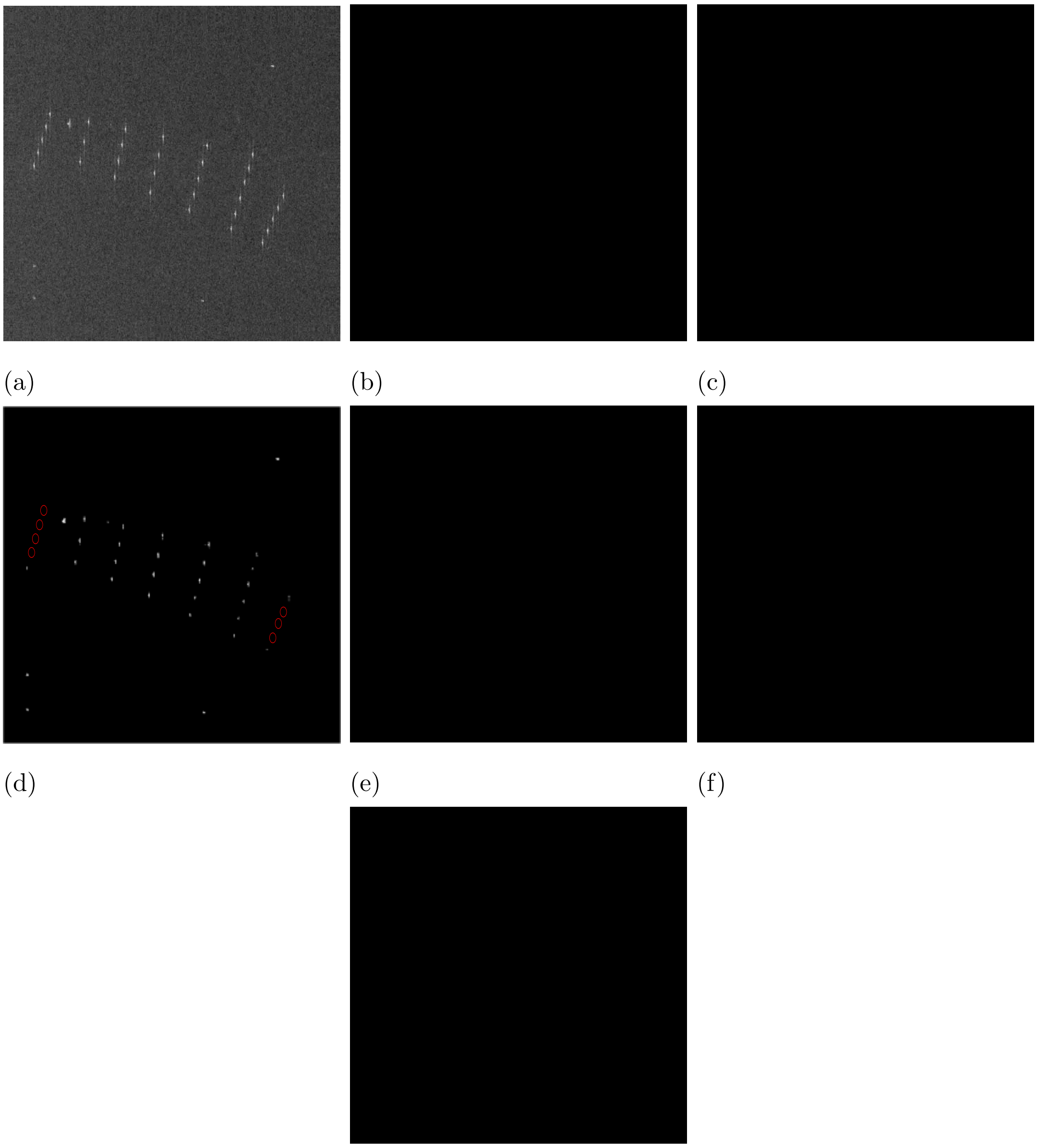

(a) (b) (c)

(d) (e) (f)

(g)

Figure 6.14: Qualitative detection performances of all detectors for a real ship densely distributed area scenario; (a) Real SAR image, (b) Corresponding GT image, (c) LN-CFAR detector, (d) LMM-CFAR detector, (e) LNTS-CFAR detector, (f) BTSR-CFAR detector and (g) AML-CFAR detector (Red circles designate missing targets).

sort to the images of Figs. 6.11a–c and their corresponding GT images shown in Figs. 6.12b, 6.13b and 6.14b. This table shows that the AML-CFAR is the only detector which achieves $P_D > 0.9$ and realistic scores in terms of red$P_{FA} = 16.10 \times 10^{-5}$, 2.01×10^{-5} and 6.72×10^{-5}, and CPU time = 4.93 s, 15.79 s and 26.00 s. Then comes the BTSR-CFAR detector with $P_D > 0.85$ and reasonable scores in terms of P_{FA} and CPU time. The LNTS-CFAR and LN-

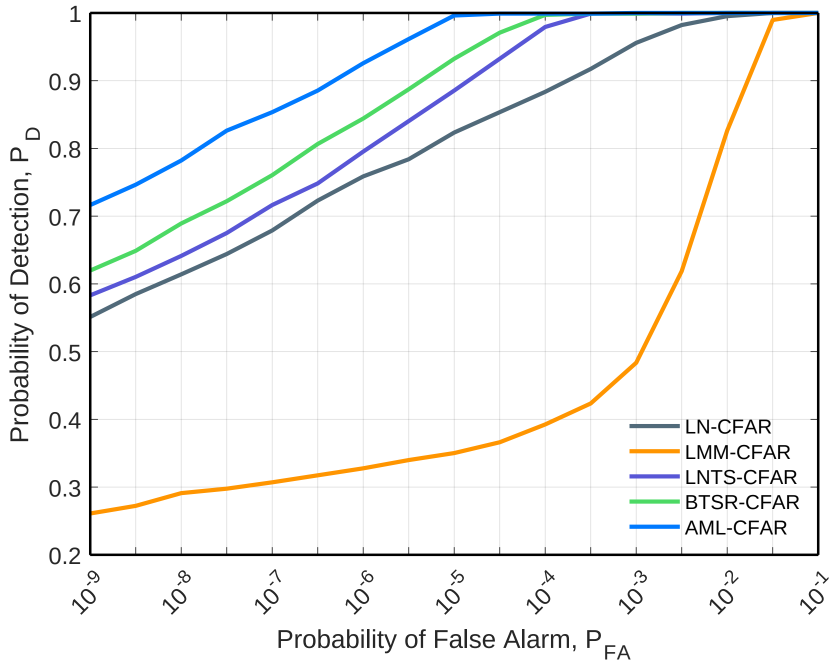

(a)

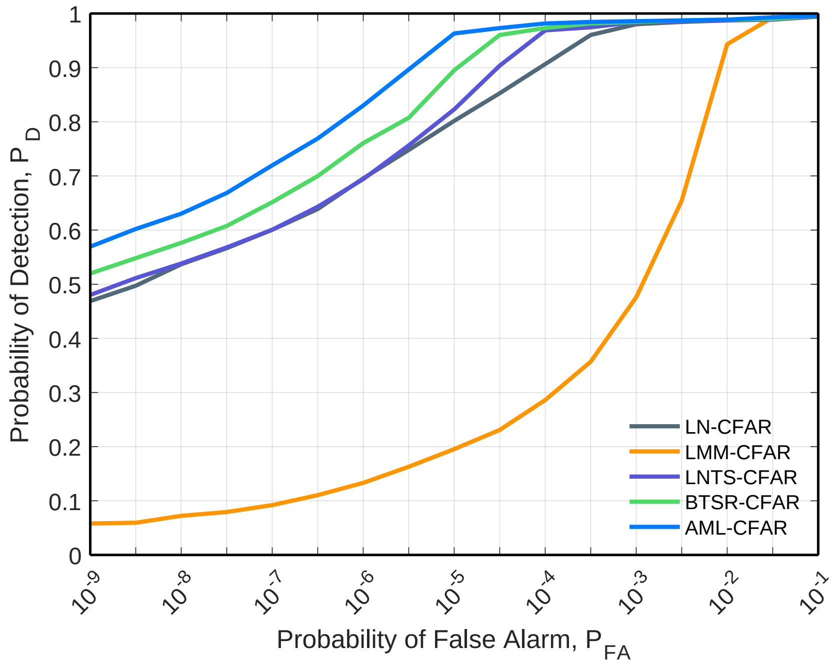

(b)

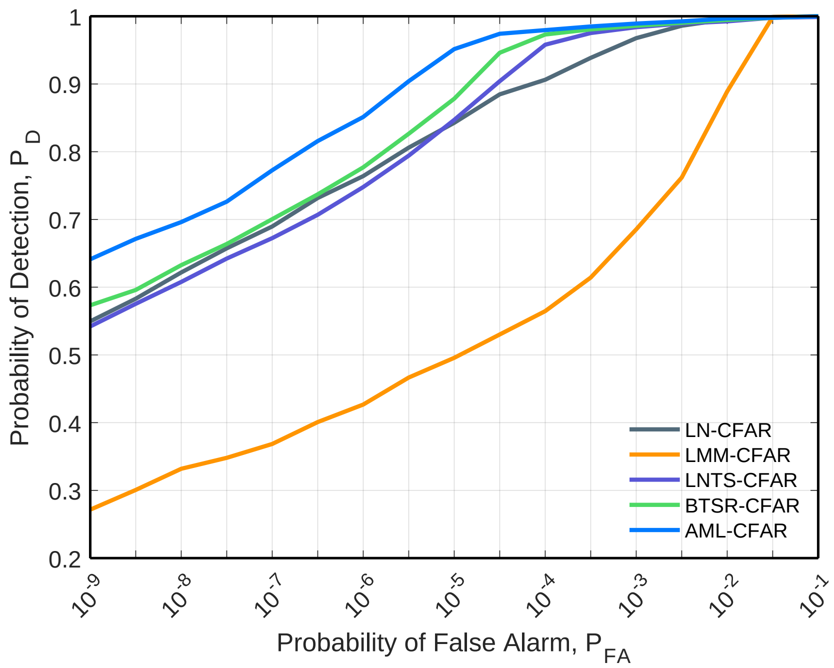

(c)

Figure 6.15: ROC curves of all detectors for the real SAR images of Figs. 6.11a–c.

CFAR detectors also achieve interesting scores in terms of $P_D > 0.80$, P_{FA} and CPU time. The LN-CFAR detector which does not work for the simulated SAR images, seems to catch up more or less with the previous detectors in terms P_D. Finally, the LMM-CFAR does not show any improvement with respect to the simulated SAR images.

Dealing always with the case of the real SAR images of Figs. 6.11a–c, Fig. 6.15 shows the curves of P_D versus P_{FA}, i.e., ROC curves, of all detectors. It is clear that the AML-CFAR detector exhibits the best binary classification.

6.4 Conclusion

In this chapter, we analyzed the censoring and detection algorithms of the AML-CFAR detector for complex scenes of Log-normal sea clutter in SAR imagery without any prior knowledge of the presence or not of a clutter edge and/or interfering targets in the sliding window. In doing this, we first discussed the derivation of the closed-form expressions of the censored normal distribution parameters using AMLEs and described the automatic censoring algorithm. Then, we validated the CFAR property of the AML-CFAR detector through extensive MC simulations. Finally, we analyzed and evaluated, through simulated and real SAR images, the detection performances of the AML-CFAR detector in a log-normal sea clutter when no prior knowledge is made available about the number of interfering targets and/or any other sea clutter heterogeneities, such as targets, off-shore oil-spilled sea areas and land. For a series of scenarios, we showed, via experimental results, that the proposed CFAR detector is efficient on both simulated SAR and real SAR images. That is, the AML-CFAR ship detector acquires a fair P_{FA} regulation, a high detection performance and a fair CPU processing time with regard to the challenging state-of-the-art detectors, and particularly the LNTS-CFAR and BTSR-CFAR detectors.

,

Chapter 7

Conclusions and perspectives

Summary

In this last chapter, we recall the essence of this thesis, then we discuss our contributions including the main results. Lastly, we present potential viewpoints and ideas for further research work.

7.1 Summary of the main results

Ship detection is considered as one of the most complex problems in remote sensing. The continuous evolution of radar systems and the diversity of acquisition modes have made this task very difficult. This is the reason why several scientific works propose methodological approaches to try to solve this problem. Since the acquisition of radar images, various researchers have taken advantage of this progress to exploit them in the framework of this discipline. With the openings on shape recognition and artificial intelligence. Nevertheless, most of the methods propose recognition processes for a defined application and for a type of images. Throughout this work, we proposed innovative methods to improve the recognition process by taking into account not only the accuracy of the methods but also the computation time. In this context, several advances have been noted through the work presented in Chapters 4, 5 and 6. The primary goal of this work was to investigate the behavior of some CFAR detectors, as well as our new suggested ones, in complex scenarios of sea clutter in SAR images.

Parameter estimation and censoring are both important aspects in CFAR to design or develop a maritime radar so that it can detect with high accuracy the ship targets and adjust the false alarm rates in SAR imagery at any time and under all adverse weather conditions. Parameter estimation refers to the process of estimating the statistical parameters of the noise in the system, such as its mean and variance. Censoring, on the other hand, refers to the process of removing or censoring data points that are likely to be associated with the target signal.

In the first contribution, we considered the QM-CFAR detector in the case of a non-stationary Weibull clutter with the presence or not of interfering targets, the QM and the MLE were concomitantly used to allow the proposed detector to perform robustly in multiple target situations with a *priori* unknown Weibull parameters. By that means, we first ranked order the reference samples to select quantile information that shares the same clutter parameters as the CUT and eliminate any outliers within the data. Then, we resorted to the QM and the MLE to get the parameters. Finally, we carried out target decision-making. The subsequent CFAR detection threshold allowed then fixed censoring of the upper end of the reference window.

In the second contribution, as ship detection in SAR images are influenced mainly by the presence of outliers such as high-target-density situations, busy shipping lines, crowded harbors, lands and oil spills, conventional CFAR detectors suffer P_D degradation and/or P_{FA} increase. We proposed a new robust and fast detector named MAD-CFAR for ship detection in SAR images embedded in heterogeneous log-normal clutter. As it is well known, the SDM is a spread of data measure which can be very affected by strong and/or weak outliers and non-Gaussianity of the background clutter. To alleviate this problem, we recoursed to the absolute deviation around the median, commonly known as the MAD) measure which happens to be more resilient to outliers in multiple target situations. Simulations results showed that compared to the performances of recent CFAR detectors on both simulated and real SAR images, the MAD-CFAR detector exhibits a good false alarm regulation and a high detection in a heterogeneous log-normal background.

In the third contribution, we deal with the problem inherent to lower and upper censoring of unwanted pixels from a rank ordered SRW in SAR images. Assuming complex scenes of log-normal sea clutter with no a *priori* knowledge about any kinds of outliers such as interfering ship targets, harbor areas and oil spills; we proposed and analyzed the automatic bilateral censoring and detection performances of the AML-CFAR detector. Considering an SRW with no guard region, the CFCR and CFAR are guaranteed by use of linear biparametric adaptive thresholds. In doing this, we introduced a logarithmic amplifier and determined the transformed Gaussian distribution parameters through their respective AMLEs. That is, assuming a homogeneous middle half ranked sub-SRW, we first computed the lower and upper censoring thresholds through the closed form solutions of the AML estimates of the unknown log-mean and log-standard deviation parameters. Then, upon censoring of both ends, we used the remaining set to estimate the unknown distribution parameters through the same expressions of the AML estimates. Extensive simulations on both simulated SAR and real SAR images showed that the AML-CFAR detector performs better than its competing state-of-the-art detectors.

7.2 Perspectives and Future Work

The elaboration of this work has allowed us to discover many virtues of the detectors based on the techniques of automatic unilateral and bilateral excisions. The axes to be considered as perspectives for future work can be summarized as follows

- For the first contribution that we have considered, namely the QM-CFAR detector, we may address the problem of automatic target detection in a Weibull clutter and multiple target situations with the assumption of no prior knowledge of the number of interfering targets.

- As for the second contribution that we have considered, namely the MAD-CFAR detector, we plan to investigate its performance on other LS distributions, and may also use the associated statistics as a censoring stage with other estimation methods.

- As CFAR detection in heterogeneous high-resolution sea clutter is still an open problem, another ultimate opening for future works would be to investigate the performance of the AML estimators with other censoring approaches, capable of enhancing the overall performances of the AML-CFAR detector while performing a fair regulation of the P_{FA}. Further assessment of the effectiveness of the AML-CFAR detector may also be carried out for other radar target detection applications, such as MIMO (Multiple Input Multiple Output) radars.

- Finally, we will go one-step further and investigate a deep neural network for the joint classification and characterization of ships from SAR images as it shows promising results.

Bibliography

[1] Angélique Melet, Pietro Teatini, Goneri Le Cozannet, Cédric Jamet, Alessandra Conversi, J. Benveniste, and Rafael Almar. Earth observations for monitoring marine coastal hazards and their drivers. *Surveys in Geophysics*, 41, 11 2020.

[2] Canada Center for Remote Sensing. Fundamentals of remote sensing, 2015. February 01, 2023.

[3] Gerardo Di Martino, Antonio Iodice, et al. *Maritime Surveillance with Synthetic Aperture Radar*. Radar, Sonar and Navigation. Institution of Engineering and Technology, 2020.

[4] Qiang Zhao, Le Yu, Zhenrong Du, Dailiang Peng, Pengyu Hao, Yongguang Zhang, and Peng Gong. An overview of the applications of earth observation satellite data: Impacts and future trends. *Remote Sensing*, 14(8), 2022.

[5] David J Crisp. The state-of-the-art in ship detection in synthetic aperture radar imagery. Technical report, Defence Science and Technology Organisation Salisbury Australia, 05 2004.

[6] Donato Amitrano, Gerardo Di Martino, Raffaella Guida, Pasquale Iervolino, Antonio Iodice, Maria Nicolina Papa, Daniele Riccio, and Giuseppe Ruello. Earth environmental monitoring using multi-temporal synthetic aperture radar: A critical review of selected applications. *Remote Sensing*, 13(4), 2021.

[7] Sharma Kumar Sharma, B. Saravana Kumar, Nilesh M. Desai, and V.R. Gujraty. Sar for disaster management. *IEEE Aerospace and Electronic Systems Magazine*, 23(6):4–9, 2008.

[8] Ding Tao. Maritime target detection in non-homogeneous sea clutter environments based on single-and multi-polarization synthetic aperture radar data. 2015.

[9] George Melillos, Kyriacos Themistocleous, George Papadavid, Athos Agapiou, Demetris Kouhartsiouk, Maria Prodromou, Silas Michaelides, and Diofantos Hadjimitsis. Using field spectroscopy combined with synthetic aperture radar (sar) technique for detecting

underground structures for defense and security applications in cyprus. page 1018206, 05 2017.

[10] Ian G Cumming and Frank H Wong. Digital processing of synthetic aperture radar data. *Artech house*, 1(3):108–110, 2005.

[11] Mehdi Amoon, Ahmad Bozorgi, and Gholam-ali Rezai-rad. New method for ship detection in synthetic aperture radar imagery based on the human visual attention system. *Journal of Applied Remote Sensing*, 7(1):071599–071599, 2013.

[12] Ryan A. English, Steve J. Rawlinson, and Nicholas M. Sandirasegaram. ATR workbench for automating image analysis. In Edmund G. Zelnio and Frederick D. Garber, editors, *Algorithms for Synthetic Aperture Radar Imagery X*, volume 5095, pages 349 – 357. International Society for Optics and Photonics, SPIE, 2003.

[13] Xiaolong Wang and Cuixia Chen. A fast line-scanning-based detection algorithm for real-time sar ship detection. *Signal, Image and Video Processing*, 9:1975–1982, 2015.

[14] Ming Liu, Shichao Chen, Fugang Lu, Mengdao Xing, and Jingbiao Wei. Realizing target detection in sar images based on multiscale superpixel fusion. *Sensors*, 21(5), 2021.

[15] Khalid El-Darymli, Peter McGuire, Desmond Power, and C. Moloney. Target detection in synthetic aperture radar imagery: A state-of-the-art survey. *Journal of Applied Remote Sensing*, 7:071598–071598, 01 2013.

[16] Courtney Hilliard. Selection of a clutter rejection algorithm for real-time target detection from an airborne platform. *Proceedings of SPIE - The International Society for Optical Engineering*, 4048, 07 2000.

[17] Asha Shakin Banu, P. Vasuki, and S. Md Mansoor Roomi. Target detection in sar images using bayesian saliency and morphological attribute profiles. *Computer Communications*, 160:738–748, 2020.

[18] Cai Fu-qing, Song Jie, Liu Heng-yan, and Xiong Wei. Sar image target-detection method based on two-stage cfar detector with g0 distribution. *The Journal of Engineering*, 2019(19):6206–6209, 2019.

[19] Yi Cui, Jian Yang, Yoshio Yamaguchi, Gulab Singh, Sang-Eun Park, and Hirokazu Kobayashi. On semiparametric clutter estimation for ship detection in synthetic aperture

radar images. *IEEE Transactions on Geoscience and Remote Sensing*, 51(5):3170–3180, 2013.

[20] John E. McGowan, Steven C. Gustafson, Julie Ann Jackson, and Andrew J. Terzuoli Jr. The effect of synthetic aperture radar image resolution on target discrimination. In Edmund G. Zelnio and Frederick D. Garber, editors, *Algorithms for Synthetic Aperture Radar Imagery XVII*, volume 7699, page 76990X. International Society for Optics and Photonics, SPIE, 2010.

[21] Hicham Madjidi, Toufik Laroussi, and Faical Farah. On maximum likelihood quantile matching cfar detection in weibull clutter and multiple rayleigh target situations: A comparison. *Arabian Journal for Science and Engineering*, 12 2022.

[22] Hicham Madjidi, Toufik Laroussi, and Faical Farah. A robust and fast cfar ship detector based on median absolute deviation thresholding for sar imagery in heterogeneous log-normal sea clutter. *Signal, Image and Video Processing*, pages 1–7, 02 2023.

[23] Hicham Madjidi and Toufik Laroussi. Approximate mle based automatic bilateral censoring cfar ship detection for complex scenes of log-normal sea clutter in sar imagery. *Digital Signal Processing*, 136:103972, 2023.

[24] Hicham Madjidi, Toufik Laroussi, and Faiçal Farah. A cfar detection algorithm for weibull and lognormal clutter mixture in sar images. In *2022 19th International Multi-Conference on Systems, Signals and Devices (SSD)*, pages 286–291, 2022.

[25] Hicham Madjidi, Toufik Laroussi, and Faiçal Farah. Cfar ship detection in sar images based on the generalized rayleigh mixture models. In *the 2022 International Conference of advanced Technology in Electronic and Electrical Engineering (ICATEEE)*, pages 286–291, 2022.

[26] Toufik Laroussi. *détection adaptative CFAR de cibles chi-square corrélées a plusieurs degrés de liberté en présence d'un fouillis Rayleigh corrélé*. PhD thesis, Université Frères Mentouri Constantine 1, 2005.

[27] J.F. Dallernan, J. Lichtenegger, H. Laur, and Ph. Rebillard. Principes d'imagerie radar. Technical report, Série du Centre de Télédétection FAO, No. 46 Rome, 1991.

[28] Khalid El-Darymli. *Holism for target recognition in synthetic aperture radar imagery*. PhD thesis, Memorial University of Newfoundland, 2015.

[29] Masinde Muliro University of Science and Technology. Introduction to radar systems, 2012. February 01, 2023.

[30] Alicja Ossowska. *Highly Resolved Synthetic Aperture Radar with Beam Steering.* PhD thesis, 01 2015.

[31] Abigael Taylor. *Traitements SAR multivoies pour la détection de cibles mobiles.* PhD thesis, 12 2016.

[32] Africa Flores, K. Herndon, Rajesh Thapa, and Emil Cherrington. *The SAR Handbook: Comprehensive Methodologies for Forest Monitoring and Biomass Estimation.* 04 2019.

[33] Julien Delprato. *Analyse de la stabilité d'impulsion à impulsion des amplificateurs de puissance HEMT GaN pour applications radar en bande S.* Theses, Université de Limoges, September 2016.

[34] Ayoub Karine. *Traitement et classification parcimonieuse des images radar pour l'aide à la reconnaissance de cibles.* PhD thesis, 12 2018.

[35] Charles Elachi and Jakob J Van Zyl. *Introduction to the physics and techniques of remote sensing.* John Wiley & Sons, 2021.

[36] Alberto Moreira, Pau Prats-Iraola, Marwan Younis, Gerhard Krieger, I. Hajnsek, and Konstantinos Papathanassiou. A tutorial on synthetic aperture radar. *IEEE Geoscience and Remote Sensing Magazine (GRSM)*, 1:6–43, 03 2013.

[37] Virginie Amberg. *Analyse de scènes péri-urbaines à partir d'images radar haute résolution. Application à l'extraction semi-automatique du réseau routier.* PhD thesis, 01 2005.

[38] Pasquale Iervolino and Raffaella Guida. A novel ship detector based on the generalized-likelihood ratio test for sar imagery. *IEEE Journal of Selected Topics in Applied Earth Observations and Remote Sensing*, 10(8):3616–3630, 2017.

[39] Elena Martellato, Alice Maria Piccirillo, Giampaolo Ferraioli, Alessandra Rotundi, Vincenzo Della Corte, Pasquale Palumbo, Emanuele Alcaras, Luca Appolloni, Giuseppe Aulicino, Ivano Bertini, Vincenzo Capozzi, Elena Catucci, Zelia Dionnet, Pasquale Di Palma, Flavio Esposito, Emanuele Ferrentino, Anna Innac, Laura Inno, Silvia Pennino, Simona Saviano, Giuseppina Tirimberio, Stefania Campopiano, Elena Chianese,

Pier Paolo Franzese, Giannetta Fusco, Salvatore Gaglione, Agostino Iadicicco, Ferdinando Nunziata, Claudio Parente, Vincenzo Piscopo, Angelo Riccio, Giovanni Fulvio Russo, and Enrico Zambianchi. A new orbiting deployable system for small satellite observations for ecology and earth observation. *Remote Sensing*, 14(9), 2022.

[40] Ali El Zaart. *Statistical inference and distribution selection for SAR image analysis : a mixture-based approach*. PhD thesis, 2001.

[41] Odysseas Pappas, Alin Achim, and David Bull. Superpixel-level cfar detectors for ship detection in sar imagery. *IEEE Geoscience and Remote Sensing Letters*, 15(9):1397–1401, 2018.

[42] Yi Cui, Jian Yang, and Yoshio Yamaguchi. Cfar ship detection in sar images based on lognormal mixture models. In *2011 3rd International Asia-Pacific Conference on Synthetic Aperture Radar (APSAR)*, pages 1–3, 2011.

[43] HM Finn. Adaptive detection mode with threshold control as a function of spatially sampled clutter-level estimates. *Rca Rev.*, 29:414–465, 1968.

[44] G.V. Trunk. Range resolution of targets using automatic detectors. *IEEE Transactions on Aerospace and Electronic Systems*, AES-14(5):750–755, 1978.

[45] V Gregers Hansen. Constant false alarm rate processing in search radars. In *IEE Conf. Publ. no. 105," Radar-Present and Future"*, pages 325–332, 1973.

[46] Hermann Rohling. Radar cfar thresholding in clutter and multiple target situations. *IEEE Transactions on Aerospace and Electronic Systems*, AES-19(4):608–621, 1983.

[47] Ding Tao, Stian Normann Anfinsen, and Camilla Brekke. Robust cfar detector based on truncated statistics in multiple-target situations. *IEEE Transactions on Geoscience and Remote Sensing*, 54(1):117–134, 2016.

[48] Saeed Erfanian and Vahid Tabataba Vakili. Introducing excision switching-cfar in k distributed sea clutter. *Signal Processing*, 89(6):1023–1031, 2009.

[49] M. Walessa and M. Datcu. Model-based despeckling and information extraction from sar images. *IEEE Transactions on Geoscience and Remote Sensing*, 38(5):2258–2269, 2000.

[50] R. Touzi, A. Lopes, and P. Bousquet. A statistical and geometrical edge detector for sar images. *IEEE Transactions on Geoscience and Remote Sensing*, 26(6):764–773, 1988.

[51] T. Macri-Pellizzeri, C.J. Oliver, and Pierfrancesco Lombardo. Segmentation-based joint classification of sar and optical images. *Radar, Sonar and Navigation, IEE Proceedings* -, 149:281 – 296, 01 2003.

[52] C. Tison, J.-M. Nicolas, F. Tupin, and H. Maitre. A new statistical model for markovian classification of urban areas in high-resolution sar images. *IEEE Transactions on Geoscience and Remote Sensing*, 42(10):2046–2057, 2004.

[53] A. Farrouki and Mourad Barkat. Automatic censoring cfar detector based on ordered data variability for nonhomogeneous environments. *Radar, Sonar and Navigation, IEE Proceedings* -, 152:43 – 51, 03 2005.

[54] Gui Gao. A parzen-window-kernel-based cfar algorithm for ship detection in sar images. *IEEE Geoscience and Remote Sensing Letters*, 8(3):557–561, 2010.

[55] L. Bruzzone, M. Marconcini, U. Wegmuller, and A. Wiesmann. An advanced system for the automatic classification of multitemporal sar images. *IEEE Transactions on Geoscience and Remote Sensing*, 42(6):1321–1334, 2004.

[56] P. Mantero, G. Moser, and S.B. Serpico. Partially supervised classification of remote sensing images using svm-based probability density estimation. In *IEEE Workshop on Advances in Techniques for Analysis of Remotely Sensed Data, 2003*, pages 327–336, 2003.

[57] Xiaobo Deng, Chao Gao, and Jian Yang. Sea clutter amplitude statistics analysis by goodness-of-fit test. *Procedia Engineering*, 29:791–796, 12 2012.

[58] Mourad Barkat. *Signal Detection and Estimation.* Radar Library. Artech House, Norwood, MA, 2 edition, August 2005.

[59] J. Marcum. A statistical theory of target detection by pulsed radar. *IRE Transactions on Information Theory*, 6(2):59–267, 1960.

[60] P. Swerling. Probability of detection for fluctuating targets. *IRE Transactions on Information Theory*, 6(2):269–308, 1960.

[61] Camilla Brekke and Stian Normann Anfinsen. Ship detection in ice-infested waters based on dual-polarization sar imagery. *IEEE Geoscience and Remote Sensing Letters*, 8(3):391–395, 2011.

[62] Nizar Bouhlel and Stéphane Méric. Maximum-likelihood parameter estimation of the product model for multilook polarimetric sar data. *IEEE Transactions on Geoscience and Remote Sensing*, 57(3):1596–1611, 2019.

[63] Gary Minkler and Jing Minkler. Cfar: the principles of automatic radar detection in clutter. *NASA STI/Recon Technical Report A*, 90:23371, 1990.

[64] M.I. Skolnik. *Introduction to Radar Systems*. Electrical engineering series. McGraw-Hill, 3. edition, 2001.

[65] G.B. Goldstein. False-alarm regulation in log-normal and weibull clutter. *Aerospace and Electronic Systems, IEEE Transactions on*, AES-9:84 – 92, 02 1973.

[66] Peter Weber and Simon Haykin. Ordered statistic cfar processing for two-parameter distributions with variable skewness. *IEEE Transactions on Aerospace and Electronic Systems*, AES-21(6):819–821, 1985.

[67] Rafi Ravid and Nadav Levanon. Maximum-likelihood cfar for weibull background. *Radar and Signal Processing, IEE Proceedings F*, 139:256 – 264, 07 1992.

[68] Fernando Darío Almeida García, Henry Ramiro Carvajal Mora, Gustavo Fraidenraich, and José Cândido Silveira Santos Filho. Square-law detection of exponential targets in weibull-distributed ground clutter. *IEEE Geoscience and Remote Sensing Letters*, 18(11):1956–1960, 2021.

[69] Amel Gouri, Amar Mezache, and Houcine Oudira. Radar cfar detection in weibull clutter based on zlog(z) estimator. *Remote Sensing Letters*, 11:581–589, 06 2020.

[70] Graham Weinberg, Lachlan Bateman, and Peta Hayden. Development of non-coherent cfar detection processes in weibull background. *Digital Signal Processing*, 75, 01 2018.

[71] Baiqiang Zhang, Jie Zhou, Junhao Xie, and Wei Zhou. Weighted likelihood cfar detection for weibull background. *Digital Signal Processing*, 115:103079, 05 2021.

[72] Matsuo Sekine and Yuhai Mao. *Weibull radar clutter*. Number 3. Institution of Engineering and Technology, 1990.

[73] Rajbir-Singh Nirwan and Nils Bertschinger. Bayesian quantile matching estimation. *arXiv preprint arXiv:2008.06423*, 2020.

[74] Yunhan Dong. Distribution of x-band high resolution and high grazing angle sea clutter. Technical report, Defence Science and Technology Organisation Edinburgh (Australia) Electronic, 2006.

[75] Reza Ghaderi Zefreh, Mohammad Reza Taban, Mohammad Mahdi Naghsh, and Saeed Gazor. Robust cfar detector based on censored harmonic averaging in heterogeneous clutter. *IEEE Transactions on Aerospace and Electronic Systems*, 57(3):1956–1963, 2021.

[76] Lei Zuo, Ming Li, Xiaowei Zhang, Peng Zhang, and Yan Wu. Cfar detection of range-spread targets based on the time-frequency decomposition feature of two adjacent returned signals. *IEEE Transactions on Signal Processing*, 61(24):6307–6319, 2013.

[77] Yongchan Gao, Hongbing Ji, and Weijian Liu. Persymmetric adaptive subspace detectors for range-spread targets. *Digital Signal Processing*, 89:116–123, 2019.

[78] Dong-Xiao Yue, Feng Xu, Alejandro C. Frery, and Ya-Qiu Jin. Synthetic aperture radar image statistical modeling: Part one-single-pixel statistical models. *IEEE Geoscience and Remote Sensing Magazine*, 9(1):82–114, 2021.

[79] Jun Liu, Davide Massaro, Danilo Orlando, and Alfonso Farina. Radar adaptive detection architectures for heterogeneous environments. *IEEE Transactions on Signal Processing*, 68:4307–4319, 2020.

[80] K.D. Ward, Chris Baker, and S. Watts. Maritime surveillance radar. i. radar scattering from the ocean surface. *IEE Proceedings F (Radar and Signal Processing)*, 137:51 – 62, 05 1990.

[81] S. Kuttikkad and R. Chellappa. Non-gaussian cfar techniques for target detection in high resolution sar images. In *Proceedings of 1st International Conference on Image Processing*, volume 1, pages 910–914 vol.1, 1994.

[82] Yongchan Gao, Guisheng Liao, and Weijian Liu. High-resolution radar detection in interference and nonhomogeneous noise. *IEEE Signal Processing Letters*, 23(10):1359–1363, 2016.

[83] Jiaqiu Ai, Xuezhi Yang, Jitao Song, Zhangyu Dong, Lu Jia, and Fang Zhou. An adaptively truncated clutter-statistics-based two-parameter cfar detector in sar imagery. *IEEE Journal of Oceanic Engineering*, 43(1):267–279, 2018.

[84] Jiaqiu Ai, Yuxiang Mao, Qiwu Luo, Mengdao Xing, Kai Jiang, Lu Jia, and Xingming Yang. Robust cfar ship detector based on bilateral-trimmed-statistics of complex ocean scenes in sar imagery: A closed-form solution. *IEEE Transactions on Aerospace and Electronic Systems*, 57(3):1872–1890, 2021.

[85] Christophe Leys, Christophe Ley, Olivier Klein, Philippe Bernard, and Laurent Licata. Detecting outliers: Do not use standard deviation around the mean, use absolute deviation around the median. *Journal of Experimental Social Psychology*, 49:764–766, 07 2013.

[86] European Space Agency. https://tpm-ds.eo.esa.int/oads/access/collection/TerraSAR-X, 2022.

[87] Copernicus open access hub. https://scihub.copernicus.eu/. [Accessed 27 November 2022].

[88] Souad Chabbi. *Détection CFAR en Milieux Non-Gaussiens Corrélés*. PhD thesis, Université Frères Mentouri Constantine 1, 2015.

[89] A. Pourmottaghi, M. R. Taban, and S. Gazor. A cfar detector in a nonhomogenous weibull clutter. *IEEE Transactions on Aerospace and Electronic Systems*, 48(2):1747–1758, 2012.

[90] Souad Chabbi, Toufik Laroussi, and Mourad Barkat. Performance analysis of dual automatic censoring and detection in heterogeneous weibull clutter: A comparison through extensive simulations. *Signal Processing*, 93:2879–2893, 11 2013.

[91] N. Balakrishnan. Approximate mle of the scale parameter of the rayleigh distribution with censoring. *IEEE Transactions on Reliability*, 38(3):355–357, 1989.

[92] N. Balakrishnan. Approximate maximum likelihood estimation of the mean and standard deviation of the normal distribution based on type ii censored samples. *Journal of Statistical Computation and Simulation*, 32(3):137–148, 1989.

[93] Narayanaswamy Balakrishnan, N Balakrishnan, and Rita Aggarwala. *Progressive censoring: theory, methods, and applications*. Springer Science & Business Media, 2000.

[94] Robert Kissell and Jim Poserina. Chapter 4 - advanced math and statistics. In Robert Kissell and Jim Poserina, editors, *Optimal Sports Math, Statistics, and Fantasy*, pages 103–135. Academic Press, 2017.

[95] Cai Fu-qing, Song Jie, Liu Heng-yan, and Xiong Wei. Sar image target-detection method based on two-stage cfar detector with g0 distribution. *The Journal of Engineering*, 2019(19):6206–6209, 2019.

[96] Alos-2 / palsar-2 sample product. https://www.eorc.jaxa.jp/ALOS-2/en/doc/sam_index.htm. [Accessed 8 January 2023].